THE UNIVERSITY OF ILLINOIS AT CHICAGO

Theoretical and Experimental Studies on the Foundations of Mesomechamics

Final Report

By

A. Chudnovsky and S. Wu
Fracture Research Laboratory
Department of Civil Engineering,Mechanics & Metallurgy
University of Illinois at Chicago, P.O. Box 4348
Chicago, IL 60680

Prepared for:

The Air Force Office of Scientific Research
Directorate of Aerospace Sciences
Bolling Air Force Base
Washington, D.C. 20332-6448

Contract No: 89-0105

REPORT DOCUMENTATION PAGE

Form Approved
OMB No. 0704-0188

1. AGENCY USE ONLY (Leave blank)	2. REPORT DATE	3. REPORT TYPE AND DATES COVERED
	June 28, 1992	Final 11/89 to 4/92

4. TITLE AND SUBTITLE

Theoretical and Experimental Studies on the Foundation of Mesomechanics

5. FUNDING NUMBERS

AFOSR-89-0105

6. AUTHOR(S)

A. Chudnovsky and S. Wu

7. PERFORMING ORGANIZATION NAME(S) AND ADDRESS(ES)

Dept. of Civil Engineering, Mechanics and Metallurgy
University of Illinois at Chicago
Box 4348
Chicago, IL 60680

8. PERFORMING ORGANIZATION REPORT NUMBER

9. SPONSORING/MONITORING AGENCY NAME(S) AND ADDRESS(ES)

Aerospace Science/AFOSR
Bolling, AFB
Washington, D.C. 20332

10. SPONSORING/MONITORING AGENCY REPORT NUMBER

11. SUPPLEMENTARY NOTES

12a. DISTRIBUTION/AVAILABILITY STATEMENT

Approved for public release,
distribution unlimited

12b. DISTRIBUTION CODE

13. ABSTRACT *(Maximum 200 words)*

SEE NEXT PAGE

14. SUBJECT TERMS

mesomechanics, crack layer, crack-microcrack interaction, process zone, damage, fracture toughness, thermodynamic model, kinetics

15. NUMBER OF PAGES

122

16. PRICE CODE

17. SECURITY CLASSIFICATION OF REPORT	18. SECURITY CLASSIFICATION OF THIS PAGE	19. SECURITY CLASSIFICATION OF ABSTRACT	20. LIMITATION OF ABSTRACT
Unclassified			

ABSTRACT

The report summaries a closely coupled experimental and theoretical investigations of various stages of Fracture Process: (1) accumulation of "damage" on submicroscopical and microscopical scales leading to crack initiation; (2) slow (subcritical) crack growth and an evolution of the damage zone; (3) transition to dynamic crack growth and the catastrophic failure.

The experimental part of the program is focused on the observation and quantitative characterization of damage preceding and accompanying crack initiation and growth. A special experimental setup for studying the fracture process under variable stress field is reported in Chapter 2. A leading role of crack-damage interaction in fracture process is well documented. A new formalism for solution of crack-microcrack array interaction problem and its successful implementation in the evaluation of crack layer driving forces is presented in Chapter 3.

A new model of the process zone, which generalizes the well-known Dagdale-Barenblatt model is presented in Chapter 4. A new measure for material toughness and the prediction of R-curve behavior illustrate the practical application of our model. Experimental examinations of our model under various test conditions are reported in Chapters 4, 5 and 6. The development of the constitutive equations for Crack Layer evolution and their experimental examinations under stress relaxation, fatigue and creep conditions are reported in Chapters 5 and 6.

An accelerated test procedure and the formulation of crack layer instability criteria as a substitution for the conventional fracture toughness parameters are also discussed in Chapter 6.

SIGNIFICANT ACCOMPLISHMENTS

1 A new test methodology was developed for studying the law of crack propagation.

2 A protocol for quantitative characterization of damage and its evolution was established.

3 A new formalism for the crack-damage interaction problem has been developed. It successfully implemented in evaluation of the crack layer driving forces.

4 A thermodynamic model of the process zone was proposed. It generalizes the well-known Dagdale-Barenblatt model. Our **new model describes** a wide range of **experimental data with no adjustable parameters.**

5 A constitutive equation of process zone growth under stress relaxation condition was derived and verified experimentally.

6 Kinetic equations of the crack and its surrounding damage zone growth were proposed. The equations adequately describe experimentally observed nonmonotonic crack layer propagation.

7 Crack Layer **instability criteria** were developed to **substitute** the conventional **fracture toughness parameters.** Well known R-curve behavior has been obtained from crack layer stability considerations.

8 An accelerated test to predict the time to failure under fatigue and creep conditions was proposed. A comparison with well characterized experimental data reported elsewhere illustrates the predictive power of the proposed methodology.

9 An inspection tool and an inspection manual aimed at prevention of polycarbonate canopy failure has been developed. This work has been funded by The Wright Laboratory, WPAFB, through AFOSR grant 890105. The detailed report of these studies is presented directly to, and will be published by The Wright Laboratory.

LIST OF PROFESSIONAL PERSONNEL AND PUBLICATIONS

Personnel:

- A. Chudnovsky, Professor
- S. Wu, Research Associate
- B. Kunin, Research Associate, Ph.D. Completed, Spring, 1992
- W.L. Huang, Research Assistant, Ph.D. Completed, Spring, 1992
- K. Kadota, Research Assistant, Ph.D. Completed, Summer 1992
- A. Kim, Research Assistant, Ph.D. Completed, Summer 1992

Publications:

1 Huang, W.-L., Kunin, B., and Chudnovsky, A.: Kinematics of damage zone accompanying curved crack. Proc. Symp. Mechanics of Plastics and Plastics Composites, Dec., 1989, also appeared in *International Journal of Fracture*, 50: 143-152, 1991.

2 Chudnovsky, A. and Wu, S. (1990) "Effect of crack-microcrack on release rates," *International Journal of Fracture*, 44, 43-56

3 Chudnovsky, A. and Wu, S.(1991) "Elastic interaction of a crack with random array of microcracks," *International Journal of Fracture*, 49, p123-140.

4 Chudnovsky, A., Huang, W.-L., and Kunin, B.: Effect of damage on fatigue crack propagation in polystyrene. *Polymer Engineering and Science*, 30(20): 1303-1308, 1990.

5 Wu, S. and Chudnovsky, A. (1990) "Effective elastic properties of a linear elastic solid with microcracks," *Engineering Fracture Mechanics*, 37(3), P653

6 A. Chudnovsky and S. Wu: "Evaluation of ERR in crack-microcracks interaction problem", *Inter. J. Solids and Structure*, Vol.29, 1699-1709 (1992)

7 A. Stojimirovic and A. Chudnovsky, "A New Thermodynamic Model for a Process Zone in Polymers", *Inter. J. Fracture*. in press

8 A. Kim, L. V. Garrett, C. P. Bosnyak and A. Chudnovsky,"Kinetics and chracterization of the process zone evolution", *J. Appl. Polym. Sci.*, in press.

9 A. Stojimirovic, K. Kadota, A. Chudnovsky, "An Equilibrium Process Zone in Polymeric Materials", *J. of Applied Polymer Sci.*, to appear.

10 A. Kim, C. P. Bosnyak, and A. Chudnovsky: "An energy analysis of crack initiation and arrest in epoxy", *International Journal of Fracture* in press.

11 A. Kim, L.V Garrett, C. P. Bosnyak, and A. Chudnovsky: "Modeling for kinetics of the process zone evolution in polycarbonate", *J. Appl. Polym. Sci.*, in press.

Presentations:

1 K. Kadota and A. Chudnovsky, "Analysis of the Fatigue Process Zone in Polyethylene", *Proceedings of the ASME Winter Annual Meeting*, MD-29, 101, Dec. 1-6, (1991), Atlanta, GA.

2 K. Kadota, A. Chudnovsky, J. Strebel and A. Moet, "Fractographic Analysis of Fatigue Fracture in Polyethylene", *Proceedings of ANTEC'91*, Montreal, Canada, 2180 (1991).

3 Wu, S. and A. Chudnovsky, "Effect of Microdefects on Fracture Toughness", *Proceedings of ANTEC'92*, Detroit, Michigan, pp. 1720-1723. (1992)

4 K. Kadota and A. Chudnovsky, "Constitutive equations of crack layer growth", AMD-Vol. 132/MD-Vol. 30, *Recent Advances in Damage Mechanics and Plasticity*, ASME 1992.

5 K. Kadota, A. Stojimirovic, and A. Chudnovsky, "Modeling of the process zone in ductile polymers", *Proceedings of ANTEC'92*, Detroit, Michigan, pp. 1219-1222.

TABLE OF CONTENTS

CHAPTER 1

INTRODUCTION

This report summarizes a three year research program on fundamental problems of fracture phenomena. The program has been planned as a closely coupled experimental and theoretical investigation of various stages of the fracture process: (1) accumulation of "damage" on submicroscopic and microscopic scales leading to crack initiation; (2) slow (subcritical) crack growth accompanied by an evolution of the damage zone surrounding the crack; (3) instability of slow crack growth leading to the catastrophic failure. Accordingly, the issues addressed in this report are:

I. Observation, quantitative characterization and modeling of the damage preceding crack initiation and growth.

II. Kinetic equations for a crack and its surrounding damage growth. The payoff is the creation of a rational basis for a predictive formalism for lifetime and reliability of structural components.

The above topics have been extensively studied under the name Fracture Mechanics and related areas of research during the last four decades. Two primary directions of fracture research have emerged during this time.

The first direction is related to materials science and examines the hierarchy of microdefects, their nucleation, inter- and intrascale interaction and coalescence. The scale hierarchy can be visualized by employing progressively finer scales of observation. Here the fundamental question is which elements of the hierarchy of defects are central to fracture phenomena, and thus should be properly parametrized and included in a quantitative model. This question cannot not be answered solely by materials science. The formalism of continuum mechanics, which is the other direction in fracture research, must also be used.

Recent achievements in observational techniques challenge adequacy of the continuum approach to modeling the observed details of fracture phenomena. Obviously the complexity of an interaction of defects on various scales is the main obstacle for modeling. Thus one may simplify the picture by examining a crack surrounded by damage under relatively low magnification (less than 100X). Studies which link the material microstructure observed at such magnification with macroscopic properties belong to Mesomechanics. This term has recently been introduced to denote observations and models which focus on intermediate scales [1].

Observations on mesoscales reveal the existence of numerous similar features of fracture propagation in various materials, despite many differences in molecular structure and morphology [2]. These observations constitute the basis of our search for the objective laws of the fracture process.

OUTLINE OF THE REPORT

The following *Chapter 2* is dedicated to an experimental examination of the existing models of slow (quasi-static) crack growth. A new experimental setup has been proposed and implemented to observe and characterize crack growth in the complex stress field. This setup resulted in establishing the limitations of existing models, as well as recognition of an important role played by the damage zone in determining the direction and rate of crack growth.

A system consisting of a crack and its surrounding damage is referred to as a Crack Layer (CL). A protocol for CL characterization has been developed and reported in a few international and national meetings, and has been published in four papers (Int. J. Fracture, 1991 [3,4], Int. J. Solids Struct. [5], and J. Polym. Eng. [6]).

Close observation of CL reveals a high density of damage (crazes, shear bands, microcracks, and so forth) formed as a response to stress concentration. This calls for crack-damage interaction analysis. There was no available formalism, which would allow one to perform the stress analysis of crack-microcrack (crazes, etc.) array interaction for high density of microcracks. Therefore, we have made a special effort to develop a new formalism for the stress and energy analysis of crack interaction with a high density microcrack array. These new theoretical developments closely linked to the observations have been reported in a few meetings and published in two papers (Int. J. Fracture [7] and Eng. Fract. Mech. [8]). These results constitute *Chapter 3*.

The mesomechanical considerations of chapters 2 and 3 provide detailed knowledge of crack-damage interaction, but assume extensive knowledge of damage distribution. The latter requires tedious damage characterization and analysis. An alternative thermodynamic approach operates with only a few average parameters, and thus is much more adequate for engineering applications. Having this in mind, we developed a thermodynamic model of crack-damage interaction concurrently with mesomechanical studies. The two approaches complement each other. The new thermodynamic model of the damage zone is presented in *Chapter 4*. Here we operate with the effective properties of media with damage, and introduce thermodynamic driving forces which are responsible for damage zone evolution. The model is an essential generalization of the well-known Dagdale-Barenblatt model. Experimental examination of our model demonstrates its predictive power. Moreover, our model is one of only a few known thermodynamic models which describe a wide range of experimental data with no adjustable parameters. A new measure for material toughness and the prediction of R-curve behavior illustrate the practical application of the model. The model has been reported at SPE annual meeting [9], ASME meeting [10], and is to appear in Int. J. Fracture [11] and J. of Appl. Polym. Eng. Sci. [12].

Previous analysis has led us to recognize the important role of the process zone evolution in fracture phenomena. In *Chapter 5* the experimental and theoretical studies of the process zone kinetic are presented. The kinetic equation of process zone growth is derived by using the ideas of the thermodynamics of irreversible processes. The proposed equation results in a master curve for the process zone evolution for various initial conditions, and serves as the basis for mathematical modeling of CL evolution. The material in this chapter has been presented at SPE annual meeting [9] and Fracture Colloquium at Wright-Patterson Air Force Base, November 1991; two papers have been accepted for publication in Appl. Polym. Eng. Sci. [13,14].

The relationships between the rates of CL growth and the corresponding driving forces i.e., CL kinetic equations are addressed in *Chapter 6*. Following the general framework of irreversible thermodynamics, we formulate the kinetic equations by expressing the CL growth *rates* as a linear combination of CL *driving forces*. The proposed CL kinetic equations model well experimentally observed nonmonotonic CL growth, and provide the basis for fatigue and creep lifetime estimation. Such predictions have been examined by comparison with the large data base of fatigue and creep experiments reported in [15]. Prediction of lifetimes by the model is in an excellent agreement with an empirical formula, which summarizes a large pool of experimental data. The developments of this chapter have been reported at ASME meeting [16], SPE annual meeting [17], and is accepted for the Third PanAmerican Congress of Applied Mechanics [18]. The first paper on this subject has been accepted for publication in J. Appl. Polym. Eng. Sci. [14].

CHAPTER 2

EXAMINATION OF FATIGUE CRACK PROPAGATION LAW

2.1 Introduction

Fatigue crack growth has been studied for more than 30 years out of about 150 years of fatigue research. The first rational formulation, which summarized numerous experimental data, was due to Paris and Erdogan [19]. Since then, various models have been proposed offering equations of fatigue crack growth. All the models assume a functional relationship between the crack speed and the stress intensity factor increment $\Delta K_I = K_I|_{\sigma_{max}} - K_I|_{\sigma_{min}}$, mean value of K_I, or the energy release rate, G_1. For example, a comparative analysis of a number of models for fatigue crack growth in polymer can be found in [29]. The assumption of a functional relationship between the crack speed and ΔK_I or G_1 implies that the influence of the crack growth history prior to a given moment can be neglected. However, there are experimental evidences to the contrary [21]. Thus, it appears that the crack growth rate in general cannot be expressed as a function of ΔK_I or G_1 only.

In this chapter, we report the results of a specially designed experimental program of examining the relationship between the fatigue crack propagation rate and ΔK_I (or G_1). Fatigue crack growth in a vicinity of a hole in a single edge notched (SEN) specimen has been observed through travelling optical microscope and record on a video system. Commercial polystyrene (an amorphous transparent polymer) has been chosen as a model material. The experimental setup and parametric studies are described in details in Appendix A (section A.2.2.1).

One can observe a layer of damage (crazing in our case) surrounding and preceding the fatigue crack (see Fig. 2.1). The dark zone in Fig. 2.1 reflects the layer of intense crazing. A system of the crack and its surrounding damage zone is referred to as Crack Layer (CL) [2]. An Active and Inert Zones are distinguished within CL. The Active Zone (AZ) is the part of CL adjacent to the crack tip, where the damage growth is taking place. Figure 2.2 illustrates an AZ morphology in this experiment. The inert zone of CL appears as a trace of the AZ. It is illustrated in Fig. 2.3 by the consecutive configurations of the AZ at 790, 800, 810, etc. cycles and the corresponding envelope of the CL. Notice that the AZ positions are almost equally spaced whereas the time intervals (in number of cycles) are significantly different. In particular, the crack significantly slows down between C and D positions (see Fig 2.3). This coincides with dramatic changes in AZ size and orientation.

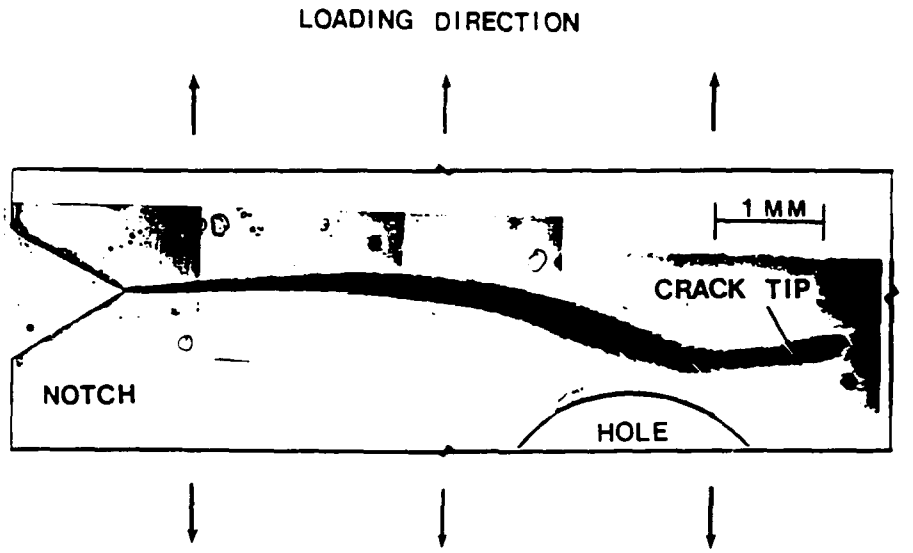

Figure 2.1 The fatigue-grown layer of intense crazing around a crack in a vicinity of a hole in a single edge notched specimen. Material: commercial polystyrene.

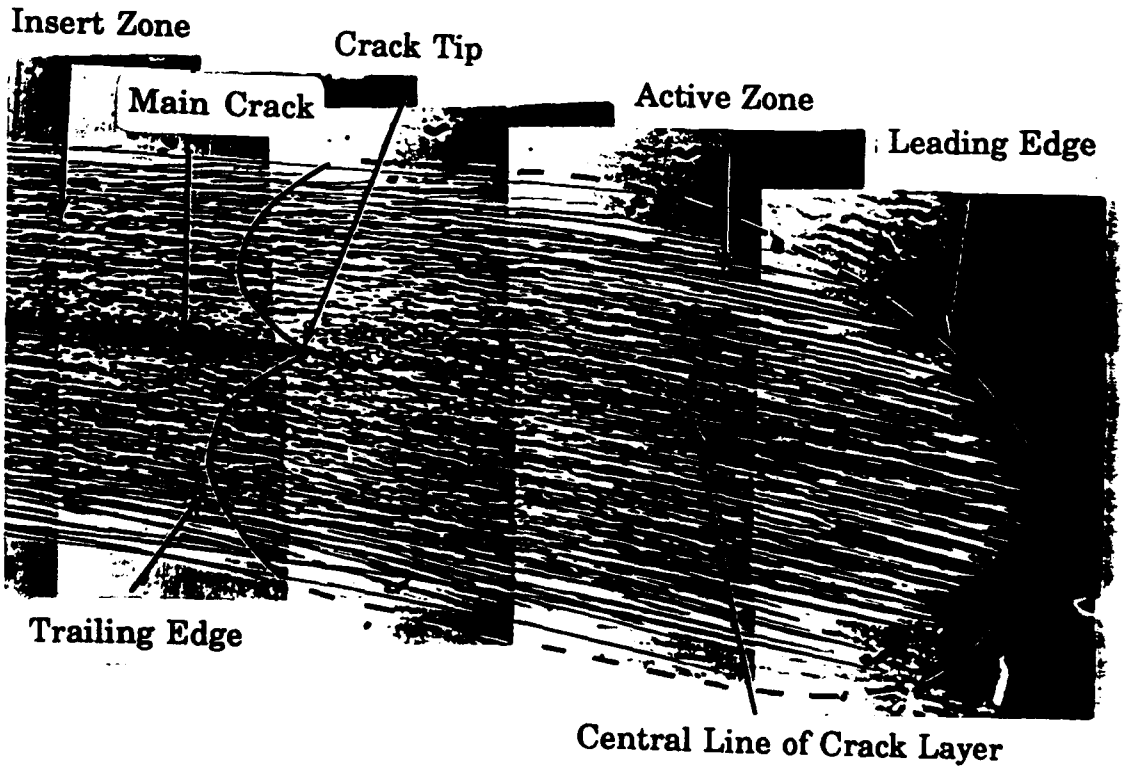

Figure 2.2 Crack Layer Notations.

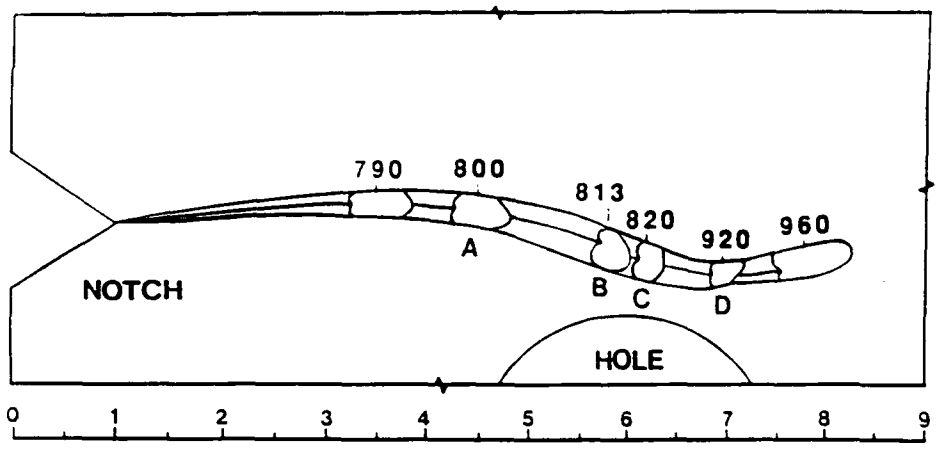

Figure 2.3 Crack Layer evolution in a vicinity of a hole. For each AZ position, the number of cycles counted from the beginning of the test is indicated. The middle line represents the main crack trajectory.

The analysis below demonstrates that there is no unique relationship between the crack propagation rate and conventional fracture mechanics parameters such as ΔK_I or G_1. Moreover, it results from our studies that the changes in the craze distribution and orientation within the AZ are primarily responsible for the effect.

Crack Layer Kinematics

In the absence of the hole, a fatigue crack in SEN specimen under simple tension propagates along the axis of symmetry. In our experiments, we position a hole at three different distances from the axis of symmetry (which we refer to as "reference line"). In all three cases, the crack propagates in a rectilinear fashion until it enters the domain where the elastic fields are perturbed by the presence of the hole. At this stage the crack begins to curve, as illustrated in Fig. 2.4 where crack trajectories traced from different specimens are superposed. The trajectories begin at differently positioned notches (reference lines at the distances 5r/3, 7r/3 and 9r/3 from the hole center, respectively; the hole radius r = 1.5 mm). The trajectories are well reproducible.

Figure 2.5 shows the speed of the crack along each of the trajectories shown in Fig. 2.4 (three separate tests). The position-vs.-cycle data are obtained from playback of the video recording of the crack growth process.

In Case 3 (crack trajectories farthest from the hole), the crack accelerates monotonically throughout its propagation. In Case 1 (crack trajectory closed to

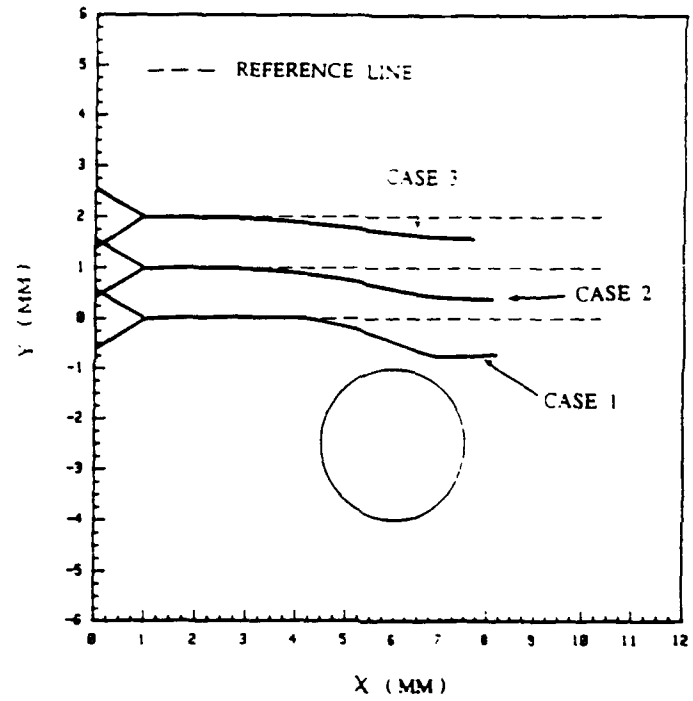

Figure 2.4 Trajectories of the main crack fatigue grown in specimens with different notch position relative to the hole.

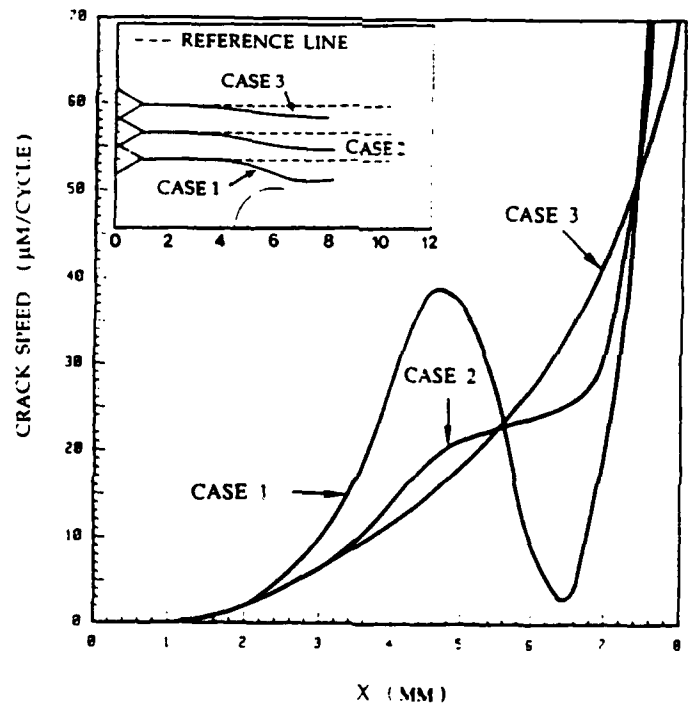

Figure 2.5 Crack speed $d\ell/dN$ (N number of cycles) as a function of the crack tip position along the trajectories shown in Fig. 2.4.

the hole), the crack speed is initially higher than in Case 3, then, as it enters the "shadow" above the hole (reduced stress), it decelerates to point of being almost arrested and, finally, it accelerates again. The crack behavior in Case 2 (intermediate position) falls in between those above.

In what follows, we will discuss mainly the most revealing Case 1.

Stress Intensity Factor and Energy Release Rate Estimation

Traditionally, the kinematics of fatigue crack growth is correlated with fracture parameters such as the stress intensity factor increment or the energy release rate (ERR). To do so, in our case, an elastic solution for infinite media, has been worked out by Rubinstein [22]. An adaptation of the Rubinstein's solution, which makes use of mode I and mode II correction factors for load-specimen configurations under consideration is presented in Figs. 2.6-2.7. Non-zero mode II stress intensity factor (Fig. 2.7) results from both the curvature of the crack and its interaction with the hole. WE also utilize ERR $G_1 = (K_I^2+K_{II}^2)/E$ to correlate with fatigue crack growth rate, since the mixed mode crack tip field is present. The ERR as a function of the crack tip position is shown in Fig. 2.8 for all three test configurations.

It should be noted that the mode I dominates: the ratio $K_I/K_{II} = \Delta K_I/\Delta K_{II} <$ 8%, hence the mode II contribution to the ERR is less than 1% $[K_{II}^2/(K_I^2 + K_{II}^2) < 1\%]$.

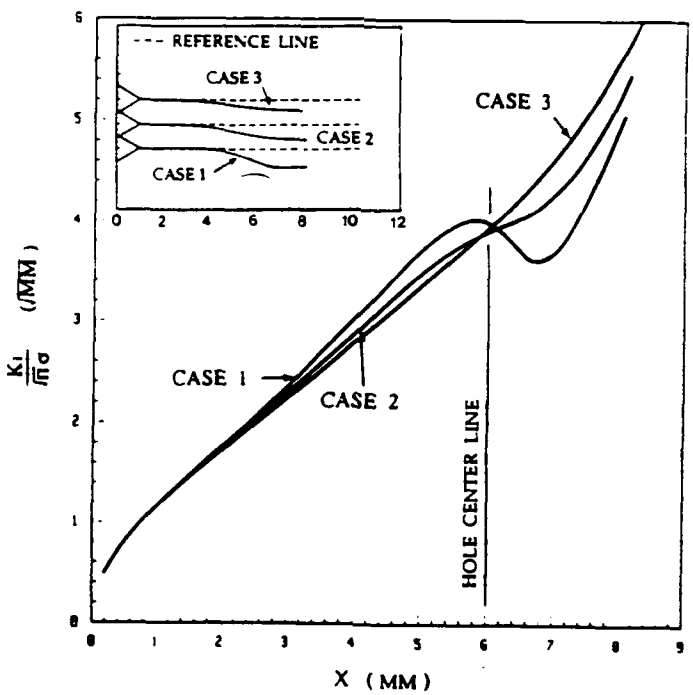

Figure 2.6 Normalized stress intensity factor K_I as a function of the crack tip position. The computations were performed for the crack configurations observed in the tests (Fig. 2.4).

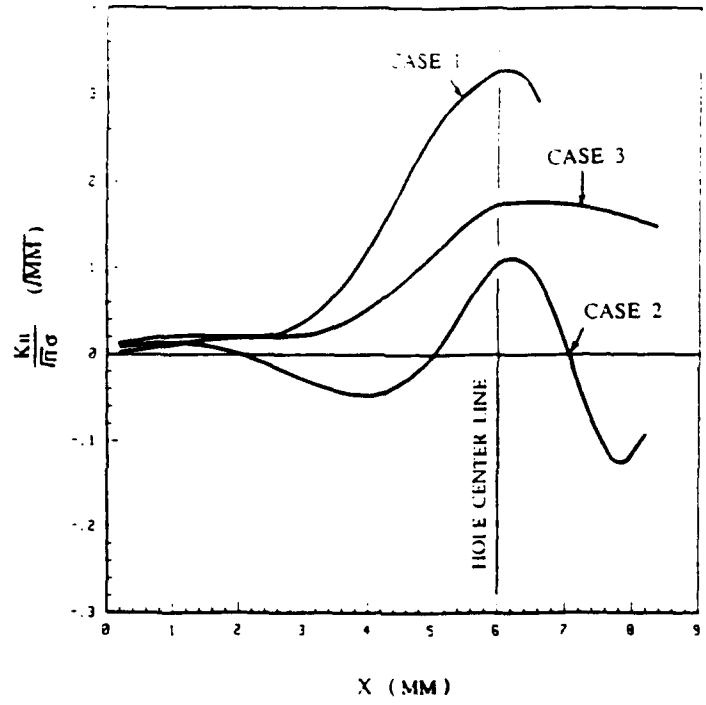

Figure 2.7 Normalized stress intensity factor K_{II} as a function of the crack tip position. The computations were performed for the crack configurations observed in the tests (Fig. 2.4).

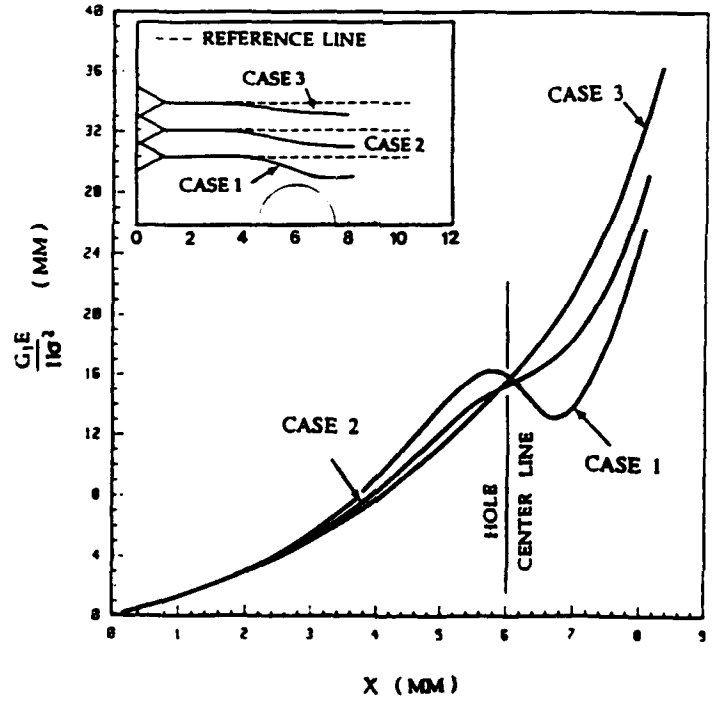

Figure 2.8 Normalized energy release rate as a function of the crack tip position. The computations were performed for the crack configurations observed in the tests (Fig. 2.4).

Crack Speed Versus ΔK_I , G_1

We start the discussion with Case 3 (see Fig. 2.4) which closely resembles the conventional test condition, i.e., a rectilinear crack in an SEN specimen. In this case, the log ($d\ell/dN$)-vs.-log (ΔK_I) plot indeed has a common shape (see Fig. 2.9): a significant portion of the curve (region II) is fairly linear, thus the power law approximation $d\ell/dN = A(\Delta K_I)^n$, $A=2.4\times10^{-6}$, n=2.2 (SI units) is justified.

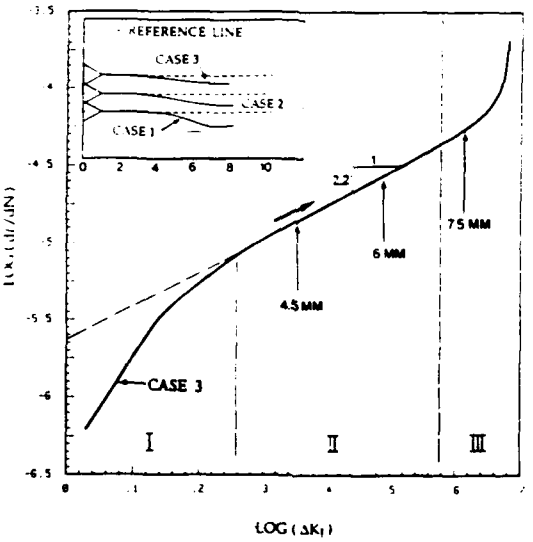

Figure 2.9 Crack speed $d\ell/dN$ for the crack trajectory farthest from the hole (Case 3 in Fig. 2.4) in relation to the corresponding stress intensity factor increment ΔK_I in a log-log plot. The relation is obtained from Figs. 2.5 and 2.6. The thick arrow above the curve shows the direction of crack growth (i.e. the increment of "X" in Figs. 2.5 and 2.6).

For the crack having the intermediate position relative to the hole (Case 2 in Fig. 2.4), there are two ranges over which the log ($d\ell/dN$)-vs.-log (ΔK_I) relation is approximately linear (see Fig. 2.10), though both line is not a good approximation for the curve any more. However, one still finds one-to-one correspondence between $d\ell/dN$ and ΔK_I.

For the crack trajectory closest to the hole (Case 1 in Fig. 2.4), the very concept of the existence of a functional relationship between $d\ell/dN$ and ΔK_I breaks down. Indeed, as Fig. 2.11 shows, there is a range of value of ΔK_I (roughly between 2.7 and 3.1 Mpa-$m^{1/2}$), over which there are three different crack speeds

corresponding to one value of ΔK_I. Similarly, there is a range of crack speed (between $2.8X10^{-6}$ and $28X10^{-6}$ m/cycle) over which there are three different values of stress intensity factor for each speed. In addition, one observes that there is no unique relation between da/dN and ΔK_I, if the three tests are compared.

Since we are dealing with a mixed mode crack, we also show the relation between the crack speed and ERR for each of the three cases (Fig. 2.12). For the crack farthest from the hole (Case 3), there is a unique relationship - monotonic with monotonically increasing slope - as commonly observed. For the intermediated Case 2, the relation is still monotonic, but the slope is not monotonic any more. Finally, for the crack trajectory closest to the hole, there is no functional relation at all between the crack speed and the ERR. Moreover, the difference in crack propagation speed for the range of the normalized ERR > 16 mm (see Fig. 2.12) indicates a strong effect of crack growth history.

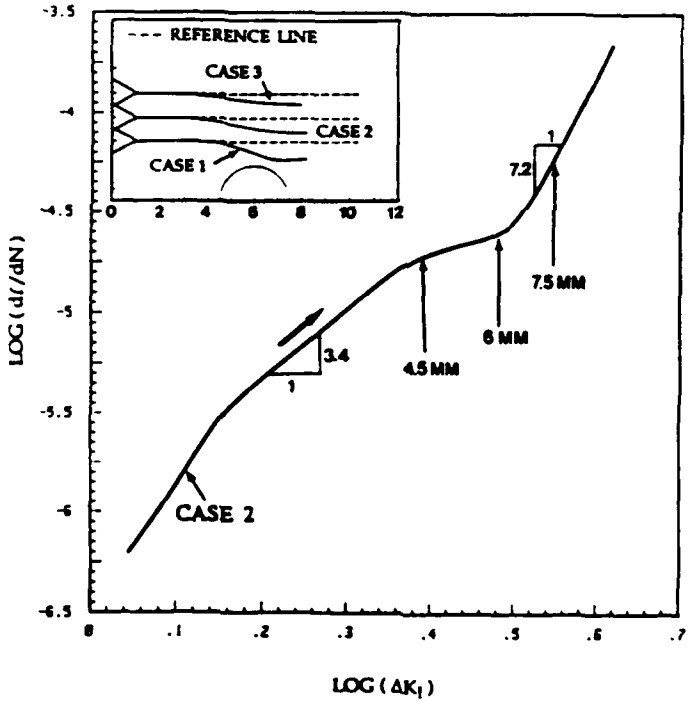

Figure 2.10 Crack speed da/dN for the intermediate crack trajectory (Case 2 in Fig. 2.4) in relation to the corresponding stress intensity factor increment ΔK_I in a log-log plot. The relation is obtained from Figs. 2.5 and 2.6. The thick arrow above the curve means the same as in Fig. 2.9.

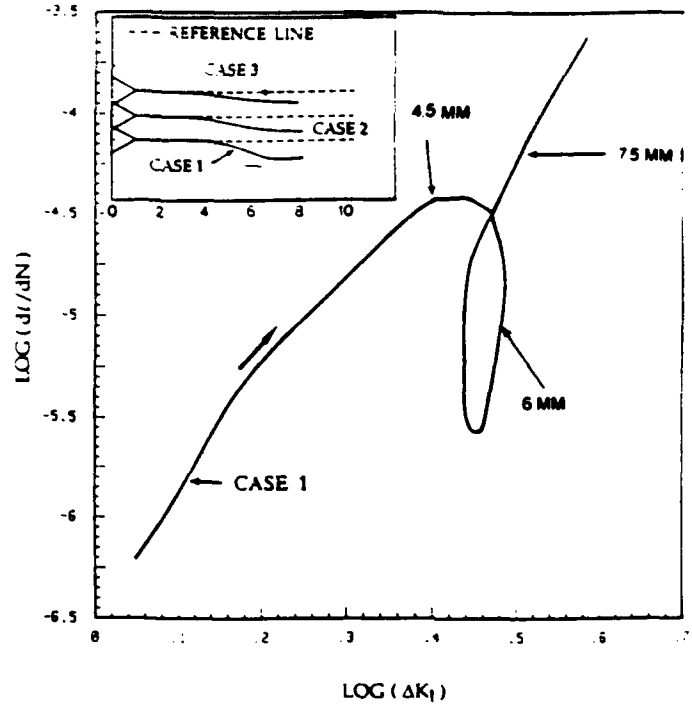

Figure 2.11 Crack speed $d\ell/dN$ for the closest to the hole crack trajectory (Case 1 in Fig. 2.4) in relation to the corresponding stress intensity factor increment ΔK_I in a log-log plot. The relation is obtained from Figs. 2.5 and 2.6. The thick arrow above the curve means the same as in Fig. 2.9.

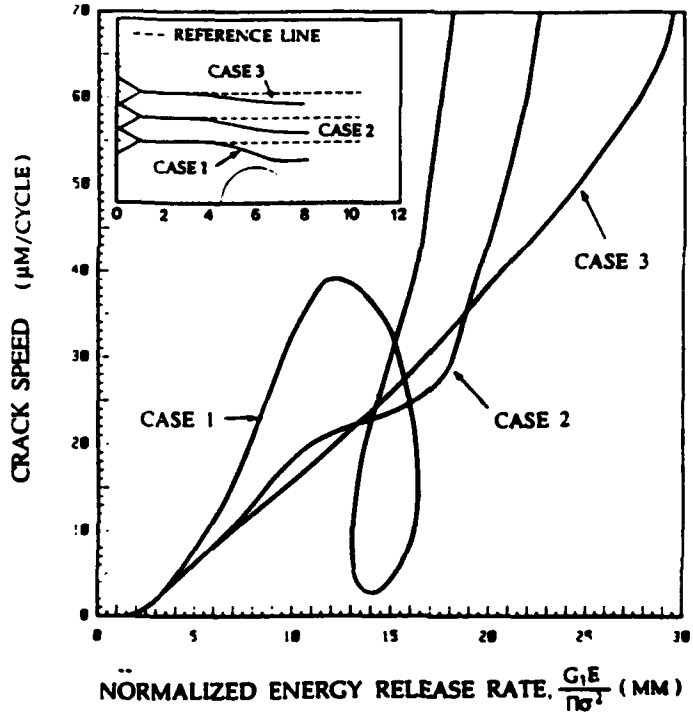

Figure 2.12 Crack speed $d\ell/dN$ for the three tests in relation to the corresponding energy release rates. The relations are obtained from Figs. 2.5 and 2.8.

Apparently, the stress intensity factors or the ERR are not the only parameters responsible for the crack growth rate. Our observation indicate that AZ morphology plays an important role in the determination of the crack speed. IN what follows, we elaborate on this statement.

It should be noted that the crack speed measurements obtained from video recording are not highly accurate. Therefore, we have repeated the key experiment (Case 1) at high stress level, (σ_{max} = 0.45 σ_f , $\sigma_{min}/\sigma_{max}$ = 0.1) which allowed a cross-examination of crack speed measurements from the video recording by those made from a 160X micrograph of the fracture surface and the side view, both carrying clear marks of crack tip positions. Also the AZ evolution was followed in more detail.

Figure 2.13 represents the $d\ell$ /dN-vs.-G_1 curve for the above test with an addition of the schematic pictures of the AZ at various stages of the main crack growth. For each AZ position, we show the crack growth direction, AZ overall shape, and craze orientation within AZ. As before, there is a range 13 < G_1 <1[illegible] [mm], where there is no one-to-one correspondence between $d\ell$/dN and G_1. This statement has been carefully checked and holds even if the two lower portions of the curve over this range are not distinguished (the difference of the speed values is on the borderline of the experimental accuracy).

This observation indicates the necessity to incorporate parameters of AZ evolution into the equation of crack growth.

Damage Characterization and Active Zone Kinematics

A two-dimensional linear elastic solid containing a crack surrounded by a random array of microcracks is considered. It represented a particular case of crack layer [2]. A random array of microcracks can be visualized as follows. Let us consider N realizations of CL formed under identical loading conditions (see Fig. 2.14). It is observed that the configuration of the microcrack array varies from one realization to another. Thus a statistical characterization is required. The microcrack density with orientation θ can be introduced as follows (see Fig. 2.15):

$$\rho(\theta/\mathbf{x}) = \frac{1}{N}\sum_{m=1}^{N}\frac{1}{V}\sum_{k=1}^{n^m}\ell_m^k(\mathbf{x},q). \qquad (2.1)$$

Here ℓ_m^k in RHS is the length of a portion of k-th microcrack with orientation q belonging to the elementary cell V surrounding a point "$\mathbf{x}$", nm is the number of such microcracks in m-th realization of the microcrack array and N the number

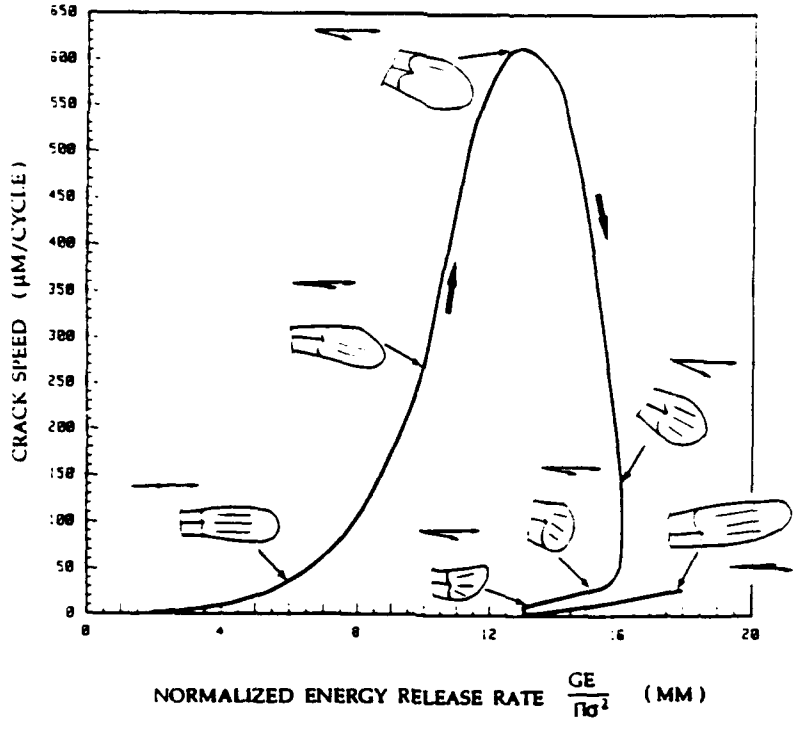

Figure 2.13 Crack speed dℓ/dN (N number of cycles) in relation to the corresponding energy release rate G_1. The thick arrow means the same as in Fig. 2.9. Shown along the curve are the shapes of AZ at various crack positions. In each of the AZ's, the corresponding distribution of craze orientations in the AZ is roughly indicated. The pair of arrows next to each AZ contour shows the main crack orientation: the long arrow is parallel to the reference line (see Fig. 2.4), and the short arrow shows the current direction of the crack at its tip.

number of realizations considered. The function $\rho(\theta/\mathbf{x})$ represents a histogram on the unit radius circle (sphere in 3-dimension). Employing conventional statistical analysis, we substitute the histogram by the corresponding angular distribution of microcrack density $\rho(\theta/\mathbf{x})$ at the given point "$\mathbf{x}$". If this distribution has an elliptical shape, it can be characterized by a second rank tensor [23]. If the shape of the distribution is more complex, the higher rank tensors can be utilized to approximate the distribution.

For most practical cases the size of V is much smaller than the microcracks (crazes) length and different directions of cracks or crazes within V are mutually exclusive. Therefore $\rho(\theta/\mathbf{x})$ can be presented by two Dirac's delta functions (to account for two faces):

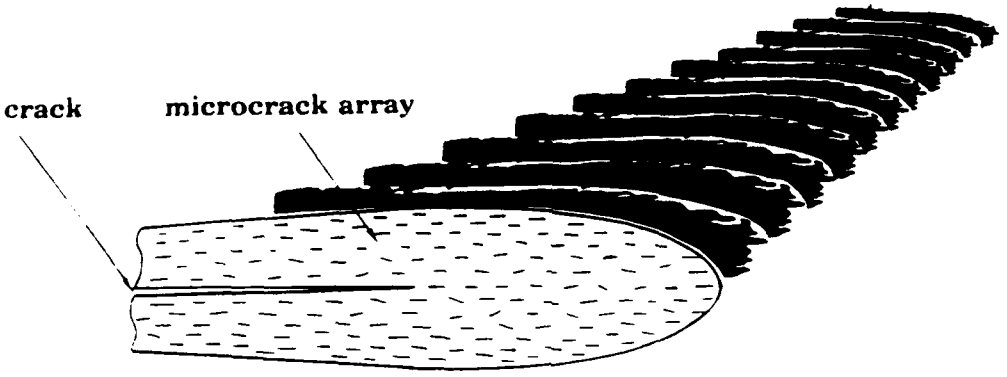

Figure 2.14 N realizations of crack layer under identical loading conditions.

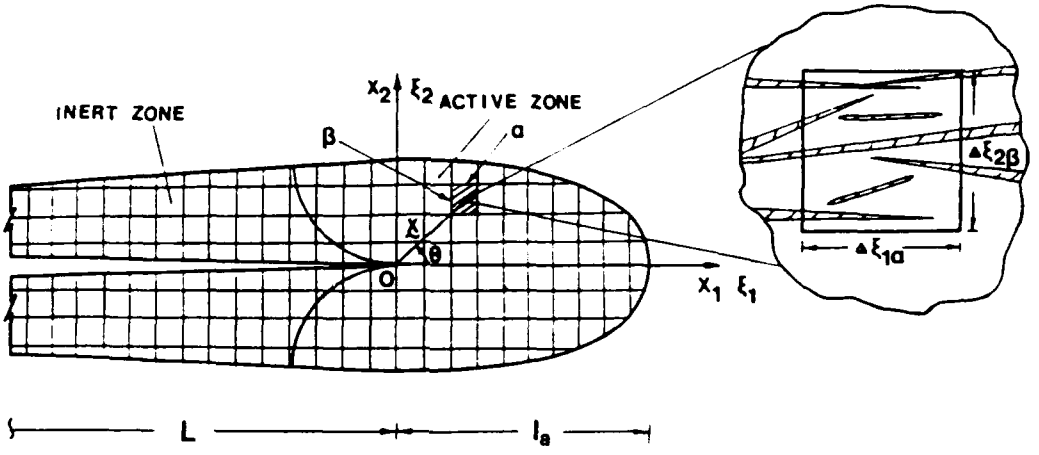

Figure 2.15 The schematic representation of the active and inert zone and the subdivision of the crack layer into a rectilinear mesh. The boundary between active and inert zone is illustrated following [7].

$$\rho(\theta/\mathbf{x}) = \frac{1}{2}\,\rho(\mathbf{x})\{\delta(\theta - \theta_*) + \delta(\theta - (\theta_*+\pi)\}, \tag{2.2}$$

where θ_* stands for a crack (craze) orientation.

It is convenient to normalize the angular distribution:

$$\rho(\theta/\mathbf{x}) = \frac{1}{2}\,\rho_0(\mathbf{x})\,\phi(\theta/\mathbf{x}), \tag{2.3}$$

where

$$\rho_0(\mathbf{x}) = \int_0^{2\pi} \rho(\theta/\mathbf{x})\,d\theta.$$

The latter represents the total microcrack density in a point "$\mathbf{x}$" and has dimension (m^2/m^3). This quantity can be directly measured (see for example [24,25,26]).

The fact that microcrack length is larger than the size of elementary cell, implies that the angular distribution of microcracks is not sufficient to formulate the microcracks interaction problem. Thus in addition to $\rho(\theta/\mathbf{x})$, we introduce a conditional probability distribution $\rho(\ell/\mathbf{x},\theta)$ of microcrack length $\ell(\theta)$ with orientation θ crossing V. Finally, the damage $D(\mathbf{x})$ at a given point $\mathbf{x}$ is characterized by the microcrack density $\theta_0(\mathbf{x})$, angular distribution $\phi(\theta/\mathbf{x})$ and the microcrack length distribution $D(\mathbf{x}) = \{\theta_0(\mathbf{x}), \phi(\theta/\mathbf{x}), \rho(\ell/\mathbf{x},\theta)\}$.

Figure 2.16a shows a micrograph of the AZ developed at about 820 cycles (see Fig. 2.2). At this stage the CL enters the domain of high stress gradient resulting from the CL-hole interaction.

We characterize the AZ morphology by the craze density distribution $\rho(\underline{\mathbf{x}})$ and the average AZ craze orientation ω. Specially, the craze density at a point $\underline{\mathbf{x}}$ is the total area of the craze middle planes within an elementary volume (its center at $\underline{\mathbf{x}}$) divided by V, thus the dimension of ρ is mm^2/mm^3. (In Fig. 2.16b, $\rho(\underline{\mathbf{x}})$ is represented by the contours of equal craze density.) The size of the elementary volume is chosen much smaller than the typical craze size, thus all crazes are parallel within V. Craze orientation at $\underline{\mathbf{x}}$ is the angle $\omega(\underline{\mathbf{x}})$ between the crazes in V and the direction tangent to the crack at its tip.

We integral the following integral parameters of crazing: total crazing within the AZ

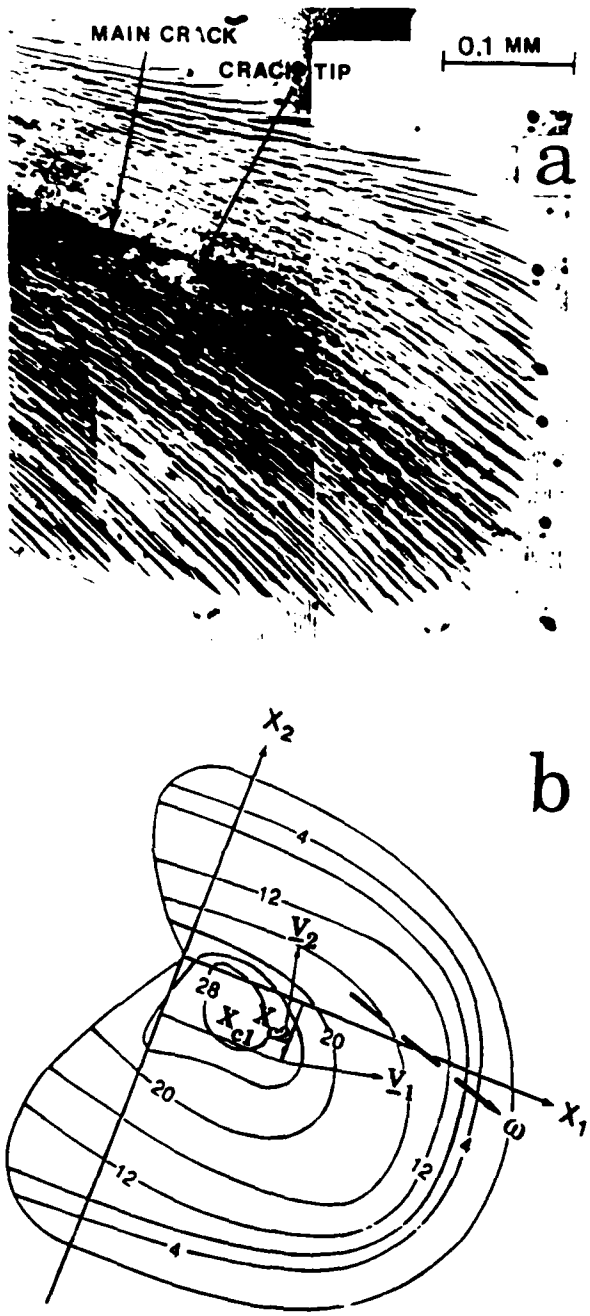

Figure 2.16 (a) A micrograph of the crazed zone ahead of the crack tip immediately after 820 cycles. (b) An outline of the AZ from the above micrograph; shown are: contours of equal craze density ρ [X 0.41 m^{-1}], position of the AZ gravity center $\underline{x}_c$, eigenvectors $\underline{v}_1$, $\underline{v}_2$ of the AZ central inertia moment matrix $\underset{\sim}{I}$, and the average AZ craze direction (dashed line).

$$R = \int_{V_{AZ}} \rho(\underline{x})\, dV,$$

the gravity center of the AZ (see Fig. 2.16b for an illustration)

$$x_{ci} = \frac{1}{R} \int_{V_{AZ}} x_i \rho(\underline{x})\, dV\ , \qquad i=1,2$$

the normalized "central inertia moment"

$$I_{ij} = \frac{1}{R} \int_{V_{AZ}} (x_i - x_{ci})(x_j - x_{cj})\rho(\underline{x})\, dV\ , \qquad i,j=1,2$$

(represented in Fig. 2.16b by its eigenvectors $\underline{v}_1, \underline{v}_2$) and the average craze orientation

$$\omega = \frac{1}{R} \int_{V_{AZ}} \omega(\underline{x})\rho(\underline{x})\, dV\ ,$$

represented by the dashed line in Fig. 2.16b. The advantage of such integral parameters is that they are insensitive to local fluctuation of craze density. Comparing the values of the above parameters for consecutive AZ position, one can evaluate the rate $\dot{\underline{x}}_c$, of AZ translation together with the rates of rotation and deformation (recovered from $\dot{\underline{I}}$, and $\dot{\omega}$, see [3] for details).

Our observations indicate that the crack speed near the hole is strongly correlated with evolution of AZ. For example, Fig. 2.17 shows that the crack speed $d\ell/dN$ reaches its maximum approximately at the same point ($x \approx 5$ mm) where the AZ area reaches its peak and, vice versa, $d\ell/dN$ reaches its minimum at the point ($x \approx 6.5$ mm) where the area also has a minimum. Also, it should be pointed out that crack deceleration coincides with a drastic mismatch between the average craze orientation and the crack propagation direction (see Fig. 2.18). In regard to this, it should be noticed that the changes in the average craze orientation represent only part of AZ rotation. The rest of it is associated with the rotation of the eigenvectors of AZ inertia moment $\underline{I}$.

For the conditions described above, the crack-damage interaction is the key problem for modeling crack layer growth.

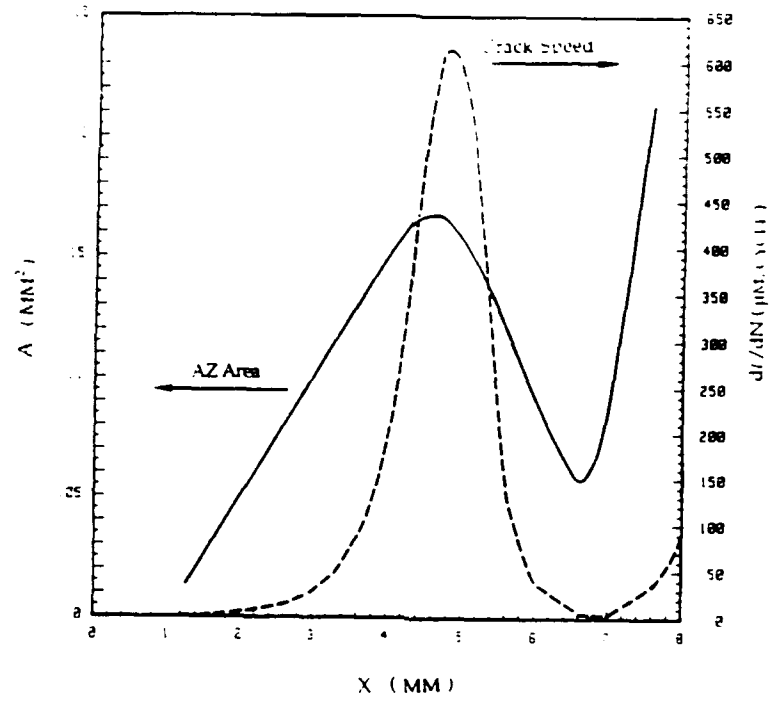

Figure 2.17 The Active Zone area A as a function of the crack tip position X (solid line) shown against the crack speed $d\ell/dN$ (N number of cycles) as a function of X (dashed line).

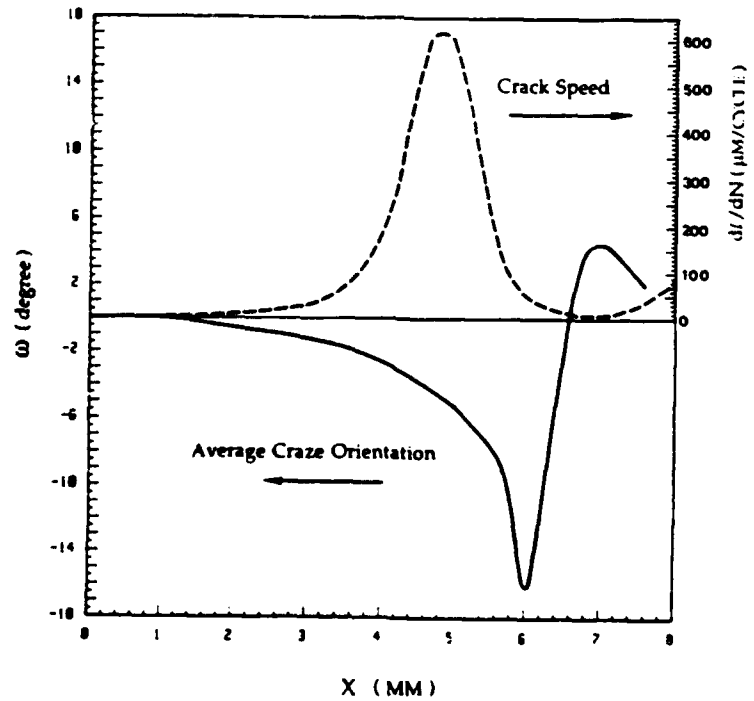

Figure 2.18 The average craze orientation ω as a function of the crack tip position X (solid line) shown against the crack speed $d\ell/dN$ (N number of cycles) as a function of X (dashed line).

CHAPTER 3

ELASTIC CRACK-DAMAGE INTERACTION PROBLEM

3.1 Elastic Interaction of a Crack with a Random Array of Microcracks

Introduction

As illustrated in the previous chapter, a damage zone (DZ) usually accompanies slow crack propagation under fatigue and creep conditions. In this chapter we consider a special case of a damage zone consisting of an array of localized discontinuities such as microcracks or crazes. Figure 3.1 illustrates an array of crazes formed in a vicinity of a fatigue crack in an amorphous polymer. Statistical distributions of microcrack densities, orientation and length appear to be the most appropriate characterization of such type of damage [3,4]. A hypothesis of a self-similarity of DZ, i.e., self-similarity of the statistical distributions at various stages of the DZ evolution has been first proposed theoretically [2] and then supported by experimental examinations [27,28]. The self-similarity hypothesis (SSH) yields a decomposition of the DZ propagation into elementary movements such as translation, rotation and deformation. The corresponding driving forces are represented by linear functions of the energy release rates (ERR) associated with the elementary movements [29]. This motivates the present study of crack-microcrack array interaction and an evaluation of ERR's resulting from the array translation, expansion etc.

Three approaches recently advanced to evaluate elastic fields associated with the presence of microcrack array in a vicinity of the main crack tip. The first approach models the microcrack array as an inclusion of an effective elastic media. This well posed boundary value problem of crack partially penetrating into a "softer inclusion" has been addressed by various authors [30-33]. However, there are various shortcomings in this approach from the physics stand point. First it does not account for local fluctuations of microcrack density and length, which is of primary importance for fracture process. Secondary, the relationship between the statistics of the microcrack array in the vicinity of the main crack and the effective elastic constants is, in general, unknown. Determination of such relationship is equivalent to solving the crack-microcrack interaction problem. Besides that, the distribution of microcracks in the array is usually a heterogeneous one. To reflect that, an equivalent elastic inclusion should be nonhomogeneous and anisotropic one that would lead to certain computational difficulties.

The second approach to crack-microcrack interaction uses a detail description of the location, size and orientation of every microcrack in every particular realization of the microcrack array [34-39]. Apparently, this leads to a computational limitation and the method becomes impractical for an array similar to one shown in Fig. 3.1.

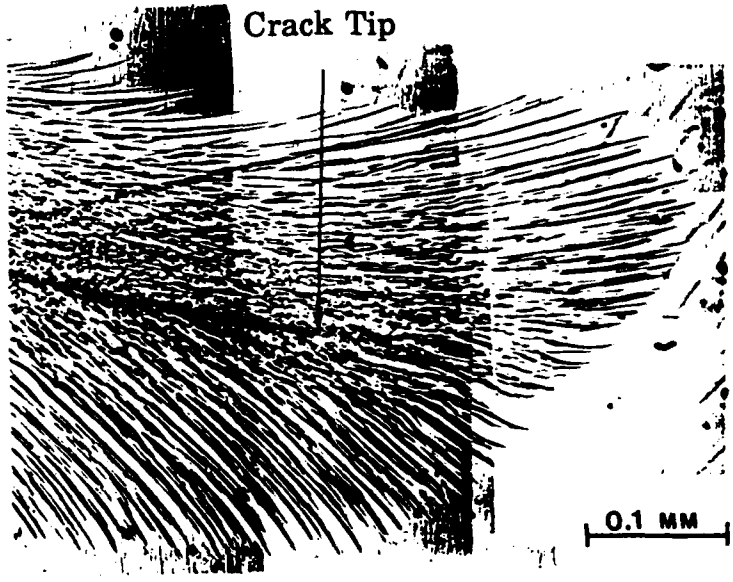

Figure 3.1 The optical micrograph displaying the damage zone (craze array) near the crack tip in an amorphous polymer.

The third approach characterize the microcrack array by statistical distributions of microcrack densities, sizes and orientation. It leads to evaluation of integral (average) parameters associated with microcrack array [4,7,40,41]. The present paper follows the third approach and is a continuation of our previous work.

The statistical distributions of the microcrack lengths as well as the distance between the microcracks, their locations and orientations with respect to the main crack are essential for the interaction problem. We employ a characterization of a random array of microcracks in terms of distributions of the size, orientation and density of microcracks proposed by [4]. Specifically we characterize the damage at a given point $\underset{\sim}{x}$ by the microcrack density $\rho_0(\underset{\sim}{x})$, angular distribution $\varphi(\theta/\underset{\sim}{x})$ and the distribution of length of microcracks $\rho(\ell/\underset{\sim}{x}, \theta)$ with orientation θ. The microcrack density

$\rho_0(\underset{\sim}{x})$ is defined as 1/2 of crack surfaces per unit volume and has dimension m^{-1}. Apparently, it is different from dimensionless "microcrack density" ε conventionally used in damage mechanics. A corresponding quantity in our case is microcrack concentration $\rho\ell$. The relationship between $\rho\ell$ and the effective elastic constants for "dilute" microcrack concentration in 2-D case can be easily found [8].

Two issues are addressed in this paper. The first is a formulation and solution of crack-microcrack array interaction problem in terms of the above distributions. It is based on the Green's function of linear elasticity for a dislocation dipole placed in a vicinity of the main crack tip given by [42]. The second is an evaluation of ERR's. The effect of the distributions of microcrack density, length and orientation on the SIF and the ERR's due to microcrack array is illustrated on examples.

Formulation of the Problem

The linear elastic interaction of crack microcrack array can be obtained by the superposition method based on the Green's function "G" for a dislocation dipole interacting with a crack. Microcrack opening displacement is conventionally represented by a continuous distribution $\underset{\sim}{b}(\underset{\sim}{\xi})$ of dislocation dipoles. Thus the stress, displacement and SIF of the main crack due to a particular microcrack (ℓ_0) can be expressed as:

$$\underset{\sim}{u}(\underset{\sim}{x}) = \int_{\ell_0} \underset{\sim}{b}(\underset{\sim}{\xi})\underset{\sim}{\Phi}(\underset{\sim}{x},\underset{\sim}{\xi})\, d\underset{\sim}{\xi}, \quad \underset{\sim}{\sigma}(\underset{\sim}{x}) = \int_{\ell_0} \underset{\sim}{b}(\underset{\sim}{\xi})\underset{\sim}{F}(\underset{\sim}{x},\underset{\sim}{\xi})\, d\underset{\sim}{\xi} \tag{3.1}$$

$$K = \int_{\ell_0} \underset{\sim}{b}(\underset{\sim}{\xi})\, \underset{\sim}{G}_{SIF}(\underset{\sim}{\xi})\, d\underset{\sim}{\xi}$$

Where the influence functions $\underset{\sim}{\Phi}$, $\underset{\sim}{F}$ and $\underset{\sim}{G}_{SIF}$ are obtained by simple transformations of the Green's function G [41]. Then by means of the superposition principle, the stress, displacement and stress intensity factor due to a microcrack array can be obtained by integrating Eq. (3.1) over the domain V occupied by the array with microcrack density ρ as a weight function.

$$\underset{\sim}{u}^A(\underset{\sim}{x}) = \int_V \underset{\sim}{\rho}(\underset{\sim}{\xi})\, \underset{\sim}{b}(\underset{\sim}{\xi})\, \underset{\sim}{\Phi}(\underset{\sim}{x},\underset{\sim}{\xi})\, d\underset{\sim}{\xi}, \quad \underset{\sim}{\sigma}(\underset{\sim}{x}) = \int_V \underset{\sim}{\rho}(\underset{\sim}{\xi})\underset{\sim}{b}(\underset{\sim}{\xi})\, \underset{\sim}{F}(\underset{\sim}{x},\underset{\sim}{\xi})\, d\underset{\sim}{\xi} \tag{3.2}$$

$$K^A = \int_V \underset{\sim}{\rho}(\underset{\sim}{\xi})\, \underset{\sim}{b}(\underset{\sim}{\xi})\, \underset{\sim}{G}_{SIF}(\underset{\sim}{\xi})\, d\underset{\sim}{\xi}$$

The integrals in Eq. (3.2) are well defined if the microcrack concentration $\rho\ell$ tends to zero faster than $r^{1/2}$.

$$\lim_{r \to 0} r^{-1/2} \rho(r)\, \ell(r) = 0 \tag{3.3}$$

We consider below the case when this condition is satisfied.

The elastic fields in a vicinity of the main crack surrounded by a process zone can be expressed as a sum:

$$\underset{\sim}{u} = \underset{\sim}{u}^C + \underset{\sim}{u}^A, \quad \underset{\sim}{\sigma} = \underset{\sim}{\sigma}^C + \underset{\sim}{\sigma}^A \tag{3.4}$$

$$K = K^0 + K^A$$

where $\underset{\sim}{u}^C$, $\underset{\sim}{\sigma}^C$ and K^0 are the displacement, stress and SIF due to the main crack under the remote loading $\underset{\sim}{\sigma}^0$ respectively. Thus the traction free condition on the main crack is met since both terms in Eq. (3.4) satisfy it, the remote loading boundary condition is satisfied by the first terms in Eq. (3.4). The remaining boundary conditions, i.e., the traction free faces of the microcracks are met by solving a system of corresponding integral equations with respect to $\underset{\sim}{\sigma}^A$ and K^A.

The equations are written for every microcrack embedded into an effective stress field. The latter is defined as following. Let us consider the effective stress $\underset{\sim}{\sigma}^{eff}$ along the i-th microcrack line generated by the main crack and the rest of microcracks in absence of i-th microcrack:

$$\underset{\sim}{\sigma}^{eff}(\underset{\sim}{x}) = \underset{\sim}{\sigma}^C(\underset{\sim}{x}) + \sum_{j \neq i}^{M} \int_{\ell^{(j)}} \underset{\sim}{b}^{(j)}(\underset{\sim}{\xi})\, \underset{\sim}{\underset{\sim}{F}}(\underset{\sim}{x}, \underset{\sim}{\xi})\, d\underset{\sim}{\xi} \tag{3.5}$$

Then applying $-\underset{\sim}{\sigma}^{eff}(\underset{\sim}{x}) \cdot \underset{\sim}{n}(\underset{\sim}{x})$ on i-th microcrack faces, we satisfy the traction free requirement for i-th microcrack. Applying this treatment to every microcrack, one obtains the system of integral equations. For simplicity, we assume $\underset{\sim}{\sigma}^{eff}(\underset{\sim}{x})$ being constant on the microcrack scale. Then the relation between the effective stress and the microcrack opening displacement is well known:

$$\underset{\sim}{b} = \frac{\pi\ell}{E}\, \underset{\sim}{\sigma}^{eff} \cdot \underset{\sim}{n} \tag{3.6}$$

Combining Eqs (3.5) and (3.6), we obtain a system of integral equation with respect to the unknown b functions. Solution of these equations leads to the solution of the interaction problem.

Substituting the summation in Eq. (3.5) by the integration over V with weight function $\rho(\underset{\sim}{x})$ and employing a conventional regularization of the singular integrals in Eq. (3.2) (see [39] for details), we rewrite equations (3.5) as:

$$\underset{\sim}{\sigma}^{eff}(\underset{\sim}{x}) = \underset{\sim}{\sigma}^{c}(\underset{\sim}{x}) + \int_{v} \underset{\sim}{\rho}(\underset{\sim}{\xi})\,[\underset{\sim}{b}(\underset{\sim}{\xi}) - \underset{\sim}{b}(\underset{\sim}{x})]\,\underset{\sim}{F}(\underset{\sim}{x},\underset{\sim}{\xi})\,d\underset{\sim}{\xi} \tag{3.7}$$

Finally, combining the equations (3.6) and (3.7), we obtain the following equation for the unknown microcrack opening displacement vector $\underset{\sim}{b}(\underset{\sim}{x})$:

$$\underset{\sim}{b}(\underset{\sim}{x}) = \frac{\pi \ell(\underset{\sim}{x})}{E}\,\underset{\sim}{\sigma}^{c}\cdot\underset{\sim}{n} + \frac{\pi \ell(\underset{\sim}{x})}{E}\,\{\int_{v} \underset{\sim}{\rho}(\underset{\sim}{\xi})\,[\underset{\sim}{b}(\underset{\sim}{\xi}) - \underset{\sim}{b}(\underset{\sim}{x})]\,\underset{\sim}{F}(\underset{\sim}{x},\underset{\sim}{\xi})\,d\underset{\sim}{\xi}\}\cdot\underset{\sim}{n} \tag{3.8}$$

Apparently from Eq. (3.8) the components b_k of an average vector opening $\underset{\sim}{b}(\underset{\sim}{x})$ at point "$\underset{\sim}{x}$" can be viewed as the sum of the opening due to the main crack with remote load and due to the microcrack array in presence of the main crack. The integral in Eq. (3.8) can be divided into summation by employing the same method described in [4]. Thus Eq. (3.8) can be reduced to two system of algebraic equations with respect to the components of microcrack opening displacement b_1 and b_2:

$$\begin{aligned} \lambda_{11}B_1 + \lambda_{12}B_2 &= F_1 \\ \lambda_{21}B_1 + \lambda_{22}B_2 &= F_2 \end{aligned} \tag{3.9}$$

Where B_1 and B_2 are the columns matrix consisting of the value of microcrack openings b at points of discretization. Matrix λ_{ij} and F_i are known functions of the microcrack density, length distribution and the elastic properties of the undamaged material. The equation (3.9), in principle, can be solved by a numerical technique. However, the singularity of the effective stress at the crack tip creates an obstacle for the computation. To overcome this problem, we decompose the effective stress $\underset{\sim}{\sigma}^{eff}$ into a singular and a regular ones:

$$\underset{\sim}{\sigma}^{eff}\,\underset{\sim}{x} = \frac{K^{eff}}{\sqrt{2\pi r}}\,\underset{\sim}{\varphi}(\theta) + \underset{\sim}{\sigma}_0^{eff}(\underset{\sim}{x}) \tag{3.10}$$

The form of the singular part of the effective stress is based on the analytical solution with unknown K^{eff}. The regular part of the effective stress are obtained numerically. If the microcrack orientation is statistically isotropic at every point of the active zone, the effective stress singularity is expected to be the same as conventional singularity in an isotropic material. For an anisotropic statistics, i.e., for a microcrack array with a dominant orientation, the singularity of stress field is expected to resemble that in a media with the corresponding anisotropy. Then, the order of singularity is still the same ($r^{-1/2}$), but the angular distribution of stress $\underset{\sim}{\varphi}(\theta)$ depends on the particular anisotropy.

Knowing the $\underset{\sim}{b}(\underset{\sim}{x})$ field, the SIF K_I^{eff}, the elastic fields $\underset{\sim}{u}(\underset{\sim}{x})$ and $\underset{\sim}{\sigma}(\underset{\sim}{x})$ can be radially reconstructed by Eqs. (3.2) and (3.4).

Crack-microcrack Interaction

Example 1. In this example we compare the SIF calculated using our scheme with that obtained by modeling a microcrack array as an elastic inclusion with isotropic effective elastic properties. A circular shape damage zone and the corresponding inclusion are considered. The elastic properties of the inclusion are chosen as effective properties of an elastic media perforated by microcrack array with constant microcrack concentration ($\rho\ell$ = constant). For computational purpose we select the ratio of the radius of damage zone and the main crack length R/L = 0.1. All the microcracks are parallel to the main crack, so the singular part of the resulting effective stress field similar to that for an orthotropic material where the orthotropic property comes from the distribution of microcracks [8]. A low microcrack density case, the range $0 < \rho\ell < 0.2$ is considered to examen the effect of microcrack array on the SIF. It should be noted that the above microcrack concentration is different from commonly used microcrack densities "ε" [32]. Here, the relation between the effective elastic properties and the microcrack concentration is taken from [8] for two dimensional case. Considering the equation (3.2), the effective SIF can be expressed as following:

$$K^{tot} = K^0 + K^A = K^0 + \int_V \underset{\sim}{\rho}(\underset{\sim}{\xi})\,\underset{\sim}{b}(\underset{\sim}{\xi})\,\underset{\sim}{G}_{SIF}(\underset{\sim}{\xi})\,d\underset{\sim}{\xi} \tag{3.11}$$

The dependence of SIF on microcrack concentration $\rho\ell$ is shown in Fig. 3.2 by solid line. The dotted line represents SIF of Hutchinson [32] whose result given in terms of the ratio of the initial and effective Young's modular of material has been reformulated in terms of the microcrack concentration. It should be emphasized that the Huchinson's [32] results is obtained for an isotropic inclusion which can be considered as a model of an isotropically distributed microcrack array. For the case when all microcracks are parallel to the main crack, our solution should be compared with an anisotropic inclusion problem. However, to our knowledge, the SIF for a crack partially penetrating an anisotropic inclusion is not known, therefore we compare our results with the closest available solution. It is expected that shielding of parallel microcrack array is higher than the randomly distributed microcracks, i.e., K_I^{eff} of our solution is smaller than K_I^{eff} given by [32].

The main advantage of the method described above is that it can deal with crack-damage interaction equally well for uniform and nonuniform distributions of microcracks. As soon as the microcrack density $\underset{\sim}{b}(\underset{\sim}{x})$ and the microcrack length distribution $\underset{\sim}{\ell}(\underset{\sim}{x})$ are given (e.g., measured by experimental means), the interaction problem can be solved using the same numerical procedure as above. This statement is illustrated in the next example.

Example 2. Let us consider a specimen of the same geometry and loading condition as in an experiment reported by [24] (a SEN specimen of an amorphous polymer with Young's modulus E=2.2GPa, Poisson's ratio υ=0.3, applied load σ_{22}=16MPa). The evolution of the damage zone was monitored by a video recording system attached to an optical microscopy. It should be noticed that the damage reported by [24] consists of crazes. In our example the crazes are substituted by microcracks. The calculation is performed for the microcrack array whose density coincides with the observed craze density and length distribution resembles that of crazes.

The microcrack density $\rho_0(\underset{\sim}{x})$ employed is shown in Fig. 3.3a. The distribution of mathematical expectation of microcrack length is chosen as an extrapolation of the peripheral craze length distribution:

$$\underset{\sim}{\ell}(\underset{\sim}{x}) = 0.06\left(\frac{x_1}{L_a}\right)^{\alpha} + 0.15\left(\frac{x_2}{w}\right)^{\alpha} \qquad \text{if } x_1 > 0$$

$$\underset{\sim}{\ell}(\underset{\sim}{x}) = 0.15\left(\frac{x_2}{w}\right)^{\alpha} \qquad \text{if } x_1 < 0 \qquad (3.12)$$

where ℓ_a and w are the length and half width of the active zone respectively. Using the numerical procedure as described above the effective stress field is constructed for such microcrack array. The result of numerical computation for $\alpha=2$ is presented in Fig. 3.3b, which displays the σ_{22}^{eff} component of the effective stress field. Other component of the effective stress as well as the microcrack opening distribution are reported in [4]. The effective SIF K_I^{eff} here is $K_I^{eff} = 0.88\ K_I^0$, where K_I^0 stands for SIF of the main crack without the damage zone.

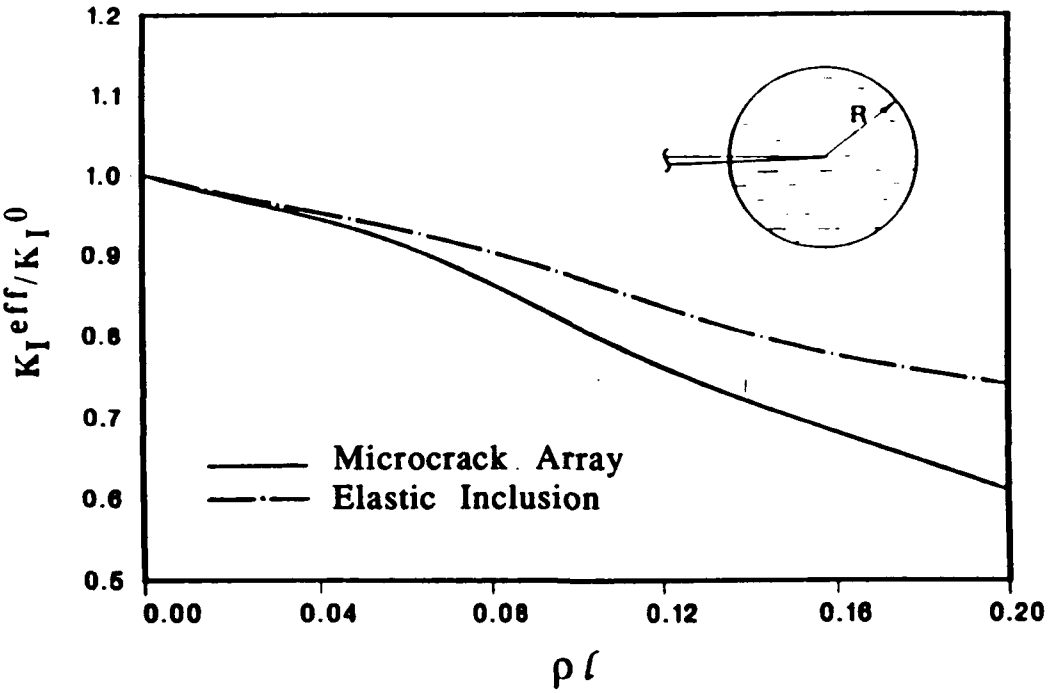

Figure 3.2 The dependence of K_I^{eff} on the microcrack concentration $\rho\ell$.

Evaluation of Energy Release Rates

An elegant approach of evaluating the elastic energy changes due to initiation and growth of defects was outlined by [43,44]. Following his approach one can express the energy release associated with the process zone translation, expansion etc. in terms of Eshelby tensor $\underset{\sim}{P}$. For example, the ERR J_k due to "translation" of the damage zone can be written as:

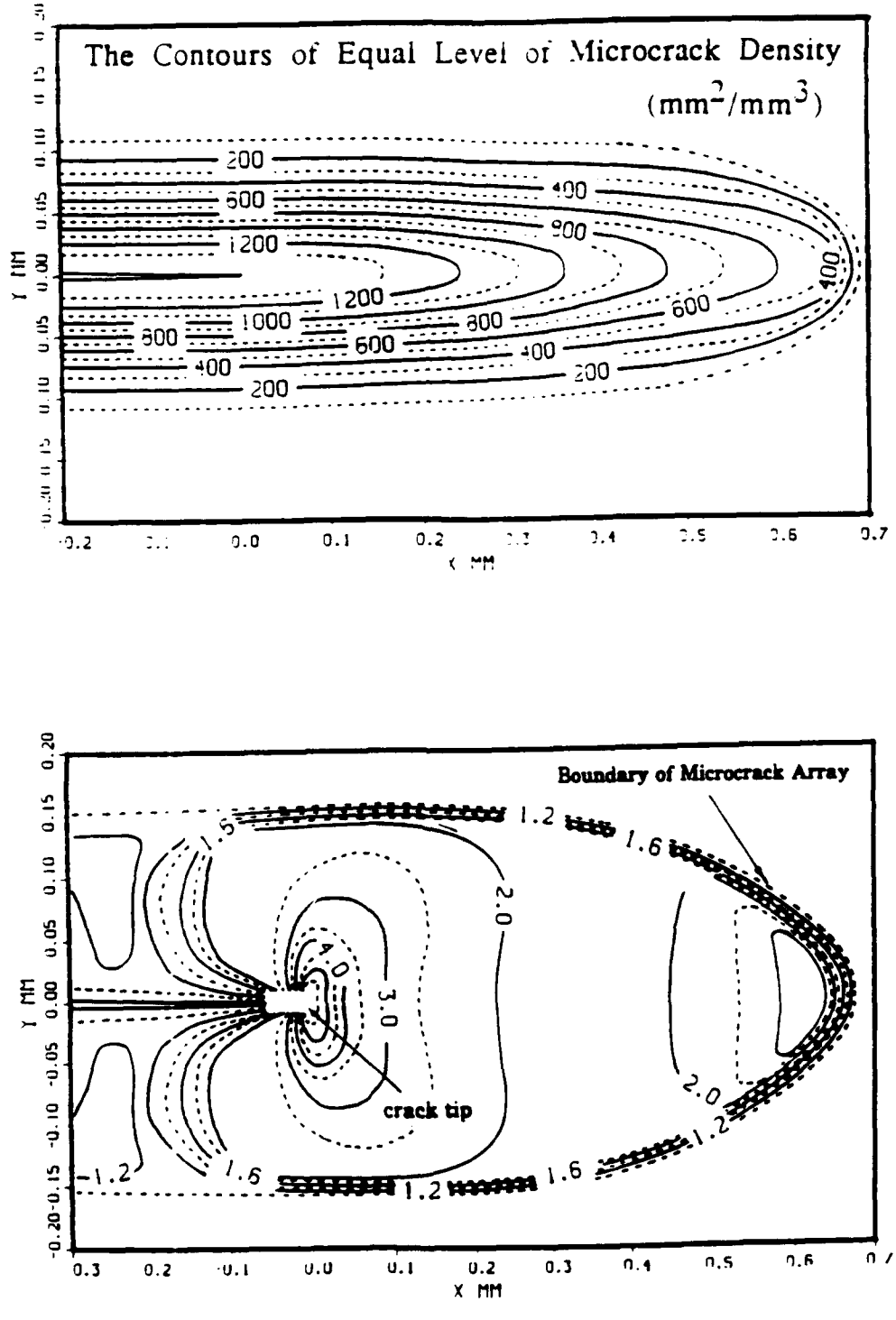

Figure 3.3 (a) The contours of equal level of microcracks density $\rho_0(x)$ (mm^2/mm^3) in the active zone. The dot lines correspond to the intermediate values of $\rho_0(x)$;
(b) The contour of the equal level of normalized effective stress $\sigma_{22}^{eff}/\sigma_{22}^{0}$ in the damage zone for $\alpha=2$.

$$J_k = \int_V \partial_j P_{kj}\, dV\,; \quad P_{kj} = f\delta_{kj} - \sigma^*_{ji}\, u_{i,k} \tag{3.13}$$

Here V is the domain occupied by the damage zone, $\underset{\sim}{\sigma}^*$ is Piola-Kirchhoff stress tensor and f is the strain energy density. To evaluate Eq. (3.13) one needs to know the elastic fields σ and u of the interaction problem discussed in the previous chapter.

Below we consider only the energy release associated with translation of the damage zone. Let us decomposed the DZ into N_α x N_β elementary cells (see Fig. 3.4). Then the integral over V in Eq. (3.13) can be rewritten as:

$$J_1 = \sum_{\alpha=1}^{N_\alpha} \sum_{\beta=1}^{N_\beta} \int_{V_{\alpha\beta}} \partial_1 P_{1j}\, dV \tag{3.14}$$

where $V_{\alpha\beta}$ is the volume of the elementary cell. Since $\partial_j P_{1j} = 0$ within a homogeneous domain, the area integral in Eq. (3.14) can be converted into a path integral by means of Gauss Theorem:

$$\int_{V_{\alpha\beta}} \partial_1 P_{1j}\, dV = \int_{\Gamma_{\alpha\beta}} P_{1j}\, n_j\, d\Gamma \tag{3.15}$$

where $\Gamma_{\alpha\beta}$ is the total boundary of the elementary cell $V_{\alpha\beta}$. $\Gamma_{\alpha\beta}$ consists of the surfaces ${\Gamma_{\alpha\beta}}^{cracks}$ of microcracks penetrating the elementary cell, the boundaries ${\Gamma_{\alpha\beta}}^{int}$ between $V_{\alpha\beta}$ and the neighboring cells and a part ${\Gamma_{\alpha\beta}}^{ext}$ of external boundary V when the elementary cell $V_{\alpha\beta}$ is one of the extreme peripheral cells of the active zone. When the summation in Eq. (3.14) is performed, the integrals over ${\Gamma_{\alpha\beta}}^{int}$ cancel each other since there are always two opposite directions of integration. The summation of the integrals over ${\Gamma_{\alpha\beta}}^{ext}$ results in the integral over the boundary of the active zone V. The integrals over traction free rectilinear microcrack surfaces are vanishing everywhere except the microcrack tips. There are two types of those integral paths, i.e., Γ^+ and Γ^- (see Fig. 3.4). The integrals in the RHS of Eq. (3.15) over Γ^+.and Γ^- represent the energy release rates ${G_1}^+$ and ${G_1}^-$ respectively. For small microcrack density one may employ a piece-wise constant approximation of σ^{eff} on the scale of microcrack length "ℓ." It results in the following expression for ERR:

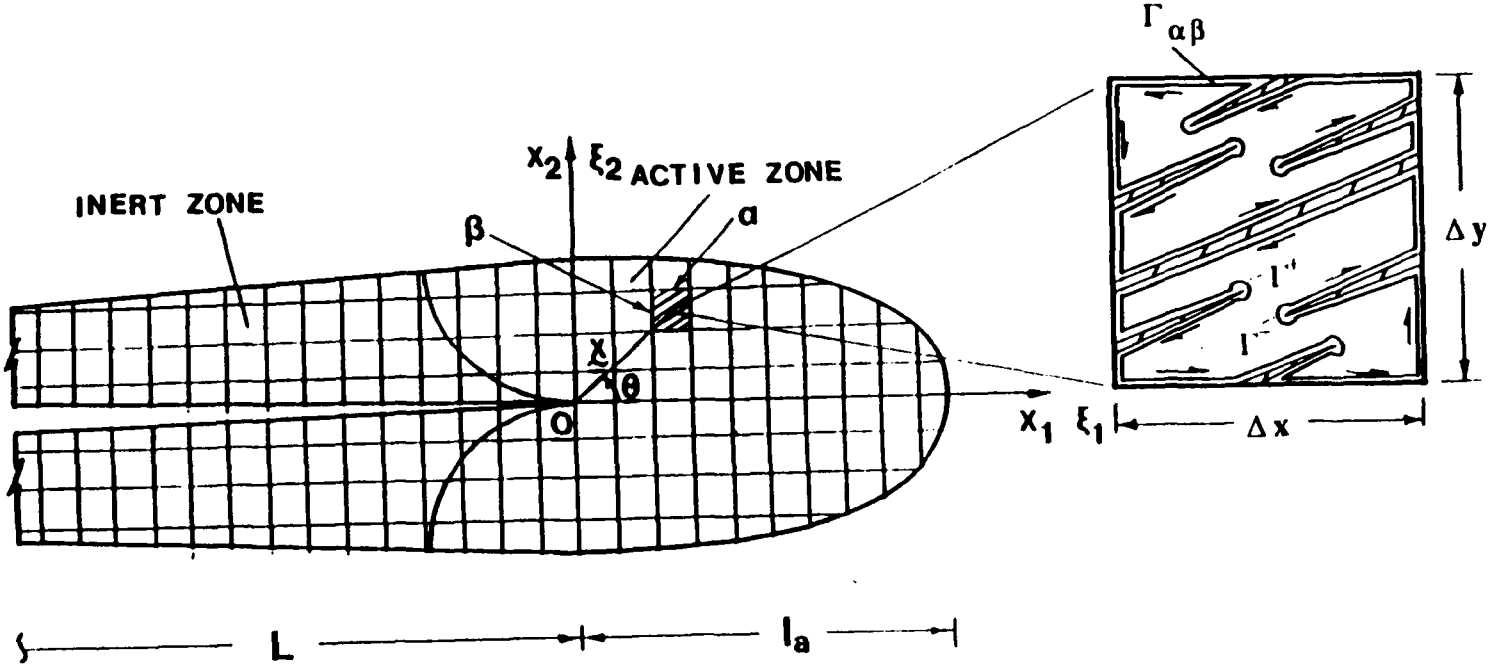

Figure 3.4 The schematic representation of the damage zone and the subdivision of the DZ into a set of the elementary cells, and the paths of integration within an elementary cell.

$$G_1^{\pm} = \pm \frac{\pi <\ell>}{E} [(\underset{\sim}{n} \cdot \underset{\sim}{\sigma}^{eff} \cdot \underset{\sim}{n})^2] + [(\underset{\sim}{\tau} \cdot \underset{\sim}{\sigma}^{eff} \cdot \underset{\sim}{\tau})^2] \tag{3.16}$$

With "+" and "-" correspond to the Γ^+ and Γ^-, respectively. In the total sum G_1^+ and G_1^- balance each other except: (a) when there is an unbalance in numbers of the "left" (-) and "right" (+) microcrack tips (see Fig. 3.4) and (b) there is a difference in the mathematical expectation of the microcrack length on the left and right size of the elementary cell under consideration. The first is associated with the gradient of the microcrack density ρ and the second with the gradient of the mathematical expectation of crack length $<\ell>$ crossing a given point. The summation in Eq. (3.14) in the limit of N_α and N_β approaching zero gives the final expression of ERR due to translation of the damage zone:

$$J_1 = \int_{\partial V} \partial P_{1j}\, n_j\, d\Gamma - \int_V \frac{\pi}{E} \cos\theta [(\underset{\sim}{n} \cdot \underset{\sim}{\sigma}^{eff} \cdot \underset{\sim}{n})^2] + [(\underset{\sim}{\tau} \cdot \underset{\sim}{\sigma}^{eff} \cdot \underset{\sim}{\tau})^2]$$
$$[\ell(\cos\theta\, \partial_1\rho + \sin\theta\, \partial_2\rho) + \rho(\cos\theta\, \partial_1\ell + \sin\theta\, \partial_2\ell)]\, dV \tag{3.17a}$$

where θ is the average orientation of the microcracks.

Considering a high craze density case, we utilize the solution in Tada [45] for a craze in a thin strip of width $h=1/\rho$ instead of piecewise constant approximation of $\underset{\sim}{\sigma}^{eff}$. The boundary condition is related to the craze formation stress $\underset{\sim}{\sigma}^{tr}$ which is a material parameter. Then the ERR due to translation of the damage zone can be expressed as:

$$J_1 = \int_{\partial V} \partial P_{1j}\, n_j\, d\Gamma - \int_V \frac{\cos\theta}{\rho E} [(\underset{\sim}{n} \cdot \underset{\sim}{\sigma}^{tr} \cdot \underset{\sim}{n})^2] + [(\underset{\sim}{\tau} \cdot \underset{\sim}{\sigma}^{tr} \cdot \underset{\sim}{\tau})^2]\, (\cos\theta\, \partial_1\rho + \sin\theta\, \partial_2\rho)]dV \tag{3.17b}$$

We have performed the computation of Eq. (3.17b) for the craze array reported in [24] . The total ERR J_1 consists two parts, one path integral J_{1G} and one volume integral J_{1V}:

$$J_1 = J_{1\Pi} + J_{1V} = 0.86\, G_1^0 + 0.54 G_1^0 \tag{3.18}$$

where G_1^0 is the ERR of the main crack with no damage zone ($G_1^0 = (K_I^0)^2/E$). The volume integral depends on the craze formation stress $\underset{\sim}{\sigma}^{tr}$ which is $1.6\underset{\sim}{\sigma}^{\infty}$ in above example.

Summary

(1). The interaction between main crack and surrounding microcrack array is formulated in terms of the distributions of the microcrack density and the mathematical expectation of microcrack length. The formulation is based on the analytical solution of the interaction between a crack and a dislocation dipole. The approach is illustrated by a special case of a circular damage zone with a constant microcrack concentration and all microcracks being parallel to the main crack. The shielding effect of the microcrack array here is compared with that of an elastic inclusion. It is shown that an isotropic elastic inclusion model underestimates the shielding.

(2). A more realistic microcrack array configuration is considered in the second example. In this case the effective stress field within the damage zone is decomposed into singular and regular parts. The singular part with unknown effective stress intensity factor is taken from the asymptotic solution of a crack in an anisotropic material where anisotropy corresponds to effective elastic properties of cracked material. The regular part of $\underset{\sim}{\sigma}^{eff}$ is determined from self consistency equation.

(3). A new technique to evaluate the ERR associated with the damage zone translation is formulated. The ERR consists of two parts. The first part is represented by a path integral similar to conventional J_1 integral. The second part is represented by an integral over the DZ domain and depend on the geometry of the process zone and the statistical distribution of microcrack density, length and orientation.

(4). The total ERR associated with translation of the damage zone is characterized by the microcrack density and length distributions. Computation of ERR for the particular craze array indicates that the ERR due to damage zone advance is the same order of magnitude as G_1^0 .

3.2 Effective Elastic Properties of Elastic Solid with Microcracks

Introduction

Effective elastic properties of an elastic solid containing many microdefects are often discussed in composite materials and continuum damage mechanics. In continuum damage mechanics, effective elastic properties of elastic solids with microdefects sometimes are used as a measure of damage. A brief review of an effective elastic properties evolution for an elastic solid with microcracks can be found for example in [46]. Recently, the relation between damage and effective elastic properties was discussed by [47]. However, although the effective elastic

properties of solid containing microcrack array with interaction between the microcracks has been considered [35-37,42,48], most of work about effective elastic properties are presented based on the small density microcracks configuration (see Fig. 3.5a). To our knowledge, the problem of effective elastic properties of elastic solid with high density microdefects (i.e., the distance between microcracks is much smaller than microcrack size, see Fig. 3.5b) was not presented before except a few special cases such as a periodic array microcracks.

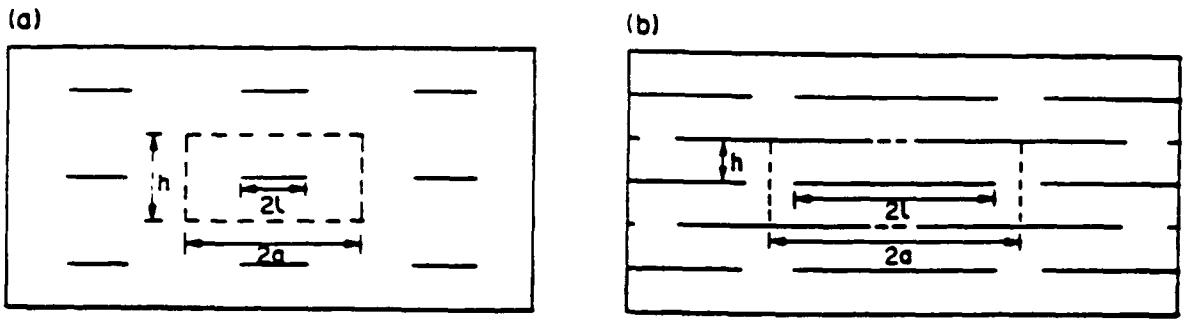

Figure 3.5 The sketch of a elastic solid with microdefects (microcrack or crazes).
(a). the case of small density microcracks.
(b). the case of high density microcracks.

For the problem of interaction between the microcracks, usually a microcrack array is modeled by detail description of the location, size and orientation of every microcrack [35-37,42,48]. Apparently detail description implies certain limitation on the number of the interaction cracks [49]. In order to solve the interaction problem of large number microcracks, a method based on the double layer potential technique [39], a self-consistency method [4,34] and a semi-empirical method [7,40] have been approached. For high density of microcrack (i.e., the distance between microcracks is much smaller than microcrack size), the problem of interaction between microcracks is so complex that the method emploied in the previous case becomes unrealistic. In this paper, in order to discuss the relation between the effective elastic properties and the failure criteria, a simple model is used to formulate the interaction problem. To evaluate the contribution of microcracks to the effective elastic properties, the element in Fig. 3.5b is represented by a simple beam for 2-D case and

by a thin plate for 3-D case. Two different boundary conditions, i.e., simply supported and build in edges, are used to obtain upper and lower bounds for the displacement jumps and consequently for the compliance. The compliance in the direction perpendicular to the cracks for both 2-D and 3-D cases are used as a example to test this model.

The relation between the effective elastic properties and the failure criteria have been discussed by this paper. Statistical analysis of the effective elastic properties show that the failure criteria appears to be sensitive to the distribution of size, orientation and distances between microcracks, where the effective elastic properties are quite insensitive to such morphological details.

Effective Elastic Properties of a Linear Elastic Solid with Microcracks

We consider a elastic solid with microcracks. The word "microcrack" is used to emphasize that the cracks size is small in comparison with a scale existing in the problem in question. The microcracks increase the compliance (decrease the stiffness) of the elastic body.

An average strain $<\varepsilon_{ij}>$ over a representative volume v for an elastic solid containing N microcracks is conventionally defined as:

$$<\varepsilon_{ij}> = <\varepsilon^0_{ij}> + \frac{1}{2V}\sum_{m=1}^{N}\int_{\omega^{(m)}} \{[u_i^{(m)}]\, n_j^{(m)} + [u_j^{(m)}]\, n_i^{(m)}\}\, d\omega \qquad (3.19)$$

where $<\varepsilon^0_{ij}>$ is the components of elastic strain in the bulk of the material, $u_i^{(m)}$ and $n_i^{(m)}$ are the components of the displacement jump across and the normal vector to m-th crack surface $\omega^{(m)}$, respectively.

The first term in Eq. (3.19) is simply related to the applied stress σ^{∞}_{ij} due to Hook's low:

$$<\varepsilon_{ij}> = C^0_{ijkl}\, <\sigma^{\infty}_{kl}> \qquad (3.20)$$

The second term in Eq. (3.19) can also be expressed in a similar fashion. Indeed, the contribution of the displacement jump due to m-th microcrack to the average deformation is

$$\frac{1}{2V}\int_{\omega^{(m)}} \{[u_i^{(m)}]\, n_j^{(m)} + [u_j^{(m)}]\, n_i^{(m)}\}\, d\omega = \Delta C_{ijkl}^{(m)} \langle \sigma_{kl}^{\infty} \rangle \qquad (3.21)$$

where the tensor ΔC_{ijkl} of compliance increment, in general, depends on the size, location, orientation and the openings of the microcracks surrounding the m-th crack. Thus the determination of ΔC_{ijkl} is based on the solution of a quite complex problem of many microcracks interaction. If this problem is solved, then the effective compliance tensor represents a resulting affect of individual microcrack contributions can be expressed as:

$$C_{ijkl} = C_{ijkl}^{0} + \sum_{m=1}^{N} \Delta C_{ijkl}^{(m)}. \qquad (3.22)$$

However, although many method have been approached for the interaction of microcrack array [35-37,39,42,48,49], there is no analytical solution for an arbitrary microcrack array configuration. Thus, the expression of Eq. (3.22) is useless except for a few particular cases. One of them has been well studied is a small density of microcracks (the interaction between microcracks is neglected). In the case of tension (for 3-D case, penny shape microcrack is considered) we have

$$\Delta C_{ijkl}^{(m)} = \begin{cases} \dfrac{(\ell^{(m)})^2}{V}\dfrac{\pi}{E} Q_{ijkl}^{(m)} & \text{for 2-D case} \\ \dfrac{(\ell^{(m)})^3}{V}\dfrac{(1-\nu^2)}{\pi(2-\nu)E}\,[n_j^{(m)} I_{ikl}^{(m)} + n_i^{(m)} I_{jkl}^{(m)}] & \text{for 3-D case} \end{cases} \qquad (3.23)$$

where

$$Q_{ijkl}^{(m)} = n_i^{(m)} n_l^{(m)} \delta_{jk} + n_j^{(m)} n_l^{(m)} \delta_{ik} \text{ and } I_{ijk}^{(m)} = \delta_{ij} n_k^{(m)} + \delta_{ik} n_j^{(m)} - \nu n_i^{(m)} n_j^{(m)} n_k^{(m)}, \qquad (3.24)$$

where E and ν. are Young's modulus and Poisson's ratio of material, respectively. Apparently, the symmetry of the effective elastic compliance tensor, Eq. (3.23), depends on the symmetry of statistical distribution of microcrack orientation as well as the symmetry of the initial elastic material.

The simplest result of Eq. (3.23) can be generalized accounting for microcrack interaction for particular microcrack array configurations [28].

For high density of micromechanics (i.e., the distance between microcracks is much smaller than microcrack size), the problem of interaction between microcracks is so complex that the method employed in the previous case becomes unrealistic. In the following we present a simple model which utilizes a small parameter, i.e., the ratio of the distance between parallel cracks and the size of the microcracks.

The representative volume for 2-D case is shown in Fig. 3.5b (in 3-D line cracks are replaced by penny-shape ones). High density microcracking implies a/h>>1. Traction free condition on microcrack surface is assumed. To evaluate the relation between the displacement jump $[u_i]$ and applied stress σ^∞, the element in Fig. 3.5b is represented by a simple beam for 2-D case and by a thin plate for 3-D case. Two different boundary conditions, i.e., simply supported and build in edges, are used to obtain upper and lower bounds for the displacement jumps and consequently for the compliance. The results of the calculation for the compliance in the direction perpendicular to the cracks can be expressed as follows. The details of the model are given in Appendix B.

For 2-D case (the microcrack is under the tension):

$$\Delta C^{(m)}_{2222} = \begin{Bmatrix} \dfrac{(\lambda^{(m)})^4}{E}\,\Phi_2^u(\eta^{(m)}) & \text{upper bound} \\ \dfrac{(\lambda^{(m)})^4}{E}\,\Phi_2^l(\eta^{(m)}) & \text{lower bound} \end{Bmatrix}. \tag{3.25}$$

For 3-D case (the microcrack is under the tension):

$$\Delta C^{(m)}_{3333} = \begin{Bmatrix} \dfrac{(\lambda^{(m)})^4}{E}\,\Phi_3^u(\eta^{(m)}) & \text{upper bound} \\ \dfrac{(\lambda^{(m)})^4}{E}\,\Phi_3^l(\eta^{(m)}) & \text{lower bound} \end{Bmatrix}. \tag{3.26}$$

where λ = a/h, η = ℓ/a. Functions $\Phi_2^u(\eta)$, $\Phi_2^l(\eta)$, $\Phi_3^u(\eta)$, and $\Phi_3^l(\eta)$ are given in Appendix B.

The dependence of functions $\Phi_2^u(\eta)$, $\Phi_2^l(\eta)$, $\Phi_3^u(\eta)$, and $\Phi_3^l(\eta)$ on the parameters λ. and η for 2-D and 3-D cases is given by Fig. 3.6. An energy release estimate shows that for $0.4 < \eta. < 0.7$ and $\lambda < 0.25$ the simple support

beam model (i.e. the upper limit) approximate well the high density microcrack effect including the interaction.

Effective Elastic Properties and Failure Criteria

As it was mentioned above, the changes in effective elastic response are often used to "measure" damage. Such measure can be misleading when used to formulate a failure criteria. Indeed, a failure criteria is usually related to an instability of the most "dangerous" crack where as effective elastic properties represent an average affect over all microcracks. For an illustrative purpose, below we use the well known Griffith's concept with the maximum energy release rate $G_I^{max} = 2\gamma$ as the failure criteria. This failure criteria appears to be sensitive to the distribution of size, orientation and distances between microcracks, where as the effective elastic properties are quite insensitive to such morphological details.

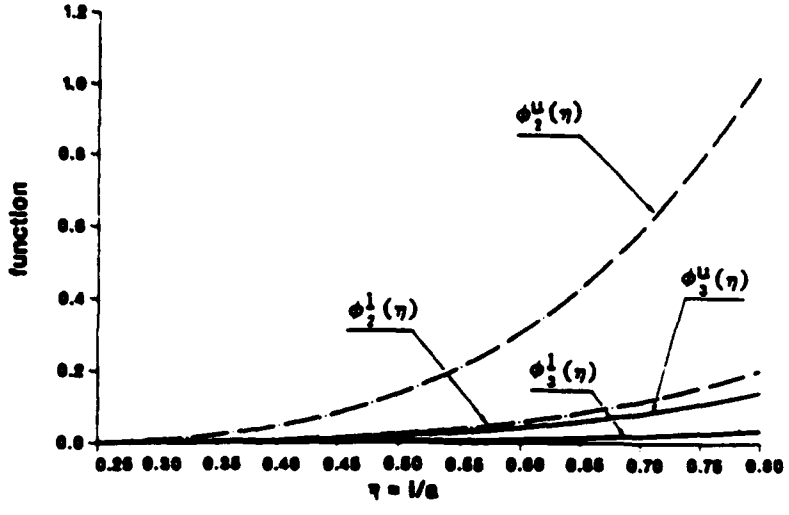

Figure 3.6 The dependence of functions $\Phi_2^u(\eta)$, $\Phi_2^l(\eta)$, $\Phi_3^u(\eta)$, and $\Phi_3^l(\eta)$ on the parameter ℓ/a.

Statistical Analysis of Effective Elastic Properties

A uniform distribution of microcrack location for both small density and high density is considered. For simplicity, we assume that microcracks are parallel (horizontal), and the microcrack length and distance between microcracks to be Gaussian random variables as:

$$f(l)=-\frac{1}{\sqrt{2\pi}\sigma_l}e^{-\frac{(l-\bar{l})^2}{2\sigma_l^2}} \qquad 0<l<l_{max} \tag{3.27}$$

$$f(x)=-\frac{1}{\sqrt{2\pi}\sigma_d}e^{-\frac{(x-\bar{x})^2}{2\sigma_d^2}} \qquad x_{min}<x<l \tag{3.28}$$

where $\sigma_l, \bar{l}, \sigma_d, \bar{x}$ are standard variance and mathematical expectation of microcrack length and distance between microcracks. Now using the same concept as [49] to consider the interaction between microcracks (see Fig. 3.5a). By comparing the stress intensity factor of one crack with collinear cracks under the same loading condition [50], a correction factor which reflect the interaction between collinear cracks can be obtained. The interaction between different layer cracks is ignored. Then the largest component of the effective elastic compliance may be expressed as:

$$C_{max}^{eff}=\langle C_{2222}^{eff}\rangle_v=\frac{1}{E}\left[1+\frac{1}{V}\sum_{m=1}^{N}2\pi(l^{(m)})^2\sqrt{\left|\frac{2}{\pi(1-x)}\tan\left(\frac{\pi(1-x)}{2}\right)\right|}\right] \tag{3.29}$$

where $x=(a-l)/a$ is the relative distance between cracks. In this case the largest component of the effective elastic compliance is C_{2222}^{eff}. For small density of microcracks, a simple statistical analysis shows that the normalized standard deviation of the maximum effective compliance is proportional to $N^{-1/2}$ (N is the number of microcracks in a representative volume):

$$\frac{\sigma(C_{max}^{eff})}{\langle C_{max}^{eff}\rangle}=k\left(\frac{\sigma_l\sigma_d}{N}\right)^{1/2} \tag{3.30}$$

where σ_ℓ and σ_d are the standard deviation of microcrack size and distances, respectively. $k \approx 2$ for $\lambda = 1$, $\bar{\ell} = 0.4$ and average distance between cracks $\bar{x} = 0.5\,a$. Thus, when the representative volume is large enough, i.e., contains a large number N of microcracks, the scatter of the effective elastic properties become negligible.

Using the same procedure as above and considering the Eqs. (3.25) and (3.26), the same result is obtained for high density of microcracks, except the coefficient of proportionality k is about 10 times larger than that of small density. Thus the relative scatter of effective elastic properties decrease with number of microcracks much slower than for small density case.

Statistical Analysis of Strength

Now we consider the scatter of G_I^{max} employed in Griffith's criterion of failure for the most dangerous microcrack. The largest energy release rate results from the most unfavorable combination of two random variables: crack length and the distance between the cracks.

The distributions of the largest crack length and the smallest distance between the microcracks result from conventional in statistics of extremes derivation [51]:

$$F_{max}(\ell) = \begin{cases} 0 & \text{if } \ell < \ell_{min} \\ e^{-\beta\left(\frac{\ell_{max} - \ell}{\ell - \ell_{min}}\right)^{\alpha}} & \text{if } \ell_{min} < \ell < \ell_{max} \\ 1 & \text{if } \ell > \ell_{max} \end{cases} \tag{3.31}$$

$$F_{min}(x) = \begin{cases} 0 & \text{if } x < x_{min} \\ 1 - e^{-\beta\left(\frac{x_{max} - x}{x - x_{min}}\right)^{\alpha}} & \text{if } x_{min} < x < x_{max} \\ 1 & \text{if } x > x_{max} \end{cases} \tag{3.32}$$

where α, β are phenomenological parameters.

Evaluation of the normalized standard deviation $\sigma(G_I^{max})/\langle G_I^{max}\rangle$ for 2-D problem shows for $\alpha < 3$ and $\beta = 1$

$$20\% < \frac{\sigma(G_I^{max})}{\langle G_I^{max}\rangle} < 100\% \qquad \text{for small density} \tag{3.33}$$

and

$$15\% < \frac{\sigma(G_I^{max})}{\langle G_I^{max}\rangle} < 80\% \qquad \text{for high density (simple support beam model)} \tag{3.34}$$

Thus one can expect a large scatter in strength measurements and relatively low scatter in effective elastic properties. It suggest that the later are not a good measure of damage.

Similar conclusion is formulated by [47] based on their numerical simulation of five realization of a random array containing 48 cracks. The results shows that the Young's modulus E_{eff}/E_0 varied from 0.66 to 0.73 whereas $\sigma(G_I^{max})/\langle G_I^{max}\rangle$ varied from 0.94 to 1.93.

Conclusion and Discussion

The effective elastic properties of an elastic solid with small and high density microcracks are discussed. For high density of micromechanics, the problem of interaction between microcracks is represented by a simple beam for 2-D case and by a thin plate for 3-D case. Two different boundary conditions, i.e., simply supported and build in edges, are used to obtain upper and lower bounds for the displacement jumps and consequently for the compliance.

The effective elastic properties of solid with microdefects is an important way to analyze the volume average physical parameters of materials. The effective elastic properties are volume average quantities, then it is not sensitive to the distribution of shape and size of microdefects. However, failure of an elastic solid is strongly depend on the detail of microdefects, the size, orientation and distances between microcracks, the effective elastic properties is not adequate to be used as a "measure" of damage, and should be used with caution in the failure analysis.

CHAPTER 4

THERMODYNAMICS OF THE PROCESS ZONE

4.1 Thermodynamic Model of the Process Zone

Introduction

Propagation of a fatigue crack by first forming a process zone ahead of the crack and then forcing its way through the zone is a well-known phenomena. The Dugdale-Barenblatt Model, (DBM), is conventionally employed to analyze the process zone [15,52]. The application of the DBM for various polyethylenes seems plausible since the basic features of the model are observed, for example, the process zone has a thin strip shape [53,54] and has constancy of stress along the process zone [55]. In this paper we examine the differences between the size of the process zone formed under fatigue and the DBM prediction. The process zone size is evaluated based on fatigue striations observed on the fracture surface. Recently Chudnovsky proposed a new model for the process zone [10,11], which renders the simplicity of the DBM and the same time releases some of its limitations. In this chapter the new model, CM, is employed to analyze the process zone preceding fatigue crack growth in various polyethylenes reported [56] and polycarbonate.

Description of the Model

The process zone in front of a crack is considered to be a zone of allotropically transformed material. Indeed, in polyethylene or polycarbonate analyzed below, the drawn material of the process zone can be regarded as a second phase since it differs from the original one by its physical properties, and is separated by a distinct boundary. A typical process zone formed in front of a fatigue crack is illustrated in Fig. 4.1a.

Let G be the Gibbs potential of the two phase system shown in Fig. 4.1b and V_{tr} be the domain occupied by the second phase (process zone). For isothermal condition and fixed remote load, an equilibrial process zone, V_{tr} , renders the minimum of G:

$$\frac{\delta G[\sigma_\infty, l\ , V_{tr}]}{\delta V_{tr}}\Big|_{\sigma_\infty=\text{const.},l=\text{const.}} = 0 \qquad (4.1)$$

The brackets indicate that G is a functional of the zone V_{tr} and a function of the crack length, l, and the applied stress, σ_∞ .

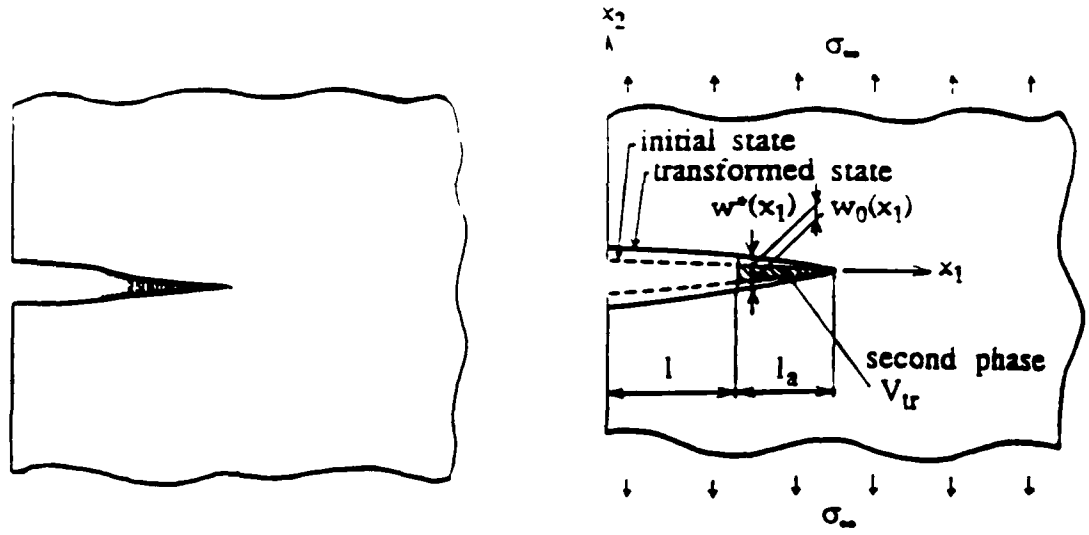

a) Schematic illustration of the process zone.

(a)

b) Schematic illustration of the model.

(b)

Figure 4.1 (a) Schematic illustration of the process zone.
(b) Schematic illustration of the model.

Following Eshelby [43], the change in Gibbs potential of the system as a result of the migration of the boundary ∂V_{tr} between two phases can be expressed as:

$$\delta G = - \int_{\partial V_{tr}} \delta\xi_i \, (P_{ij}^{0} - P_{ij}^{tr}) \, n_j \, d\Gamma \qquad (4.2)$$

where P_{ij} is the energy momentum tensor of elasticity (Eshelby tensor) $P_{ij}=f\delta_{ij}-\sigma^*_{jk}u_{k,i}$, f is the Helmholtz free energy density, σ^*_{jk} and $u_{k,i}$ stand for Piola-Kirchhoff stress tensor and the gradient of the displacement vector u_k, respectively; $\delta\xi_i$ is an infinitesimal vector of boundary migration ∂V_{tr} and n_j is the unit normal vector directed outwards from the transformed toward initial material. Superscripts "0" and "tr" refer to the original and the second (transformed) phase, respectively.

The continuity of the traction and the displacement vectors at the phase boundary ∂V_{tr}, the equilibrium and compatibility equations within each phase together with equation (4.34) result in a system of integro-differential equations for determining equilibrial V_{tr}. To our knowledge there is no

analytical solution to the problem in such generality. To simplify the problem the following assumptions are admitted:

a) The process zone width w is much smaller than its length l_a: $w/l_a<<1$, i.e., V_{tr} has a shape of a thin strip.

b) The process zone consists of a cold drawn material with a constant draw ratio, λ.

The two phase system equilibrium, (Fig. 4.1b), is represented as a superposition of the two problems, illustrated in Fig. 4.2. The first results from the original problem after removing the process zone and substituting it with an equivalent traction σ_{tr}. The second is the process zone V_{tr} submitted to σ_{tr} representing the action of the original phase onto the transformed one. The constancy of σ_{tr} along the phase boundary follows from the phase equilibrium condition.

The width, w_0, of the layer of the original material which undergoes the transformation varies along the process zone and is unknown. The width, w^*, of the transformed layer is $w^*= \lambda w_0$. The displacement continuity, i.e., the coherency of the phase boundary can be expressed as follows:

$$w^*(x_1) - w_0(x_1) = \Delta(x_1,l_a) \tag{4.3}$$

where $\Delta(x_1,l_a)$ stands for the slit opening displacement (Fig. 4.2a) and x_1 is the coordinate shown in Fig. 4.11b. Then the width $w_0(x_1)$ of the initial strip which undergoes the transformation is related to the slit opening displacement and the draw ratio:

$$w_0(x_1)=\Delta(x_1,l_a)/(\lambda-1) \tag{4.4}$$

The volume V_{tr} of the initial material which undergoes the transformation can be expressed as:

$$V_{tr} = \frac{t_0}{\lambda - 1} \int_{l}^{l+l_a} \Delta\,(l,l_a;\sigma_\infty,\sigma_{tr};x_1)\, dx_1 \tag{4.5}$$

where t_0 is the initial thickness of the specimen. Given the assumptions a) and b) it can be shown that the variation of V_{tr} is uniquely determined by changes in l_a. Thus, equation (4.1) can be rewritten as:

$$\frac{dG\,(\,\sigma_\infty,\,l\,,\,l_a\,)}{dl_a}\Big|_{\sigma_\infty=\text{const.},l=\text{const.}} = 0 \qquad (4.6)$$

Since the slit is narrow we approximate $\Delta(x_1, l_a)$ by the crack opening displacement (COD) and employing a standard fracture mechanics formalism, equation (4.39) leads to the following equation for l_a [11]:

$$K^{tot}(\sigma_\infty, \sigma_{tr}; l, l_a)\,|_{\sigma_\infty=\text{const.},l=\text{const.}} = -\frac{2\gamma^{tr}}{(\lambda - 1)\,\sigma_{tr}}\,K(\sigma_{tr}; l, l_a)\,|_{l=\text{const.}} \qquad (4.7)$$

Here K^{tot} is the stress intensity factor (SIF) for the problem of Fig. 4.2a, $K(\sigma_{tr};l,l_a)$ is the SIF for the same problem with absence of σ_∞. A new parameter γ^{tr} ($\equiv P^0_{22} - P^{tr}_{22}$) represents the jump of the Gibbs potential density (per unit volume) over the boundary between the drawn and original material (see next section).

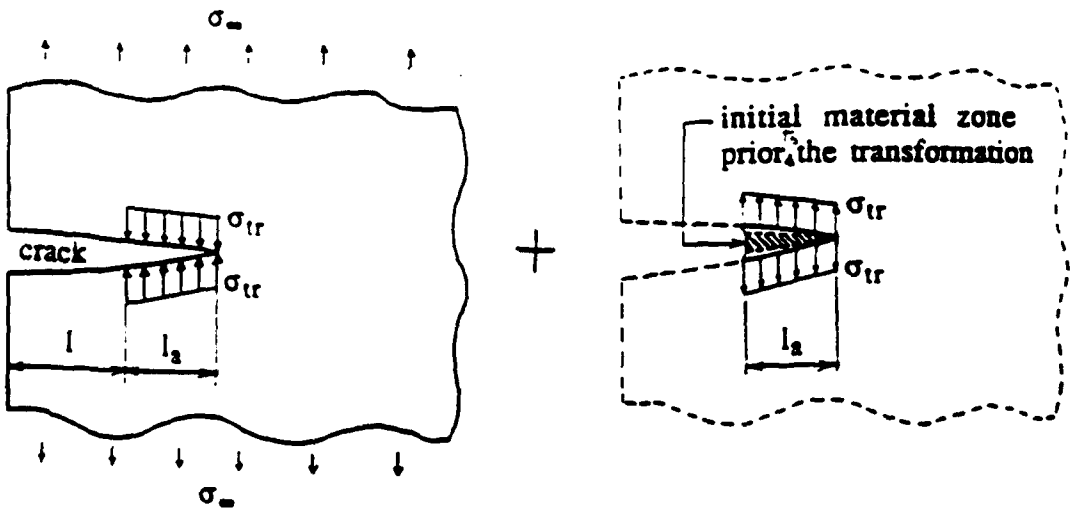

Figure 4.2 Crack carrying the transformation stress σ_{tr} at its edge (a) and the process zone of the transformed material (b).

The three material parameters, γ^{tr}, λ and σ_{tr} are employed in the model. It should be emphasized that these parameters can be determined in independent tests, for example, in a tensile test on neck formation, including the heat flux measurements together with calorimetry for determination of the residual strain energy in the necked region. The evaluation of γ^{tr}, λ and σ_{tr} for three PE's are presented in the next section.

Figure 4.3 displays the comparison of the DBM prediction and that of our model for SEN specimen for various $\tilde{\gamma}=\gamma^{tr}/(\lambda-1)\sigma_{tr}$ ($\sigma_\infty/\sigma_{tr}$ =0.23, l/B=0.4), where B is a specimen width. The vertical axis is normalized with respect to the SIF K_0 of the same crack in absence of the process zone. $K^{tot}=0$ gives the DBM process zone length "b" and a point of intersection of two curves (K^{tot} and $-2\tilde{\gamma}\,K(\sigma_{tr})$) is the equilibrial process zone length of our model. The equilibrial process zone length decreases significantly with $\tilde{\gamma}$. For $\tilde{\gamma}\approx 1$, the two models predictions differ by an order of magnitude. It is easy to see from equation (4.7) that in the limit $\gamma^{tr}/\sigma_{tr}(\lambda-1)\rightarrow 0$, the model reduces to the well-known equation of the DBM, i.e., $K^{tot}=0$.

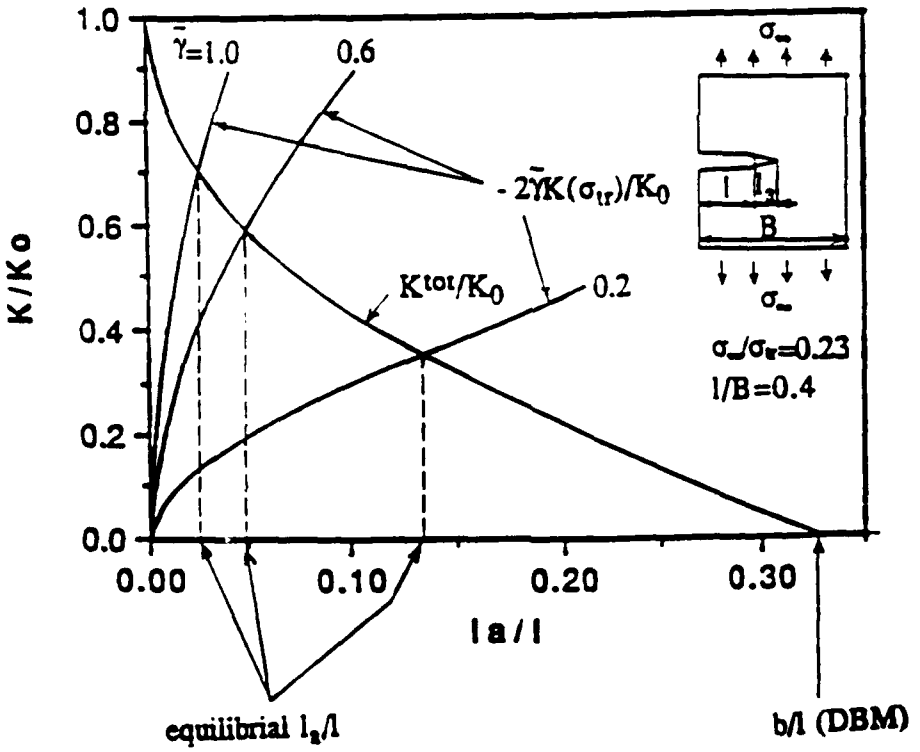

Figure 4.3 Graphic solution of equation (4.40) for various $\tilde{\gamma}=\gamma^{tr}/(\lambda-1)\sigma_{tr}$ (K_0 is the SIF of the same crack length in absence of the process zone).

Evaluation of Material Properties

The factor $\tilde{\gamma}$ has been measured in a simple tension test [10]. Typical tensile stress-strain curves of initial and drawn PE together with the photograph of a specimen illustrating the growth of a stable neck are shown in Fig. 4.4. The materials properties relevant to the analysis are summarized in Table 4.1 The necked material in the tensile test appears as a homogeneously drawn continuum. In contrast the material within the process zone is highly fibrillated (cavitated) due to the constraint of the plane strain condition. The cavitation and fibrillation are well manifested on the fracture surface and apparently play an important role in the fracture process. For instance, the evolution of micro features on fracture surfaces indirectly related to the crack driving force [9,57]. Thus, the value of $\tilde{\gamma}$ obtained in the tensile test with neck formation is simply an approximation of $\tilde{\gamma}$ in a process zone formation.

Result and Discussion

a) Shape of the process zone

From equations (4.3) and (4.4), the width of the transformed layer $w^*(x_1)$ can be expressed through the slit opening Δ as $w^*(x_1)=\lambda/(\lambda-1)\ \Delta(x_1,l,l_a)$. Thus, the shape of the process zone can be uniquely determined by the model for given l and l_a. Fig. 4.5a shows the envelope of the set of process zones calculated from the initial crack length to the current crack length. A typical process zone formed in front of a fatigue crack in Polycarbonate (PC) is illustrated in Fig. 4.5b. An effective draw ratio $\lambda^{eff}=1.33$ was used to account heterogeneous drawing within the process zone [14]. The model prediction shows a very good agreement with that observed experimentally.

b) Size of the process zone

Fig.4.6, 4.7 and 4.8 represent the SEM micrographs of the fatigue fracture surfaces of M5202, TR140 and TR418 polyethylenes (specimens courtesy Dr. N. Brown). The SEN specimens are 25mm wide and 10mm thick with 3.5mm deep notch. A 1Hz sinusoidal load is applied with the maximum and minimum stress ±4MPa, respectively.

Fatigue striations are observed on the fracture surface [9]. Based on the discontinuous fatigue crack growth mechanism reported elsewhere [56,58] as well as our own observations, we consider the bands between consecutive striations on the fracture surface to be a measure of the corresponding process zone length. The band-width increases with the crack length for every PE studied. The various PE's are distinguished by their branch density [56]. We note that the band-width increases with increase in branch density for any given crack length.

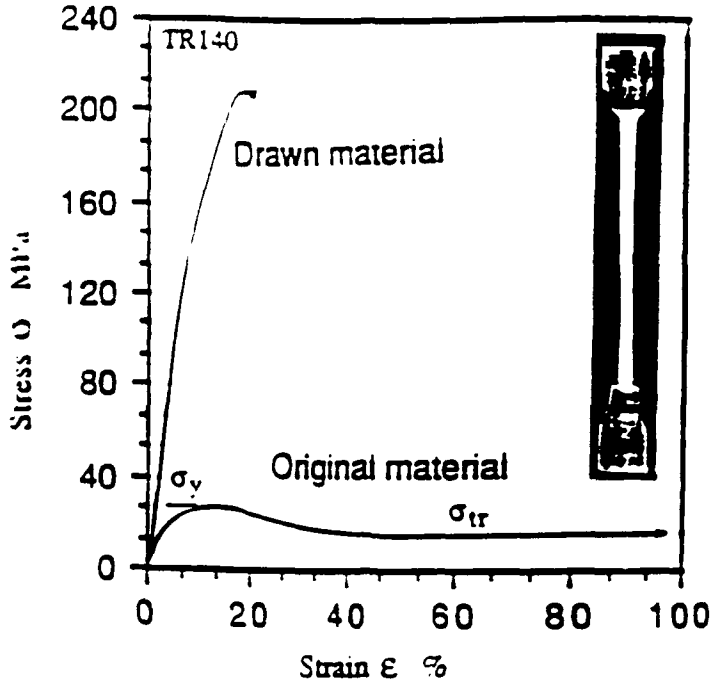

Figure 4.4 The stress-strain curves of original and drawn material.

TABLE 4.1
MATERIAL PROPERTIES OF M5202, TR140 AND TR418 RESINS

Resin	M5202	TR140	TR418
Branch Density *1 (butyl/1000c)	1.2	2.3	4.6
Young's modulus (initial PE) (GPa)	1.12	0.77	0.50
Young's modulus (drawn PE) (GPa)	2.73	2.00	1.50
σ_y (MPa)	30.5	27.0	22.5
σ_{tr} (MPa)	17.5	15.8	14.2
Draw Ratio λ	6.5	5.5	5.1
Energy of material transformation γ_{tr} (MJ/m^3)	101.0	74.7	61.1
$\tilde{\gamma}=\gamma_{tr}/(\lambda - 1)\sigma_{tr}$	1.05	1.05	1.05

(Specimens and data *1, courtesy of Dr. N. Brown)
(σ_y=maximum load/cross sectional area of the initial state)

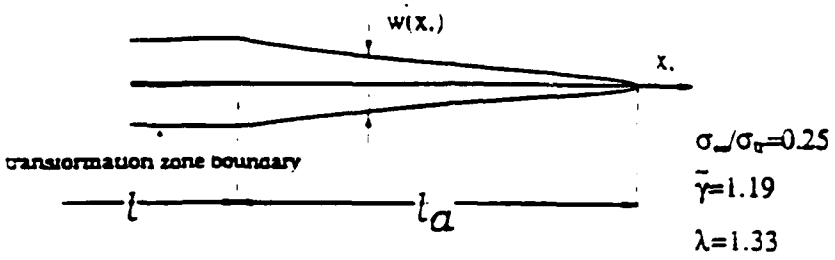

a) the envelope of the process zone (The model prediction).

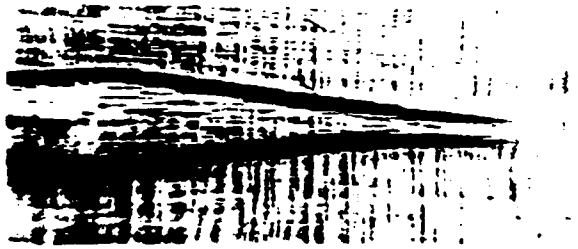

b) Composite optical micrograph of a side view of the crack with the process zone in Polycarbonate.

Figure 4.5 The shape of the process zone.

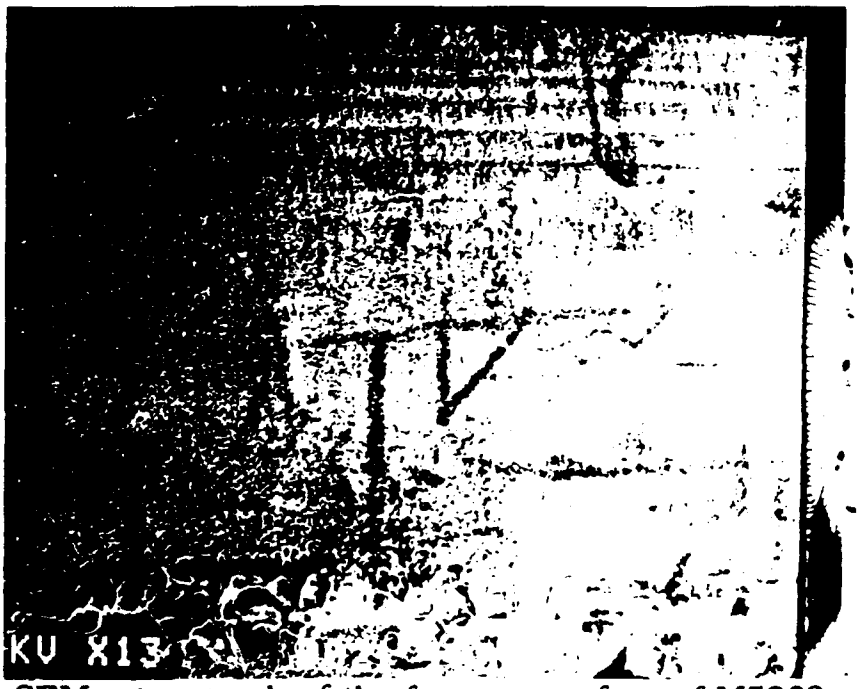

Figure 4.6 SEM micrograph of the fracture surface of M5202 (Branch Density=1.2)

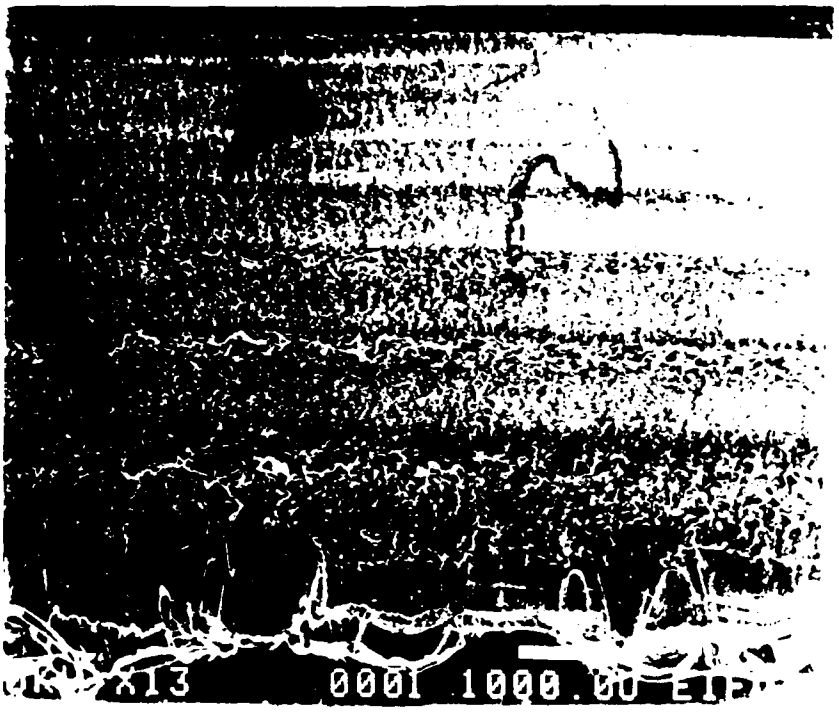

Figure 4.7 SEM micrograph of the fracture surface of TR140 (Branch Density=2.3)

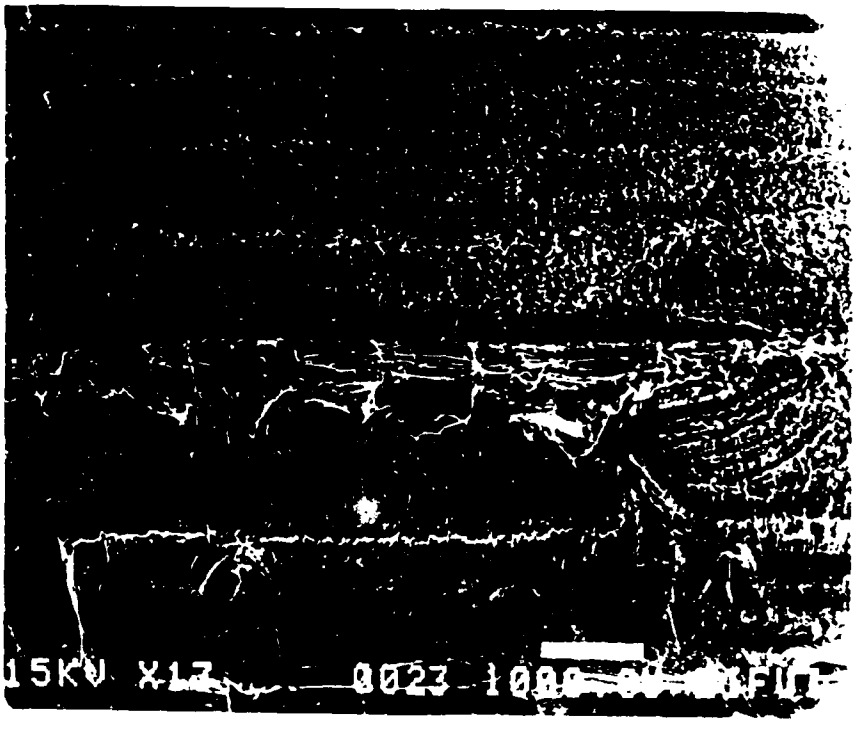

Figure 4.8 SEM micrograph of the fracture surface of TR418 (Branch Density=4.6)

Our purpose is to compare the theoretical prediction of the process zone length, l_a, i.e., the solution of equation (4.7) for various l. with the observed band-width. The conventional fracture mechanics formalism is employed to evaluate the SIF of equation (4.7).

The results of an application of the Chudnovsky Model to the three polyethylenes (M5202, TR140 and TR418) are shown in Figs. 4.9, 4.10 and 4.11, respectively. The "points" represent the band-width observed on the fracture surfaces. The solid lines show the solution of equation (4.7) in terms of l_a vs. l. The dashed lines represent the DBM prediction for comparison. The CM gives much better predictions than the DBM. The predictions are expected to be much better if we account for the cavitation and fibrillation processes and the heat flux. We have observed the exothermic heat flux qualitatively with IR microscope, but no measurements have been performed yet. Accounting for heat loss leads to a reduction in the reported value of γ^{tr} and consequently to an increase in the predicted process zone size (see Fig. 4.3).

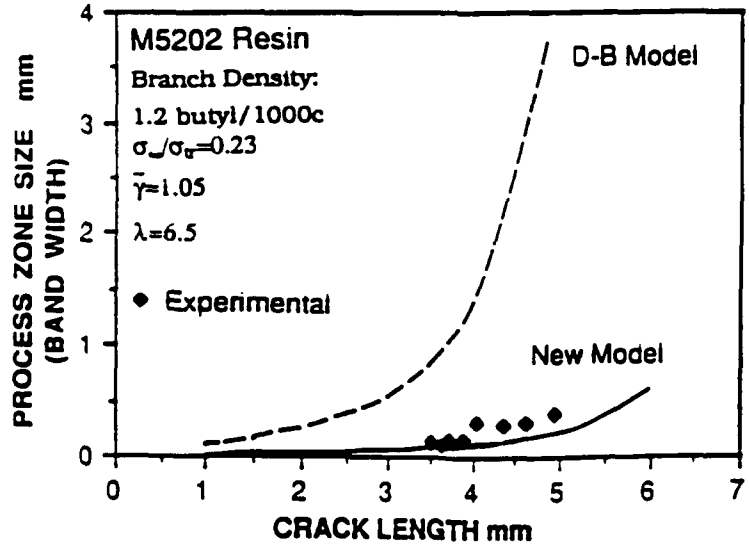

Figure 4.9 Process zone size vs. Crack length (M5202).

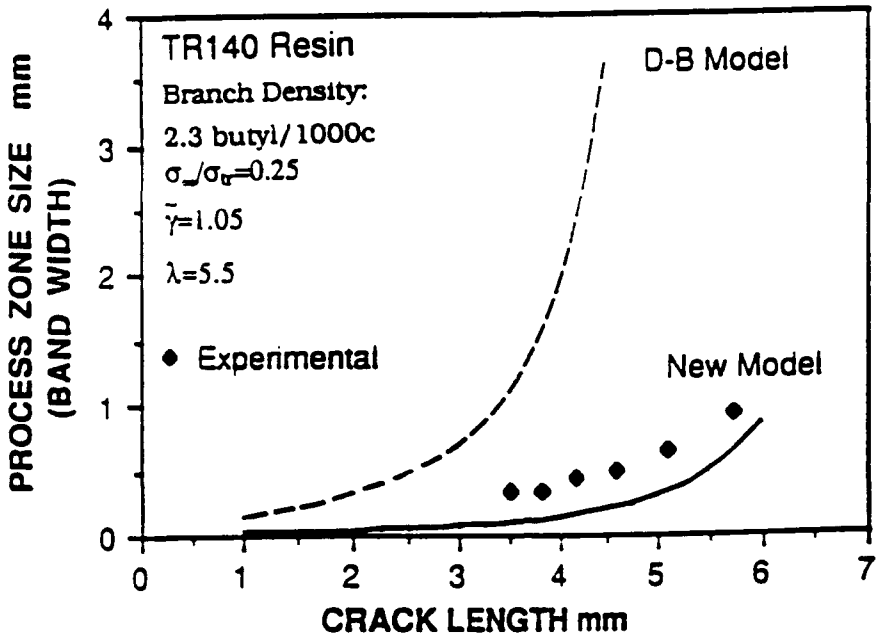

Figure 4.10 Process zone size vs. Crack length (TR140)

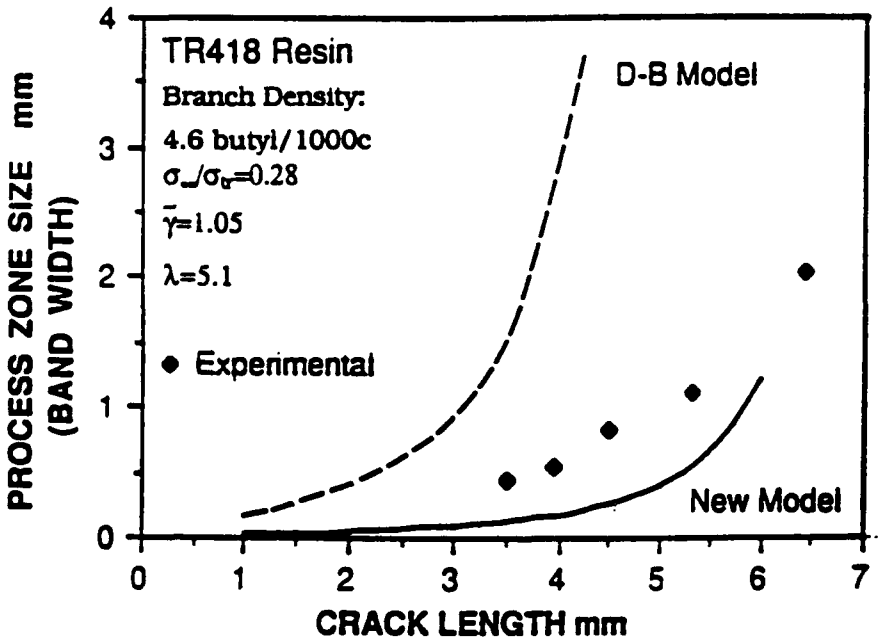

Figure 4.11 Process zone size vs. Crack length (TR418)

4.2 A New Measure of Toughness

The slow process of the crack propagation in the SEN specimen is known to end abruptly with instability of the process zone (Kasakevich et al. [86,87]). The ductile instability characterization of medium density PE has been studied with J integral R-curve method by Narisawa and Nishimura [88]. However the tedious and expensive testing procedure preparing many identical specimens calls for the necessity of a simple test to determine the instability point. It is also pointed out by Strebel and Moet [89] that the standard J_{1c} test often requires unrealistic thick specimen and the value obtained from such experiment may not represent the fracture toughness of the actual structural element, since the morphological difference can be expected because of the different thickness.

The instability condition of the process zone results from the general thermodynamic consideration as the vanishing of the second derivative of the Gibbs potential with respect to l_a, i.e., $\partial^2 G / \partial l_a{}^2 = 0$. It yields the critical values for the crack length l^* and the process zone length $l_a{}^*$ at the point of instability for given applied stress σ_∞. The detail description of the stability analysis of the CL is discussed in chapter 6.

The resistance, R, for crack propagation can be measured by the rate of the total energy absorbed on the process zone formation. It is expressed as the product of the specific energy of the material transformation γ_{tr} and the change of the volume of the zone with respect to the crack length $\partial V_{tr} / \partial l$. In the SEN specimen, the change of the volume $\partial V_{tr} / \partial l$ monotonically increases with crack length leading to a monotonic increase of the resistance R in agreement with the R-curve concept (Fig. 4.12). At the point of instability, R reaches the maximum value R^*. Thus the maximum energy absorption rate R^* prior to instability is proposed as a measure of material toughness. The values of R^* (per unit thickness) for three PEs are presented in TABLE III. The proposed measure of toughness correlates well with the lifetime under fatigue as well as creep condition. It is illustrated in Fig. 4.13 which shows the fatigue and creep lifetimes (in min, in log. scale) reported in the paper by Zhou et al.[56] versus R^*.

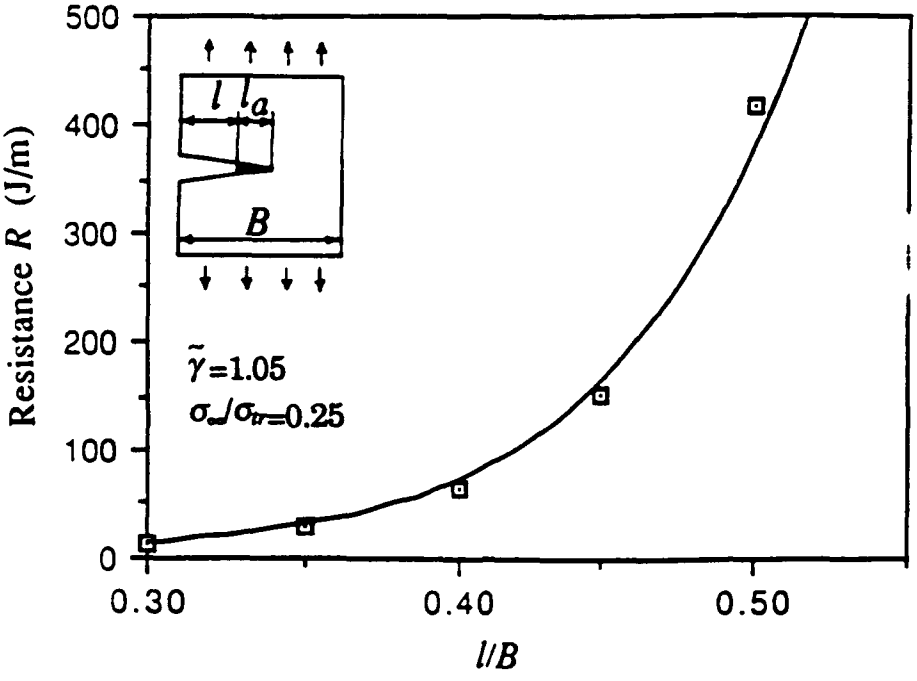

Figure 4.12 Resistance R versus crack length.

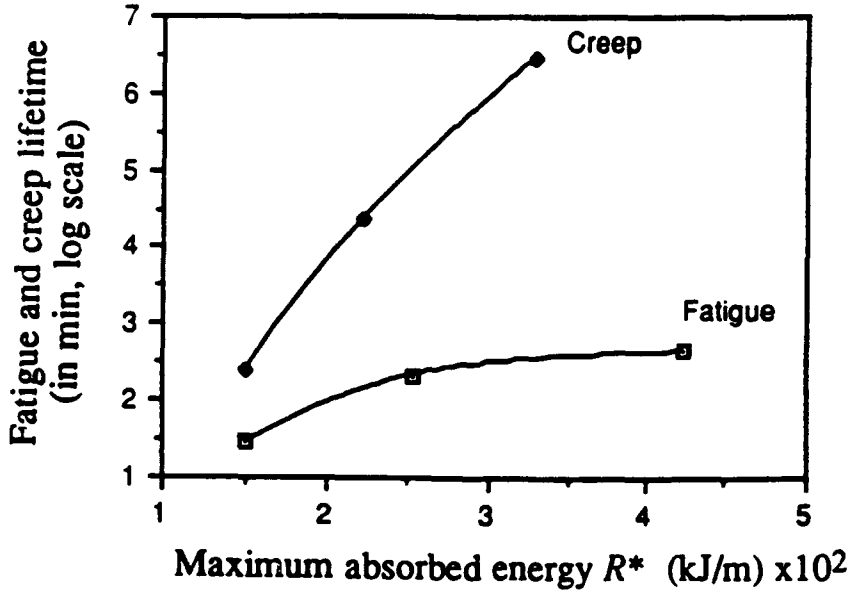

Figure 4.13 Maximum absorbed energy versus fatigue and creep lifetimes.

However no kinetics are involved in the evaluation of this measure. Thus, it should be emphasized that this measure can be utilized only as a tool to choose or rank materials as a first step when one would like to screen out materials for design purpose. The lifetime estimates require further study of the CL propagation law and are discussed in the next chapter.

Conclusion

A new thermodynamic model proposed by Chudnovsky has been successfully applied for the analysis of the process zone in SEN polyethylene specimen. Three material parameters employed in the model are determined in an independent test. Thus, no adjustable parameters are required. The maximum energy absorption on the process zone formation is proposed as a measure of toughness. The measure can be used as a convenient tool and as a first step in screening out materials for design purpose.

TABLE 4.2

VALUES OF MAXIMUM ENERGY ABSORPTION R^* (kJ/m) x10^2

resin / Loading condition	M5202	TR140	TR418
Fatigue σ_{max}=4(MPa)	1.5	2.5	4.2
Creep σ_{∞}=3(MPa)	1.5	2.2	3.3

CHAPTER 5

KINETIC EQUATION FOR PROCESS ZONE GROWTH

5.1 Kinetic Equation for Process Zone Growth in Polycarbonate

Introduction

Numerous authors have reported that slow-crack propagation in polycarbonate (PC) is commensurate with the formation and growth of a process zone surrounding the crack [11,59-61]. The energy required for process zone growth can be many orders of magnitude greater than the surface energy associated with crack formation and as such can provide significant resistance to crack growth. Thus the kinetics of the process zone development is an essential factor in the PC lifetime determination. However, the kinetics of the process zone evolution is closely coupled with that of the crack growth which complicates the determination of the kinetics of the process zone evolution itself.

The purpose of this study is to develop a methodology for the determination of the kinetics of the process zone evolution by decoupling these two processes. This is achieved by observing the process zone growth under stress-relaxation at essentially constant crack length. The growth of process zone under stress-relaxation was previously reported for polystyrene [62]. Also presented is a comparative analysis of the mechanism of process zone formation ahead of the crack with necking phenomena under simple tensile drawing. In a subsequent paper we will report the derivation of new constitutive equations for PC process zone evolution which allow the generation of a master curve for our observations reported here.

Experimental Setup and Observations

a) Material and Specimen Preparation

Polycarbonate of molecular weight, Mw 38000, Calibre 300-3, was provided by the Dow Chemical Company in the form of injection molded plaques of 3 mm thickness. After drying in a vacuum oven at 120°C for 24 hours, the plaques were further compressed to 0.7 mm thickness using a Dake compression molder under the following conditions; preheat to 270°C, hold at zero load for 10 minutes, compression under 4 MN/m^2 for 5 minutes, then another 8 minutes under this same compression condition until cooled to 23°C. Single edge notched(SEN) specimen of dimensions shown in Fig. 5.1a and dumbbell specimens, Fig. 5.1b were machined from

the compression molded plaques. The notch tips of SEN specimens were carefully introduced by razor blades. Smaller dumbbell specimens shown in Fig. 5.1c, were machined from the necked portion of pulled specimens Shown in Fig. 5.1b.

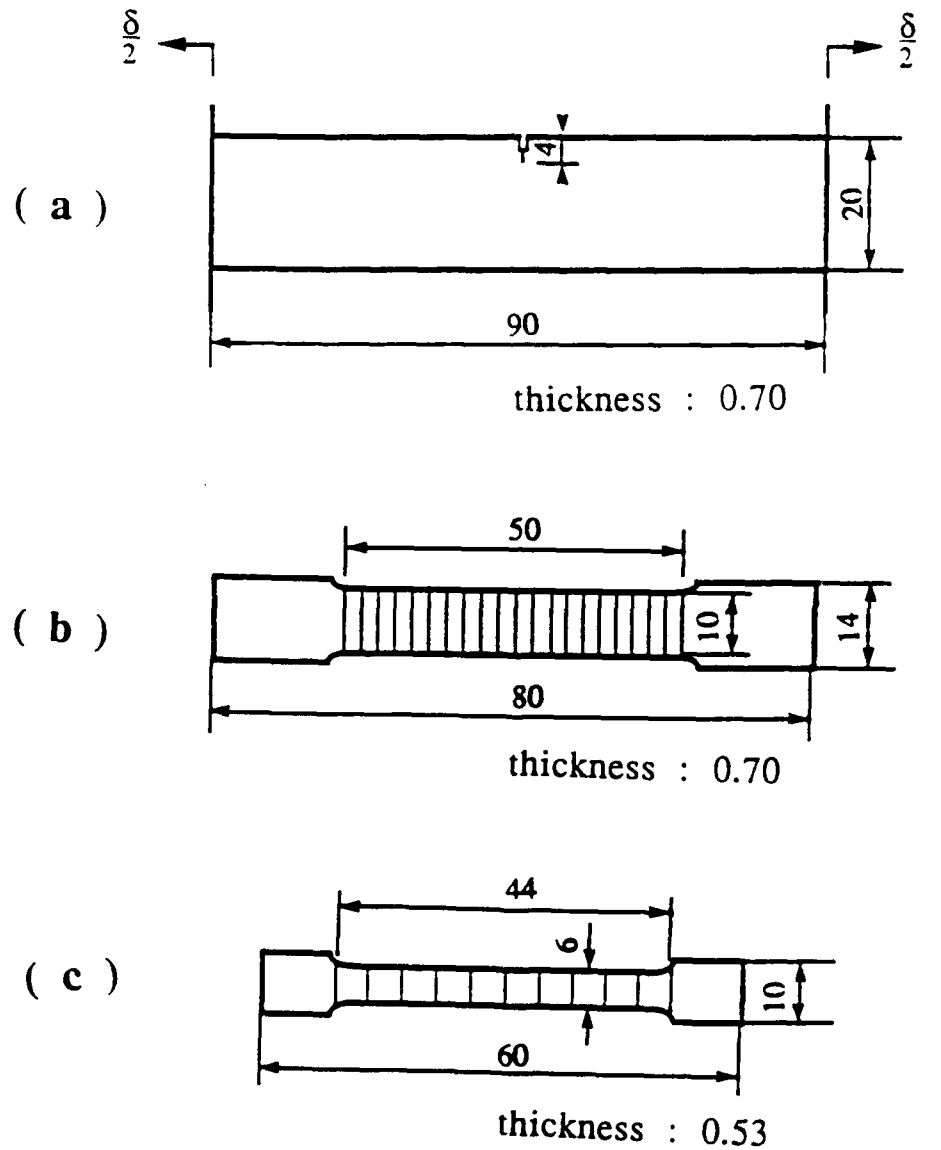

Figure 5.1 a) Dimensions of SEN, b) Dumbell specimen for original material, c) Dumbell specimen for drawn material

b) Tensile Test

The dummbell specimens were marked with horizontal lines (Fig. 5.1b) and pulled at an initial crosshead speed of 0.6 mm/min at 23±1°C. The draw ratio, λ, was determined from the ratio of the spacing between the marked lines of the drawn (necked) material, Fig. 5.1c, to that of the untransformed material. To characterize the properties of the drawn polycarbonate, smaller tensile bars with dimensions as shown in Fig. 5.1c were cut from the necked region and repulled as above.

c) Kinetics of Process Zone Growth under Fixed Displacement.

The SEN specimens were strained in tension to fixed displacements, 1.00, 1.15, 1.25 and 1.35 mm, at a constant cross-head speed of 0.6 mm/sec at 23±1°C, then held at constant strain. The load was monitored throughout the test. The kinetics of the process zone evolution was monitored through a video-recording system attached to a microscope. The process zone size is reconstructed from a combination of a side view from the video screen and optical microscopy of two cross-sections perpendicular and parallel to the direction of load application (Fig. 5.2).

d) Evaluation of Apparent Shear Band Density

The density of shear bands in the process zone was measured by optical microscopy. A micrograph of a cross-section perpendicular to the direction of load application was prepared for the evaluation(Fig. 5.2b). The shear bands in the micrograph appear to be dark stripes. The micrograph is subdivided into elementary squares, 0.077mm x 0.077mm, and the apparent density of shear bands evaluated as a ratio of the dark stripes inside a unit square to the area of this unit square.

e) Thinning in the Process Zone

The thinning in the process zone relative to an undeformed region was measured in four specimens using a Zeiss optical microscope with x200 magnification to an accuracy on the micrometer scale. The thinning was measured at more than 15 sites in each equilibrial process zone to construct the equal thinning level contour. The thinning is measured as $(z_o-z)/z_o$ where z is the specimen thickness and z_o is the undeformed thickness.

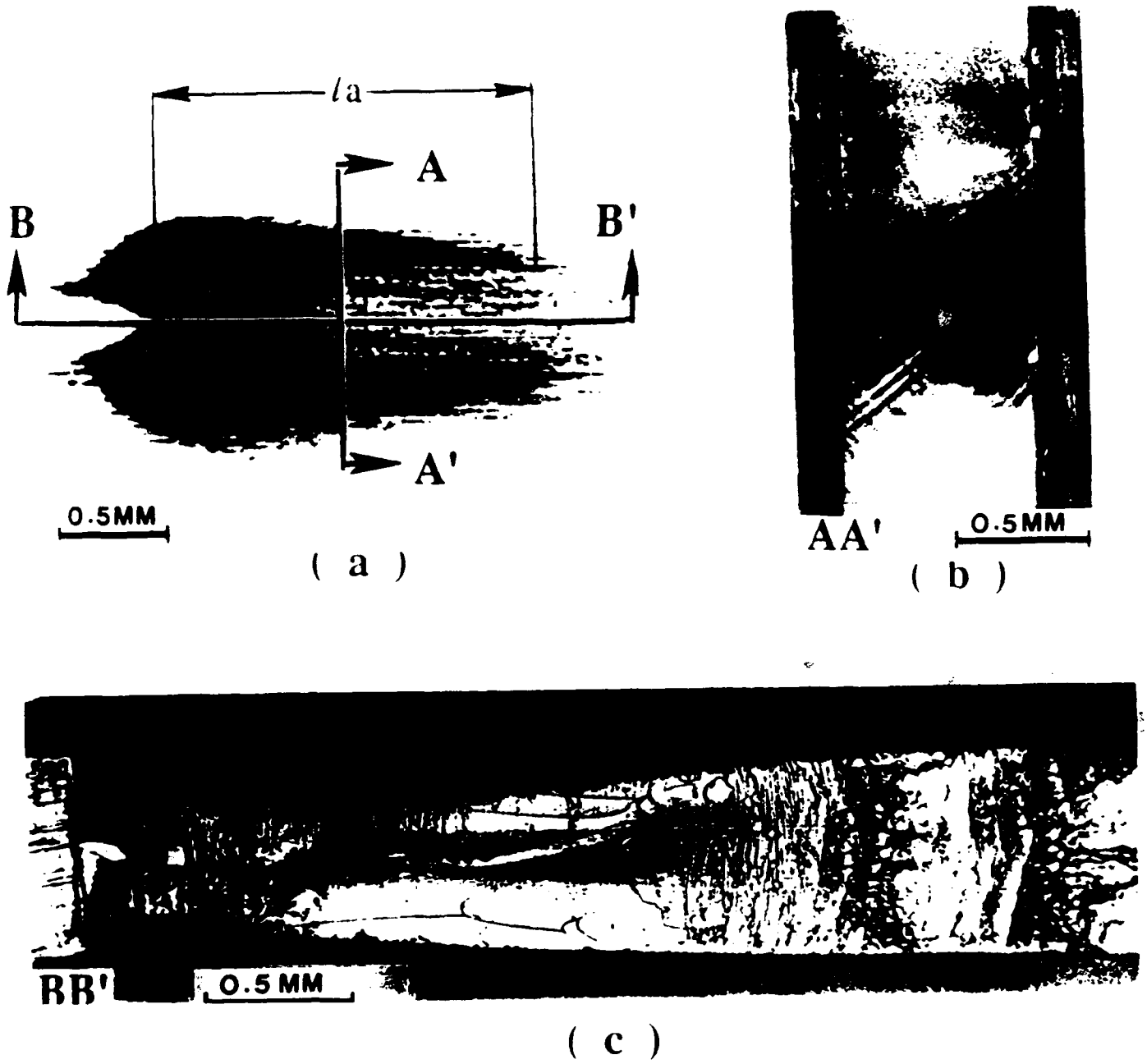

Figure 5.2 a) A side-view of process zone from the video screen
b) Cross-section A-A' in polarized transmitted light
c) Fracture surface of cross-section B-B' fractured in liquid nitrogen

Results and Discussion

Figs. 5.2a, b and c are examples of an actual determination of the process zone shape and size from the side view, cross-sections A-A' (normal to the crack plane) and B-B' (surface after fracture in liquid nitrogen). These three projections allow the determination of the process zone dimensions. It is obvious from Fig. 5.2b (cross-section A-A') that there is thinning in the thickness direction. In addition, two families of intersecting shear bands are observed. Fig. 5.3 is a schematic of the three dimensional process zone consisting of intersecting shear bands with varying density. Similar features have been well-described previously [63]. This point will be readdressed later.

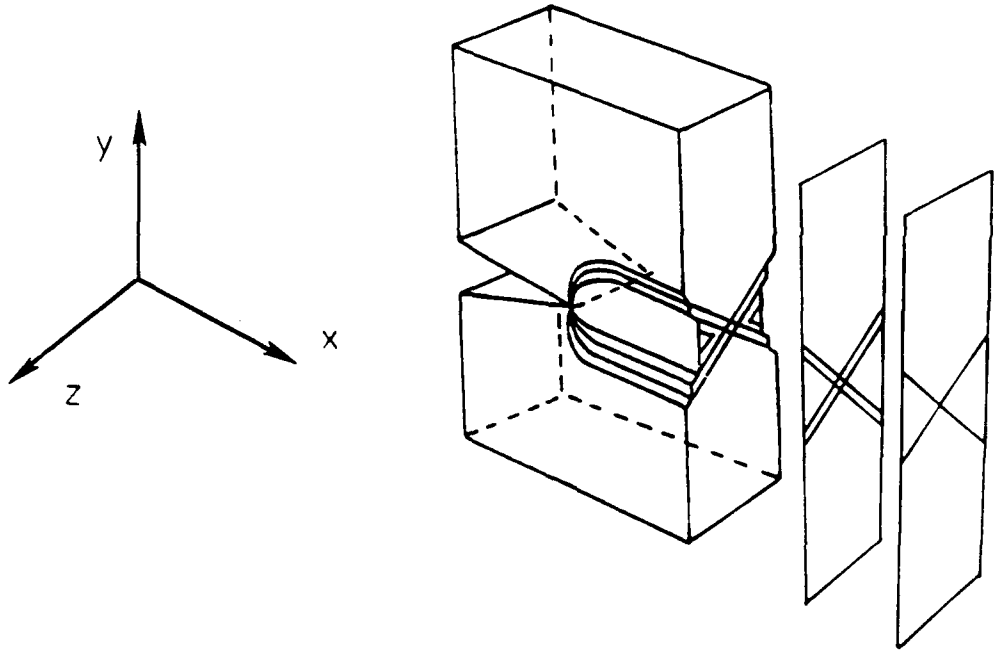

Figure 5.3 Three dimensional schematic diagram of the process zone

Figs. 5.4a-d show the surfaces of specimens at their equilibrial process zone state after fracture in liquid nitrogen. The fracture surfaces generated within the process zones are relatively smooth compared to those outside the process zones. The final equilibrial process zone size is determined based on the side-view, the thinning profile and fracture surfaces.

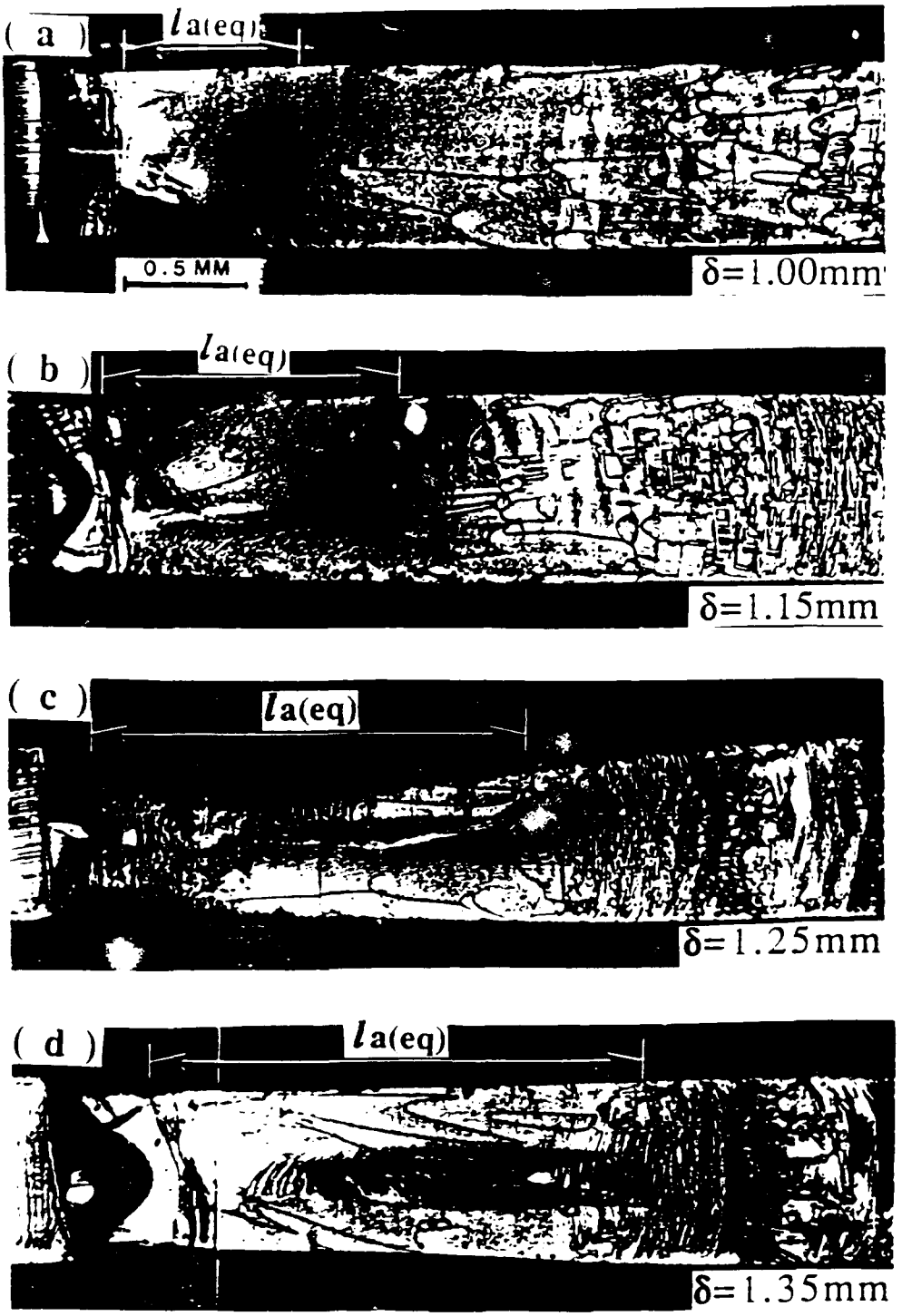

Figure 5.4 a-d) Fracture surfaces of equilibrium process zones fractured in liquid nitrogen

The stress-relaxation behavior during the test is given in Fig. 5.5. The dashed lines indicate the values of remote stress, σ_∞, at an apparent equilibrium. This stress behavior will be utilized in modelling in a subsequent paper.

The kinetics of the process zone evolution is depicted in Fig. 5.6 which shows the process zone length, l_a, versus time for SEN specimens for the four experimental conditions described previously. The process zone is seen to reach at least half of its final length during the initial ramp loading and then follows an increasingly slower approach to an apparent equilibrial size ($l_{a(\mathrm{eq})}$) dependent on the displacement. The dashed lines in Fig. 5.6 represent the values of the equilibrial sizes. Some relatively small crack growth from the notch-tip occurred during the initial loading and for a short period thereafter, particularly at the highest strain loading. However, the crack is arrested soon after the stress relaxation starts and remains stationary during subsequent process zone evolution. Thus this process occurs at essentially constant crack length. Fig. 5.6 represents the process zone evolution data acquired at this stage.

The rate of the process zone length, $\dot{l}_a$, evaluated from Fig. 5.6, is shown in Fig. 5.7 as a function of, $l_{a(\mathrm{eq})}$-l_a, scaled by the equilibrial length, $l_{a(\mathrm{eq})}$, a measure of the deviation from the equilibrium. The rate of four different loading strains apparently show different kinetics. This means that identification of the appropriate scaling factors in the kinetic equations needs to be attempted to develop a master curve.

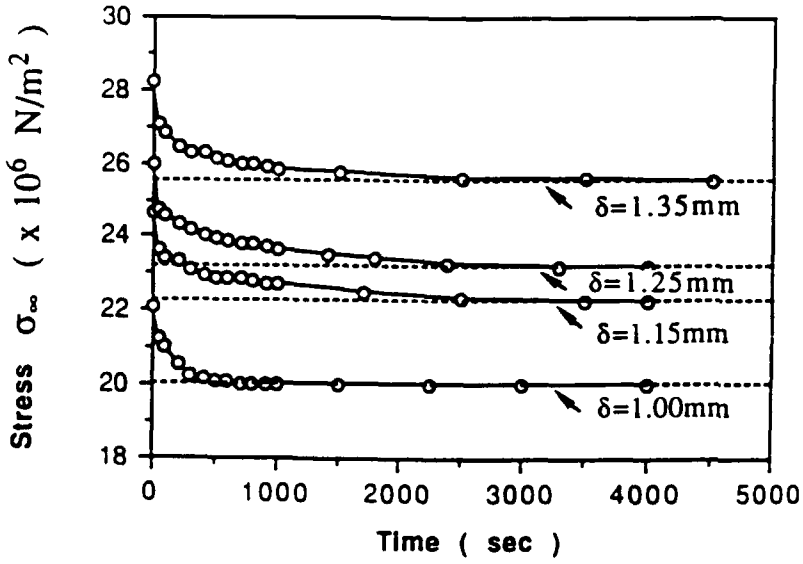

Figure 5.5 Stress relaxation data at various displacements in SEN

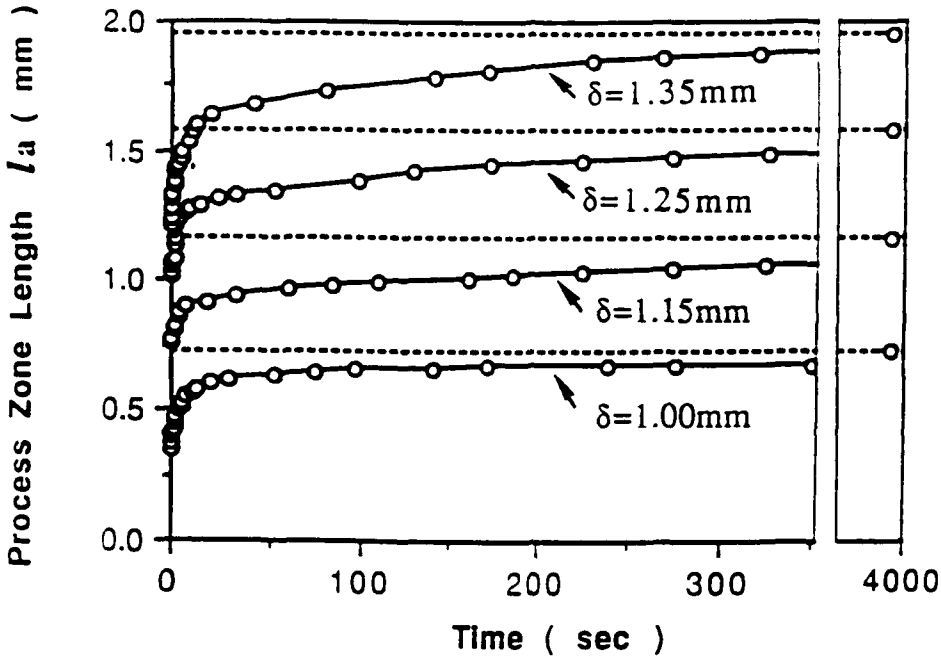

Figure 5.6 Process zone length, *la* (mm) vs time (sec)

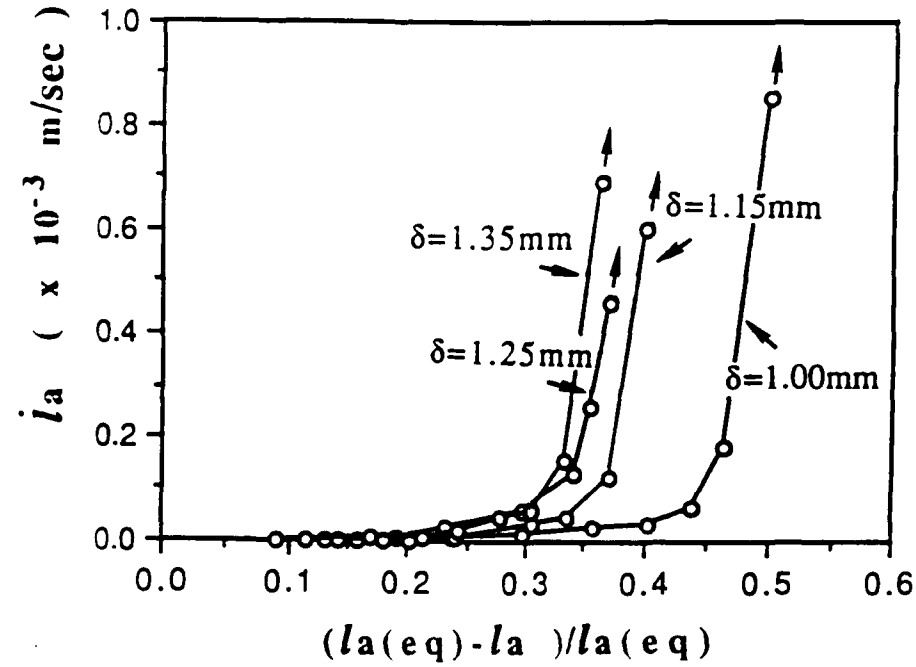

Figure 5.7 Rate of the process zone growth, $\dot{l}_a$ vs (*la*(eq)-*la*) / *la*(eq)

As described earlier, the process zone consists of two intersecting families of shear bands with orientation $\pm 59^{\circ}$ with respect to the X-Y plane which are non-homogeneous in density, see Figs. 5.2b and 5.3. The number of shear bands and the band width diminish with distance from the notch along the X-direction. The cumulative effect of the shear bands gives rise to the thinning profile. The gradient of the thinning provides the shadow seen in the side view on video screen (Fig. 5.2a) and distinguishes the boundary of the process zone and undeformed material.

As described previously in the experimental section, the relative density of shear bands is obtained from the enlargement of the optical micrograph Fig. 5.2b. The contours of equal levels of apparent shear band density is shown in Fig. 5.8. The maximum shear band density corresponds to the plane of the crack. The shape of the contours follows the conventional plastic zone behavior although there is some asymmetry which may be attributed to the sequence of shear band formation.

Haddaoui et al [59] drew an analogy of the thinning due to shear band formation in fatigue with necking phenomenon(cold drawing). If this is so, the material properties and formation of shear bands (drawn material) can be estimated separately from the tensile test. In Fig. 5.9 the tensile engineering stress-strain curves are shown for the original undeformed and drawn material. The polycarbonate was determined to have Youngs Modulus 2.08 GPa, with yield strength σ_y = 57.7 MPa, followed by necking with constant drawing stress, σ_{dr} = 47.9MPa until the material in the waist section was exhausted. As is well described elsewhere [64,65], the transition in material occurs in a localized zone between the untransformed and transformed regions. The draw ratio was determined as 1.60 for polycarbonate tested here and remained constant throughout the process of neck propagation. The specimens of drawn material showed uniform deformation until fracture with a modulus value of 3.53 GPa which accounts for the essentially constant value of draw ratio during the tensile test. These results could be used to construct a true stress-strain curve similar to that determined for polycarbonate from careful stress-optical measurements [66].

A linear correlation between the apparent average shear band density along the thickness (z direction at y) and the thinning of the thickness (at y) is shown in Fig. 5.10. The data points were measured from Figs. 5.2b and 5.8. The correlation coefficient is 0.984. Indeed the linear relationship implies that the integral density of shear bands across the thickness can be evaluated indirectly by measuring the thinning. Though the relationship was examined for one cross-section, it can be justified and generalized by the existence of a characteristic slip distance during formation of a shear band which was observed by J. Grenet et al. [67].

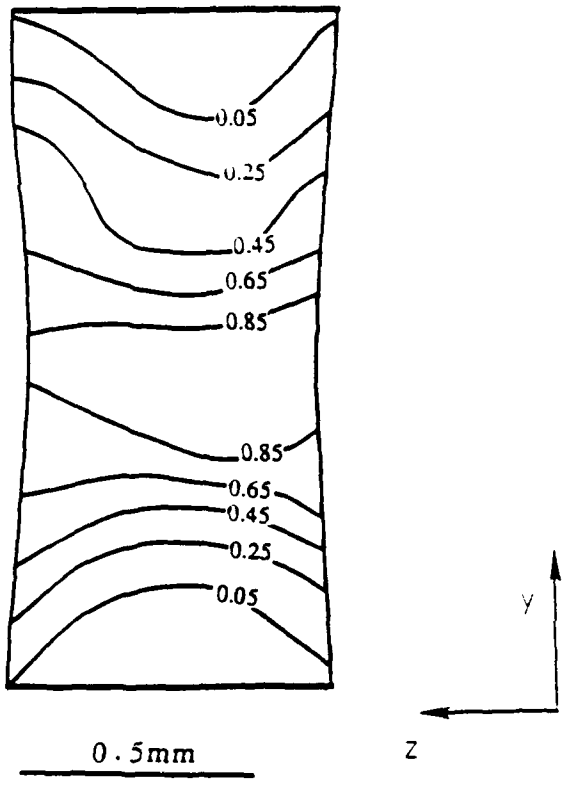

Figure 5.8 Contour map of apparent shear band density in the Y-Z plane

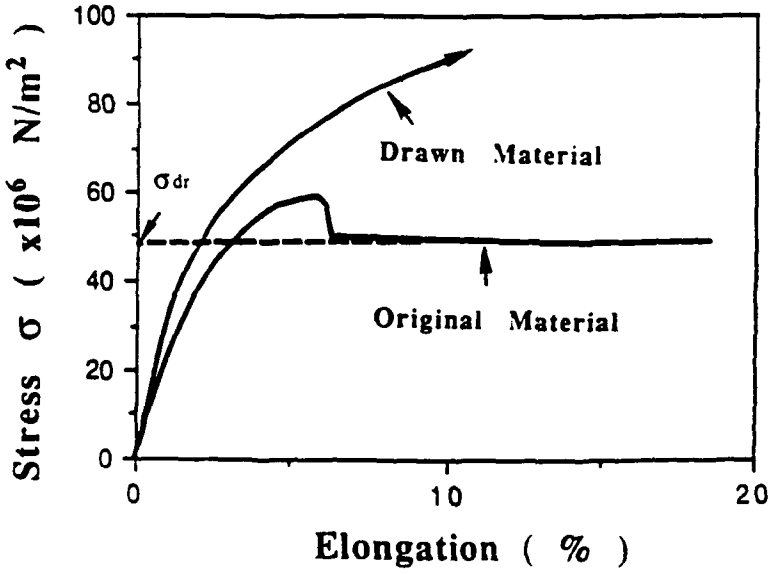

Figure 5.9 Tensile stress-elongation curves of original and drawn polycarbonate

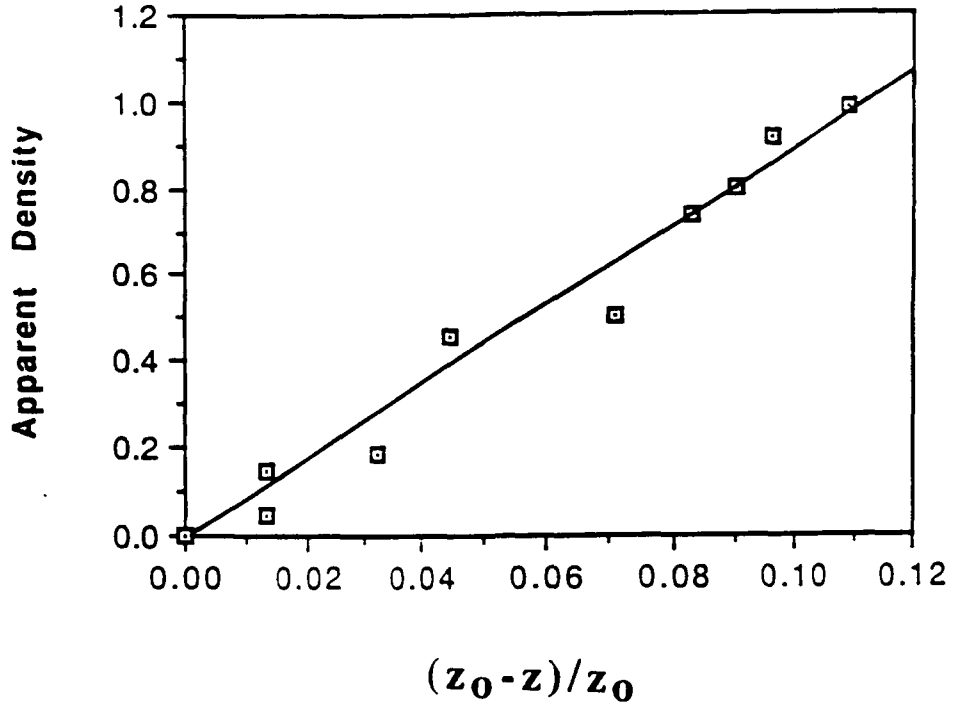

Figure 5.10 A linear correlation between the apparent average shear band density and the thinning in the process zone

Based on the above, the thinning in the process zone was measured to evaluate the density of shear bands (drawn material). The equal contour levels of relative thinning in four different equilibrial process zones are shown in Fig. 5.11. Here the relative thinning is defined by the ratio of the thinning measured in the process zone to the thinning of necked material in the tensile test, Δz(zone) / Δz(neck). If the density of drawn material in necking is defined as 1, the relative ratio represents the density of shear bands in the process zone. The average values of this ratio are 0.19, 0.28, 0.35, 0.35 at load displacements 1.00, 1.15, 1.25, 1.35 mm, respectively.

Summary

1. An experimental procedure for the study of the kinetics of the process zone evolution decoupled from the kinetics of crack growth for polycarbonate was designed and implemented. This was achieved by observing the process zone evolution under stress-relaxation at essentially constant crack length.

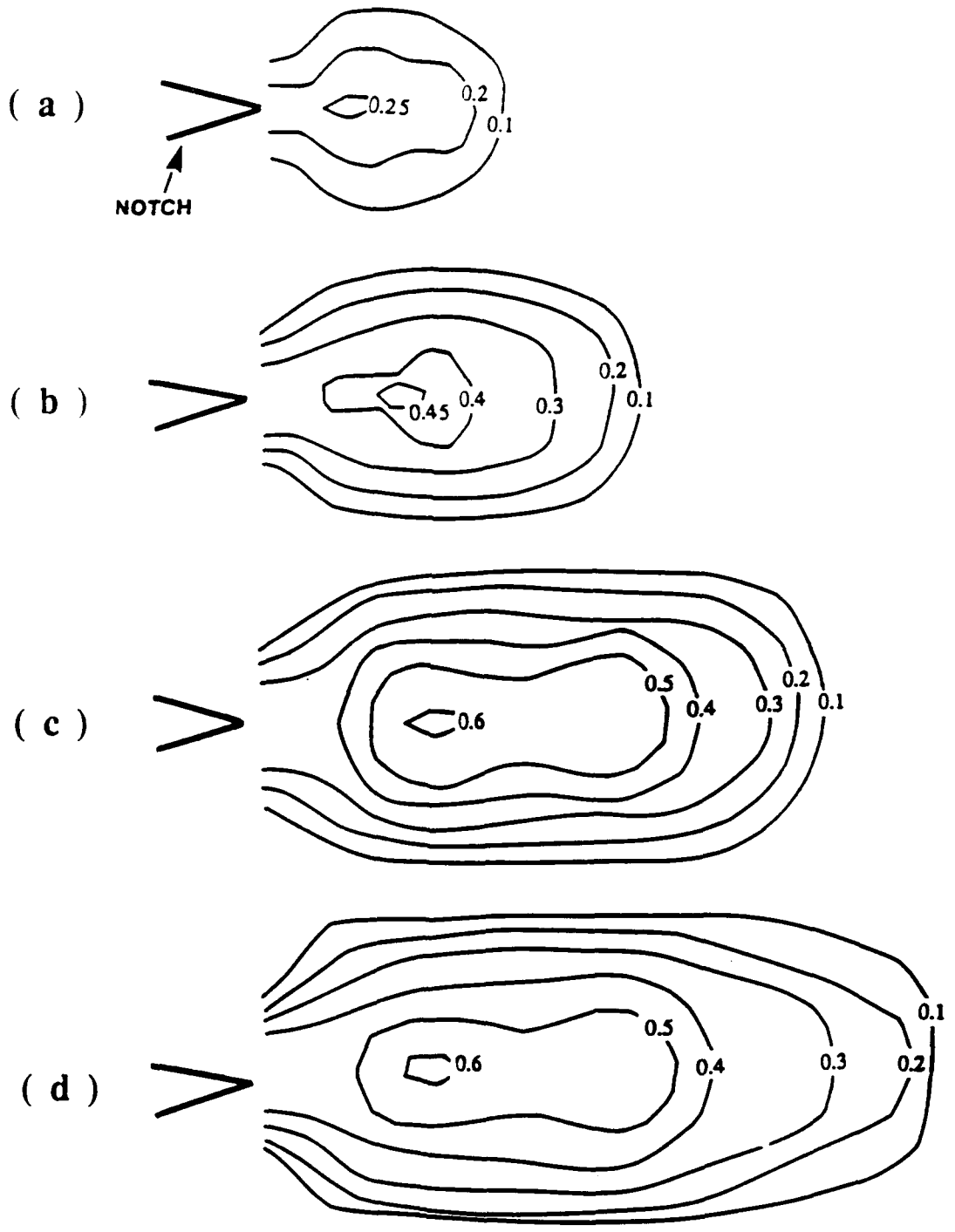

Figure 5.11 Equal level contours of relative thinning in the process zone

2. The process zone was reconstructed based on the side-view, the thinning profile and liquid nitrogen fracture surface and found to consist of two intersecting families of shear bands with orientation $\pm 59^{o}$ with respect to the X-Y plane and with variable density. The variation of the shear band density was mapped using contour lines of equal relative thinning.

3. The kinetics of the rate of growth of the process zone length were investigated during stress relaxation. The size and time to reach an equilibrium process zone were dependent on the level of strain imposed.

4. The kinetics of the process zone evolution was evaluated in terms of the relative deviation of the current process zone size from its equilibrial value. However, this parameter does not provide adequate scaling. Thusthe challenge remaining is the determination of a suitable parameter to generate a master curve for various experimental conditions.

5.2 Process Zone in Stress Relaxation Experiment

Introduction

In our previous paper we reported the evolution of the process zone ahead of a crack under stress-relaxation at a constant crack length in a polycarbonate [14]. The evolution of the process zone was evaluated in terms of the relative deviation of the current process zone size from its equilibrial value. However, this parameter did not allow us to generate a master curve for the various experimental conditions. The goal of this paper is to construct a constitutive equation for process zone growth employing thermodynamic considerations.

A thermodynamic model for an equilibrial process zone in polymers was recently proposed by Chudnovsky [11] and its validity was supported by the experimental studies on various polyethylenes [10,12]. The essence of the Chudnovsky model (CM) is that the process zone can be considered as a homogeneous second phase, i.e., transformed material, and thus the shape and the size of the process zone are derived from the phase equilibrium conditions.

The experimental examination of CM has been performed on polyethylene for which the assumption of the homogeneity of the transformed (drawn) material within the process zone is quite adequate. However, the observation of the process zone in polycarbonate, PC, shows an important difference; it consists of shear bands whose density varies noticeably within the zone. Similarly, in examination of neck formation under uniaxial tension of PC one observes a spectrum of intermediate stages between the initial and fully drawn (transformed) material. In the

present paper we improve the CM to account for the variable extent of transformation of material within the process zone. Further we employ the improved model to determine the process zone driving force and then formulate an appropriate kinetic equation following the framework of irreversible thermodynamics. An analysis of the parameters of the model as well as the comparison with experimental data are also presented.

Review and Generalization of Thermodynamic Model

Let G be the Gibbs potential of the system described in Fig. 5.12 and V_{pz} be the domain occupied by the process zone. Then for isothermal condition the equilibrial domain V_{pz} of the process zone corresponds to the minimum of G, i.e.:

$$\frac{\delta G(\sigma_\infty, V_{pz})}{\delta V_{pz}}\Big|_{l=\text{const}} = 0 \qquad (5.1)$$

Here, G is a functional of the domain V_{pz} and a function of crack length l and applied stress σ_∞.

Following the reference [20], we employ the Eshelby method to evaluate a variation of the Gibbs potential due to a virtual migration of the process zone boundary:

$$\delta G = -\int_{\partial V_{pz}} \delta\xi_i \, (P^o_{ij} - P^{pz}_{ij}) \, n_j \, d\Gamma \qquad (5.2)$$

For evaluation of the Gibbs potential, G, of a crack with the surrounding process zone consisting of the second phase (see Fig. 5.13a), the two-phase system was decomposed into its elements as shown in Fig. 5.13b. The first element results from removal of the process zone and substituting its action with an equivalent traction σ_{dr} along the interface (σ_{dr} is the drawing stress). The second element is the process zone V_{pz} within which the original material submitted to σ_{dr} undergoes the transformation (drawing). The width, w_o, of the layer of the original material in Fig. 5.12 which underwent transformation varies along the process zone length x_1 and is initially unknown. The resulting width, $w^*(x_1)$ of the process zone is $w^*(x_1) = \lambda(x_1)w_o(x_1)$ with λ being the draw ratio and assumed constant within the process zone. The displacement caused by the

transformation at the interface shown in the element 2 of Fig. 5.13b is $w^*(x_1) - w_o(x_1)$.

Then the coherency of the interface requires that the opening of a slit in the element 1 should be equal to the displacement of the boundary of the element 2. For a slender process zone the displacement of the element 1 can be approximated as the crack opening displacement, Δ, thus leading to the following compatibility equation.

$$\Delta(x_1, l, l_a) = w^* - w_o \tag{5.3}$$

Then the width $w_o(x_1)$ of the initial strip which is transformed into the process zone is directly related to the crack opening displacement of the element 1 in Fig. 5.13b:

$$w_o(x_1) = \Delta(x_1, l, l_a)\,(\lambda - 1)^{-1} \tag{5.4}$$

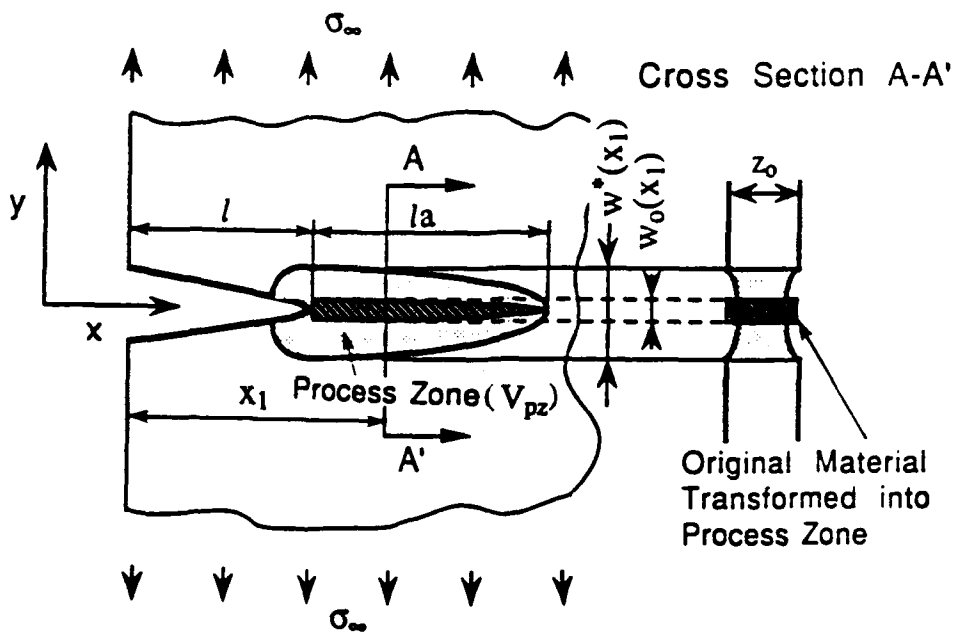

Figure. 5.12 Schematic diagram of crack and process zone in polycarbonate.

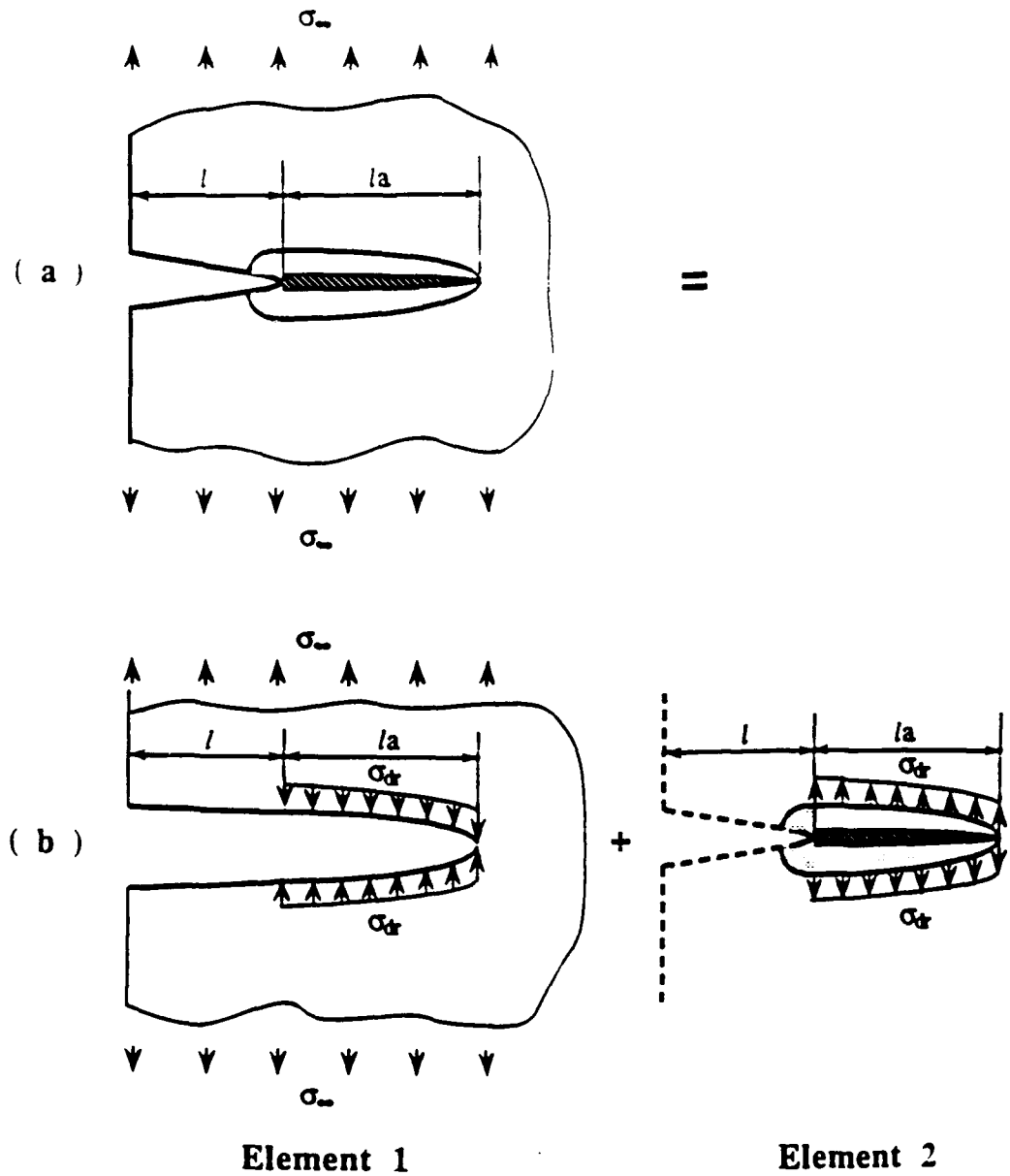

Figure. 5.13 A model for the computation of Gibbs potential: Element one is obtained from removal of the process zone and substituting its action with an equivalent traction σ_{dr} along the interface, and element two is obtained from the process zone V_{pz} within which the original material submitted to σ_{dr} undergoes the transformation.

Thus, the volume V_{pz} of the initial material can be expressed as:

$$V_{pz} = z_o \int_{l}^{l+l_a} \Delta(x_1, l, l_a)\,(\lambda - 1)^{-1} dx_1 \tag{5.5}$$

where z_o is the initial thickness of the specimen. Thus the process zone shape is uniquely determined by the process zone length, l_a, because the crack opening displacement depends on l, σ_∞, σ_{dr}, and l_a. Thus, the condition for the minimum Gibbs potential for two-phase system equilibrium can be written as:

$$\left.\frac{dG(\sigma_\infty, l, l_a, \sigma_{dr}, \lambda)}{dl_a}\right|_{l=\text{const}} = 0 \tag{5.6a}$$

$$\left.\frac{d^2G}{dl_a^2}\right|_{l=\text{const}} > 0 \tag{5.6b}$$

The equation (5.6a) leads to the following equation [11]:

$$K^{tot}(K^{tot} + \tilde{\gamma}K(\sigma_{dr})) = 0 \tag{5.6c}$$

and the inequality Eq. (5.6b) ensures the uniqueness of the solution, i.e.:

$$K^{tot} + \tilde{\gamma}K(\sigma_{dr}) = 0 \tag{5.7}$$

Here K^{tot} is the stress intensity factor (SIF) for the element 1 of Fig. 5.13a, $K(\sigma_{dr})$ is the SIF for the same element with absence of σ_∞. $\tilde{\gamma}$ represents $2\gamma^* / ((\lambda - 1)\sigma_{dr})$ where γ^* is the specific transformation energy. This solution leads to the equilibrial process zone size and shape which agree well with experimental observations on polyethylene and thin film polycarbonate [10,11].

As mentioned previously, polycarbonate was observed to undergo non-homogeneous transformation within the process zone, Fig. 5.14 showing the optical micrograph in polarized light and the schematic diagram of the two intersecting families of shear bands in cross section A-A'. we consider the individual shear band as transformed material. Between the shear bands the material appears to be untransformed.

During the evolution of the process zone, drawing progresses by a) an increase of the number of shear bands, and b) increase of the width of the individual shear bands at the expense of the neighboring untransformed material [53]. The various stages of drawn state correspond to different densities of shear bands.

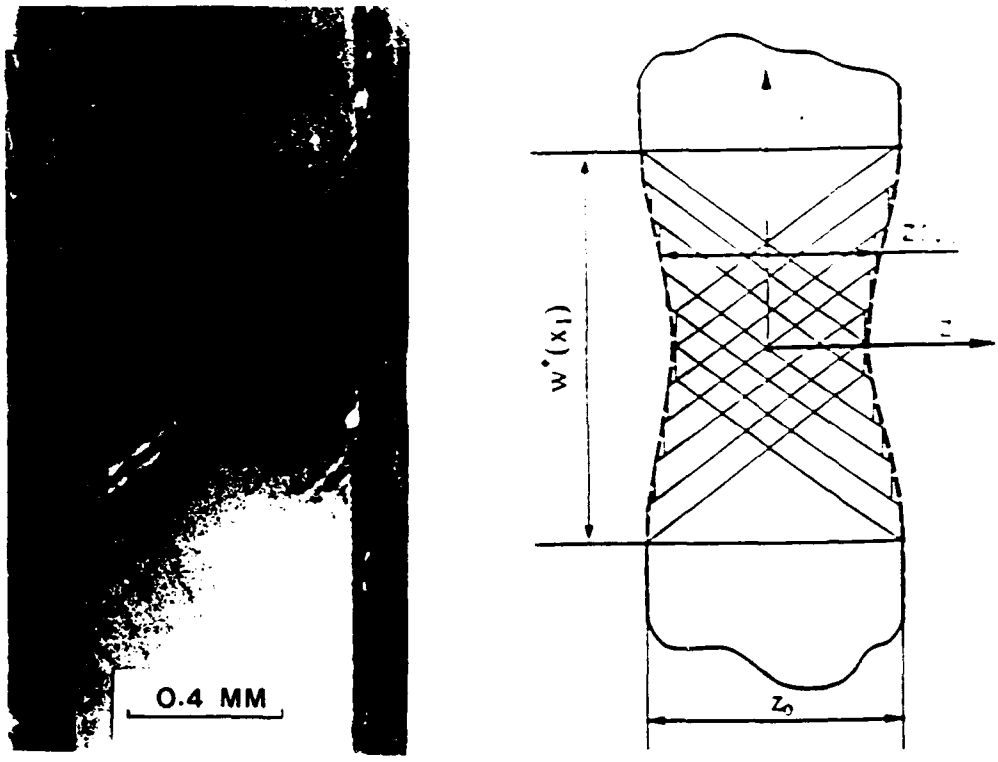

Cross Section A-A'

Figure 5.14 Micrograph and schematic diagram of intersecting families of shear bands in a cross-section of the process zone.

To characterize an intermediate transformation we introduce an extent of transformation ζ. ζ=0 corresponds to the original state and ζ=1 is associated with the fully transformed state. The thinning of cross-section is a cumulative effect of the shear banding as illustrated in Fig. 5.14. The thinning and the draw ratio, λ, are uniquely related since the density of transformed material is practically unchanged (a few percent) [10]. The extent of transformation ζ is simply related to the draw ratio λ:

$$\zeta = \left(\frac{\lambda - 1}{\lambda}\right)\left(\frac{\lambda^*}{\lambda^* - 1}\right) \tag{5.8}$$

where λ^* is the draw ratio for fully transformed material and λ is a variable draw ratio reflecting a current extent of transformation. A correspondence between an extent of shear banding and λ has been discussed in our previous paper [14]. It has been also found that the extent of transformation varies within the analyzed process zone. Moreover the distributions of ζ for process zone formed under different conditions are noticeably different.

Let us consider an average draw ratio $\lambda(x_1)$ for the cross-section at x_1:

$$\lambda(x_1) = \frac{1}{w^*}\int_{-\frac{w^*}{2}}^{\frac{w^*}{2}} \frac{z_o}{z(x_1, y)}\, dy \tag{5.9}$$

Here z_o represents the thickness of original material and z that in the process zone. Then the average extent of transformation ζ in the cross-section with coordinate "x_1" (see Fig. 5.12) is given as

$$\zeta(x_1) = \left(\frac{\lambda(x_1) - 1}{\lambda(x_1)}\right)\left(\frac{\lambda^*}{\lambda^* - 1}\right) \tag{5.10}$$

The thinning profiles presented in Fig. 11 of the reference [19] were used to give the average extent of transformation, $\zeta(x_1)$, and the average draw ratio, $\lambda(x_1)$, along the process zone. Shown in Fig. 5.15 are the values of the $\zeta_{eq}(x_1)$ as a function of the x_1 normalized by the equilibrial process zone size, $l_{a(eq)}$, for the various fixed displacements. Noticed in Fig. 5.15 is the similarity of the shape of $\zeta(x_1/l_{a(eq)})$ and the monotonic increase of the amplitude of $\zeta_{eq}(x_1)$ with the displacement. This suggests that the evolution of the extent of transformation follows a self-similar pattern which can be formally expressed as follows:

$$\zeta\left(\frac{x_1}{l_a(t)}, t\right) = \frac{l_a(t)}{l_{a(eq)}}\,\zeta_{eq}\left(\frac{x_1}{l_a}\right) \tag{5.11}$$

Here, t is time. In order to evaluate the Gibbs potential we first need to introduce an effective specific energy, γ, which is related to ζ as follows:

$$\gamma\left(\frac{x_1}{l_a(t)}, t\right) = \gamma^* \zeta\left(\frac{x_1}{l_a(t)}, t\right) \tag{5.12a}$$

γ^*, in thermodynamic terms, is the difference in chemical potential (per unit volume) across the boundary of untransformed and fully transformed material. Then the dimensionless factor $\tilde{\gamma}$ also becomes a function of x_1 and time:

$$\tilde{\gamma}\left(\frac{x_1}{l_a(t)}, t\right) = \frac{2\gamma\left(\frac{x_1}{l_a(t)}, t\right)}{\left[\lambda\left(\frac{x_1}{l_a}\right) - 1\right]\sigma_{dr}} \tag{5.12b}$$

At equilibrium, the Gibbs potential depends explicitly on $l_{a(eq)}$ similar to that in the CM as well as implicitly through the extent of transformation. As a result, the Eq. (5.12a) which is the necessary condition of the minimum Gibbs potential is rewritten as:

$$\frac{\partial G}{\partial l_a}\Big|_{l=\text{const}} + \frac{\delta G}{\delta \zeta}\frac{d\zeta\left(\frac{x_1}{l_a}\right)}{dl_a} = 0 \tag{5.12c}$$

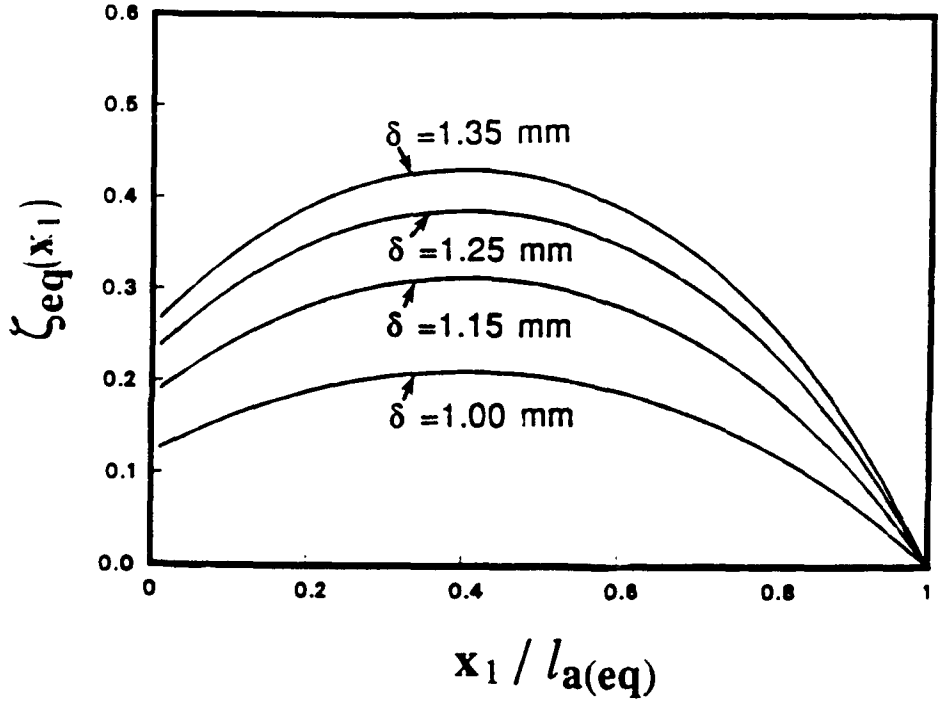

Figure 5.15 Profiles of average extent of transformation as function of $x_1/l_{a(eq)}$ for various applied displacements.

The equation (5.12c) determines the size of equilibrial process zone. Figure 5.16 shows the solution of equation (5.12c) (solid line) with $\gamma^* = 7.05 \times 10^6$ J/m^3 for the various fixed displacement conditions. The experimental data points are shown by the open circles. Only one parameter is employed in the above treatment for the four experimental conditions reported. The justification of this value comes from independent tests using the neck formation in simple tension combined with calorimetric determination of the residual strain energy stored in the transformed (necked) material and estimation of heat generation during the transformation.

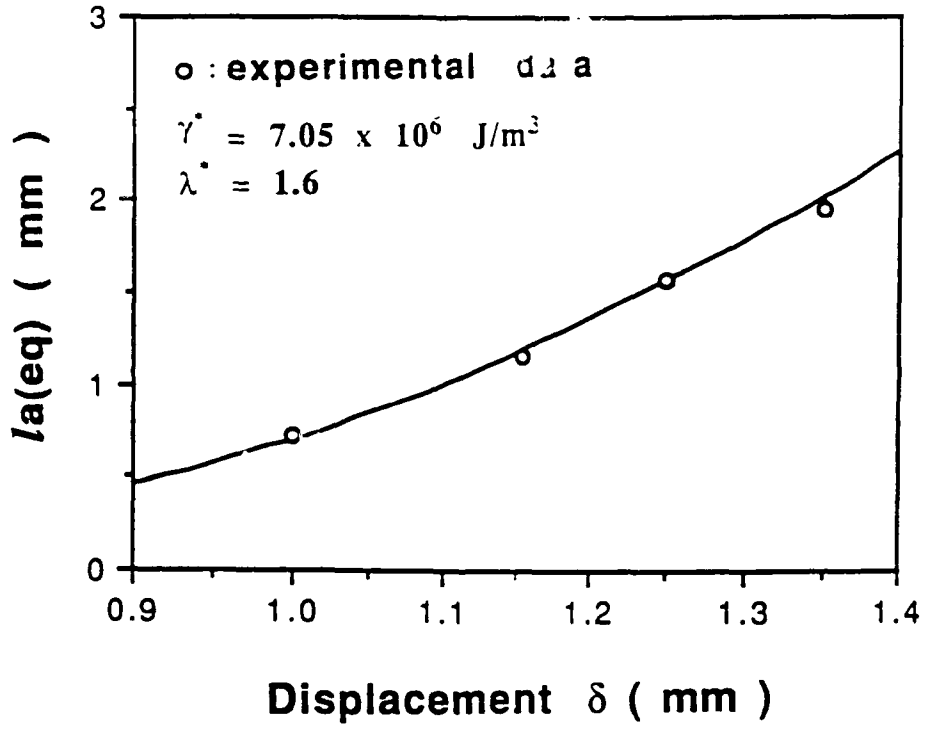

Figure 5.16 Equilibrial process zone size as a function of applied displacements. The solid line represents the theoretical solution.

Process Zone Driving Force

The force on an interface between original material and the process zone can be defined following Eshelby [43]. In our case the evolution of

the interface is uniquely determined by the process zone length, l_a as a function of time. The driving force X_{pz} is determined as:

$$X_{pz} = - \frac{dG}{dl_a}\Big|_{l=const} \tag{5.13}$$

Repeating the arguments prior to the equation (5.12c) on the dependency of G on l_a, the process zone driving force can be presented as:

$$X_{pz} = - \left[\frac{\partial G}{\partial l_a} |_{l=const} + \frac{\delta G}{\delta \zeta} \frac{d\zeta\left(\frac{x_1}{l_a}\right)}{dl_a} \right] \tag{5.14}$$

The details of the calculation of equation (5.14) will be reported separately. If the transformation of material within the process zone is homogeneous the CM is recovered. It corresponds to the first term in the RHS of the Eq. (5.14). Figure 5.17 shows the dependency of the process zone driving force as a function of $l_a / l_{a(eq)}$ for the four experimental displacement conditions. At equilibrium the process zone driving force is zero.

The kinetic equation of process zone evolution.

In irreversible thermodynamics for systems close to equilibrium that the rate of change toward the equilibrium is assumed to be proportional to the corresponding driving force, X. In our case the rate of approaching equilibrium is defined by the rate of changes in l_a, i.e., $\dot{l}_a$. Thus a kinetic equation can be written as:

$$\dot{l}_a = kX_{pz} \tag{5.15}$$

A different approach has been widely considered in studies of failure kinetics. For example, Zhurkov in his studies of the kinetics of fracture of solids under creep conditions found that a wide range of materials followed a stress biased Ree-Eyring failure kinetic equation [68]:

$$t_f = A_o \exp\left(\frac{U - \phi\sigma}{RT} \right) \tag{5.16}$$

where t_f is the time to failure, T is the absolute temperature, R is the gas constant, A_o is the characteristic time and ϕ is a factor accounting for the effectiveness of reducing the activation energy, U, by the applied stress, σ. The equation (5.16) was applied to uniaxial specimens of small diameter for which the fracture propagation time was negligible compared to the crack initiation time.

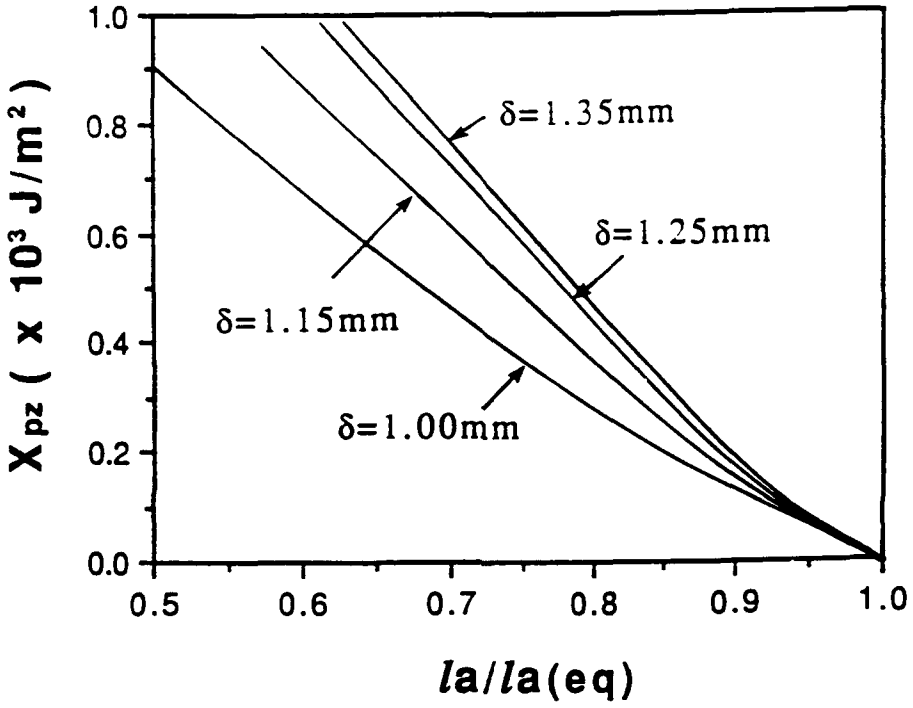

Figure 5.17 Process zone driving force as function of $l_a / l_{a(eq)}$ for various applied displacements.

An energy release rate biased Ree-Eyring equation was proposed with argument that the crack rate $\dot{l}$ is inversely proportional to the fracture time on the molecular level and the stress at the crack tip is proportional to the energy release rate G_1 by a relationship such as $\sigma = G_1/\Delta$ where Δ is the crack opening displacement:

$$\dot{l} = A_1 \exp\left(- \frac{(U - \alpha G_1)}{RT} \right) \qquad (5.17)$$

where $\dot{l}$ is crack velocity, and A_1 and α are constants. Equation (5.17) was adapted in studies of crack growth in PMMA [69]. A similar kinetic equation for alcohol assisted craze growth in PC was proposed [70]. The short-coming of these types of exponential equations is the absence of an equilibrial state.

Since the driving force X_{pz} can be decomposed into two parts, i.e., a resistant part and a driving part.

$$X_{pz} = -\frac{dG}{dl_a} = -\left(\gamma^* \frac{\partial V_{tr}}{\partial l_a} - \left(-\frac{\partial \Pi}{\partial l_a}\right)\right) \tag{5.18}$$

where V_{tr} is the transformed volume of process zone and Π is the potential energy of system. The resistant part has an analogy with activation energy U and the driving part has with energy release rate G_1 in the equation (5.17).

The Arrhenius equation was first developed to account for the temperature dependency of the reaction rate constant, k, in chemical kinetics. The equation (5.15) resembles that of a first-order chemical reaction and so adapting the Arrhenius assumption of k with incorporation of an activation energy reduced by the process zone driving force we propose the following equation for the kinetic coefficient in the Eq. (5.15):

$$k = k_o \exp\left(-\frac{U - \alpha X_{pz}}{RT}\right) \tag{5.19}$$

where α is a constant with units m^2/mole. Finally, combining the Eq. (5.19) with Eq. (5.15) we arrive at a new kinetic equation as follows:

$$\dot{l}_a = \left[k_o \exp\left(-\frac{U - \alpha X_{pz}}{RT}\right)\right] X_{pz} \tag{5.20}$$

Note that the equation (5.20) accounts for an equilibrial state ($\dot{l}_a = 0$ when $X_{pz} = 0$) and becomes increasingly nonlinear with increasing X_{pz}, that is to say with increasing departure from the equilibrium.

Since the experiments reported in the reference [19] were performed at one temperature the equation is simplified and the data cast as $\ln(\dot{l}_a)$ versus X_{pz} in Fig. 5.18. The solid line indicates the fit of equation (5.20) with a constant α as 16.39×10^3 (m^2/ kmol). The unit of k_o is m^4/(J-sec). The strongly nonlinear kinetics data are now collapsed into a master curve.

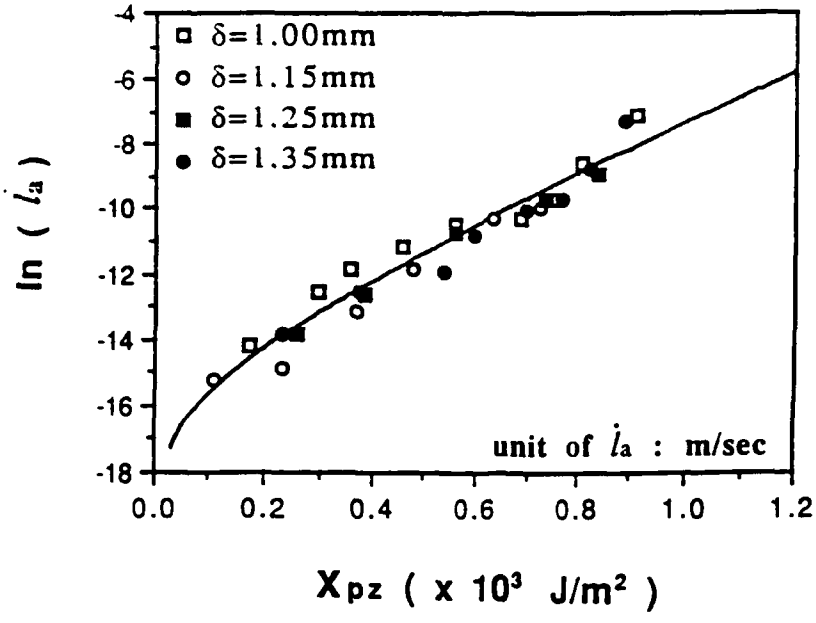

Figure 5.18 A master curve for process zone kinetics.

Conclusion

A generalization of Chudnovsky Model is made to account for non-homogeneous transformation of material within a process zone surrounding a crack.

The distribution of the extent of transformation was experimentally determined in these studies. Further improvement of the model using the variation of Gibbs potential should allow for prediction of the distribution without experimental determination.

The driving force for the process zone evolution is evaluated and a new kinetic equation incorporating the driving force is proposed which leads to a master curve for the observed growth of the process zone under various loading histories.

The fundamental significance of the constants k_0 and α in the equation (5.20) and their relation to intrinsic material parameters as well as the applicability of the equation to account for temperature and various loading conditions are subjects for future scrutiny.

CHAPTER 6

CRACK LAYER GROWTH EQUATION AND STABILITY ANALYSIS

6.1 Crack Layer Growth Equation

Introduction

Many engineering polymers undergo cold drawing. A slow crack growth in such polymers is usually preceded by a process zone consisting of drawn material. The crack and the process zone are considered to be a single entity called the Crack Layer (CL). In ductile polymers such as polyethylene, nonmonotonic (discontinuous) CL growth has been reported under both creep and fatigue loading conditions [54,71-77]. Detailed observations of CL growth processes have been reported by Lu, et al. [75]. The existence of arrest lines (discontinuous CL growth) on the fracture surface of polyethylene has been noted as evidence of stick-slip crack propagation [71,72]. Crack blunting effects explain this phenomenon as demonstrated by Kinloch and Williams for epoxy resins [78]. However, crack growth in polyethylene is a slow process, and the process zone is formed simultaneously during crack growth [75]. Thus the blunting effect exists even during crack growth. Lu, et al. suggested that the breaking of craze fibrils is the key mechanism underlying CL growth in polyethylene [75]. Similar observations in polycarbonate have also been reported [79,80]. A schematic representation of nonmonotonic behavior of CL growth is shown in Fig. 6.1. Details of the mechanism of CL growth is discussed in the sections on CL growth mechanism and CL growth simulation. Constitutive equations that adequately describe discontinuous CL growth have not yet been formulated.

In this chapter constitutive equations for CL propagation are proposed, and analytical results are compared with the experimental observations reported in [80]. A new thermodynamic model of the equilibrium process zone presented in chapter 4 has been employed to evaluate CL driving forces. These forces are the essential elements of the constitutive equations.

Determination of Crack Layer Driving Forces

The process zone is modeled as a phase transformation localized in a thin strip ahead of the crack. Experimental observations supporting this consideration are presented elsewhere [54,72,75]. Figure 6.2 shows a schematic representation of the model: V_{tr} is the domain occupied by the

second phase (process zone); σ_∞ is the applied stress; l and l_a are the crack and process zone lengths respectively. The material within the strip of width $w_0(x_1)$ undergoes transformation (drawing) at a constant draw ratio λ. The resulting process zone of width $w^*(x_1)$ is indicated by the solid line.

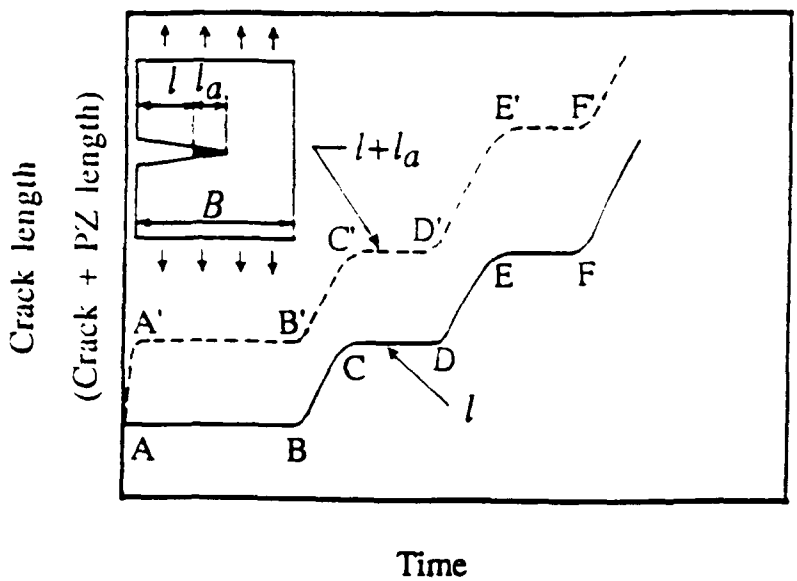

Figure 6.1: Schematic representation of nonmonotonic CL growth in ductile polymers.
BC, DE and so forth correspond to crack growths; AA', B'C', D'E' and so on correspond to process-zone growths; AB, CD, EF, A'B', C'D', E'F' and so forth reflect the time intervals (waiting time) between consecutive crack growths and the process-zone growths.

Using the assumption of a thin strip, V_{tr} is uniquely determined by the process zone length l_a for given values of l and σ_∞. In this case the Gibbs potential of the system (per unit thickness) can be expressed as a simple superposition of Gibbs potential (the potential energy) G^I and G^{II} of the first and the second phases, and the fracture energy $2\gamma l$ associated with crack within the drawn material. The resulting equation is

$$G = G^I + 2\gamma l + G^{II} \tag{6.1}$$

where γ is the Griffith's fracture energy of the drawn material per unit area.

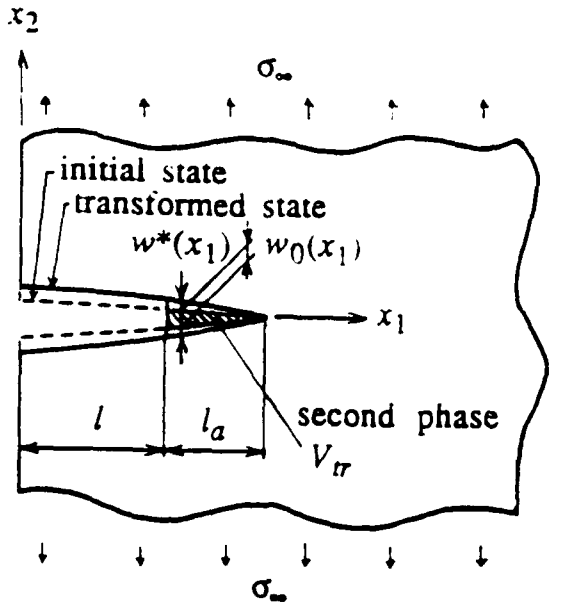

Figure 6.2 Model of the process zone as a phase transformation.

Using basic thermodynamics, the driving forces for the crack, X^{CR}, and the process zone, X^{PZ}, can be expressed as partial derivatives of the Gibbs potential with respect to corresponding variables (the crack length l and the process zone size l_a):

$$X^{CR} = -\frac{\partial G}{\partial l}\Big|_{l+l_a=const.} \tag{6.2}$$

$$X^{PZ} = -\frac{\partial G}{\partial l_a}\Big|_{l=const.} \tag{6.3}$$

Employing a standard fracture mechanics formalism (see Appendix C and [81]) the driving forces per unit thickness are

$$\text{Crack Driving Force: } X^{CR} = J_1 - 2\gamma \tag{6.4}$$

$$\text{Process Zone Driving Force: } X^{PZ} = \frac{K^{tot}}{E_0}\left\{K^{tot} + \frac{2\gamma_{tr}}{\sigma_{tr}(\lambda - 1)} K[\sigma_{tr}]\right\} \tag{6.5}$$

Here the active part of the crack driving force (the energy release rate because of crack extension into a stationary process zone) is

$$J_1 = \sigma_{tr}\left\{\delta^{tot} + \frac{\gamma_{tr}}{\sigma_{tr}(\lambda\text{-}1)}\,\delta[\sigma_{tr}]\right\} \tag{6.6}$$

K^{tot} is the stress intensity factor (SIF) and δ^{tot} is the crack tip opening displacement (CTOD at $x_1=l$) for the problem shown in Fig. 4.2a. $K[\sigma_{tr}]$ and $\delta[\sigma_{tr}]$ are, respectively, the SIF and CTOD for the same problem when $\sigma_\infty=0$. E_0 is the Young's modulus of the initial material.

The Mechanism of Crack Layer Growth

As an example, consider a single edge-notched (SEN) specimen with notch length l and specimen width B under a remote tensile stress $\sigma_\infty = 0.25\sigma_{tr}$. The equilibrium process zone size l_a^{eq} is determined by the condition $X^{PZ}(l,l_a^{eq},B,\sigma_\infty)=0$.

The process zone driving forces for various crack lengths are shown in Fig. 6.3. The abscissa is the process zone length l_a normalized with respect to the equilibrium process zone size l_a^{eq}. When the crack length is shorter than a certain critical value ($l/B \le 0.64$ in this case), the driving force decreases monotonically with the process zone length, and approaches zero as l_a approaches l_a^{eq}. For $l/B \ge 0.66$, the graph of X^{PZ} versus l_a/l_a^{eq} displays the nonmonotonic dependency which is typical for thermodynamic instability. First the process zone is formed in front of the crack. Then the process zone grows slowly, approaches its equilibrium length and is arrested. This part corresponds to region A-A' in Fig. 6.1.

The active part of the crack driving force (the energy release rate J_1) is shown in Fig. 6.4. The abscissa is the increment of crack length, normalized by the equilibrium process zone size for the initial crack length. If the crack resistance 2γ is greater than J_1, crack propagation will not occur. Thus the degradation of the material within the process zone by the action of the transformation stress σ_{tr} (reflected in the decrease of γ) is responsible for crack advance. Lu, et al. and Schirrer, et al. suggest that this degradation is the result of a slow process of disentanglement of the molecules within the fibrils constituting the process zone [75,79]. Therefore material degradation (the time dependence of γ) should perhaps be considered for modeling crack growth.

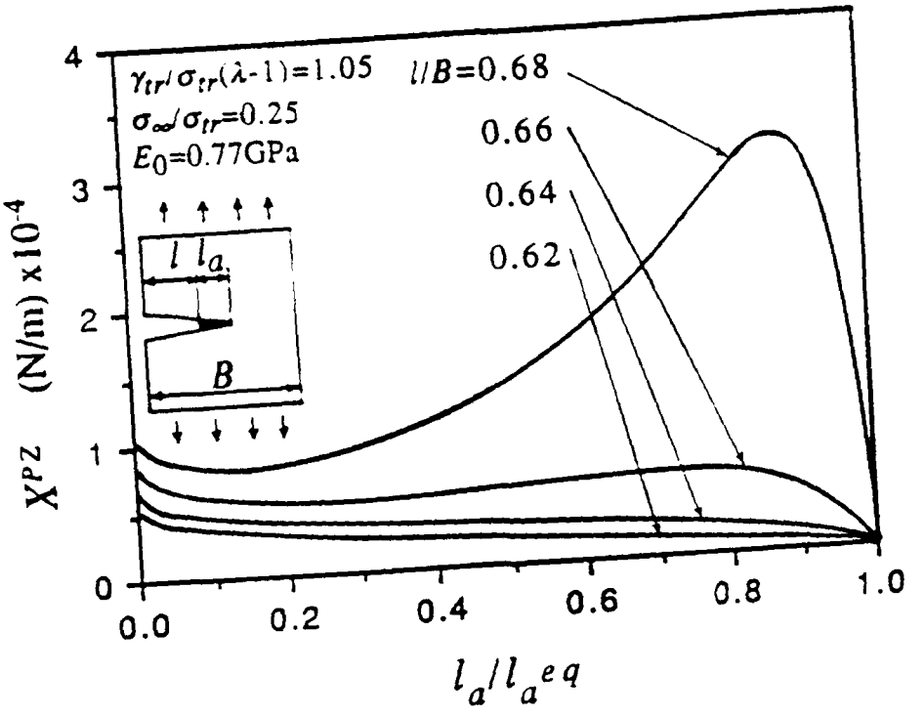

Figure 6.3 Process zone driving force versus normalized process zone length for various crack lengths.

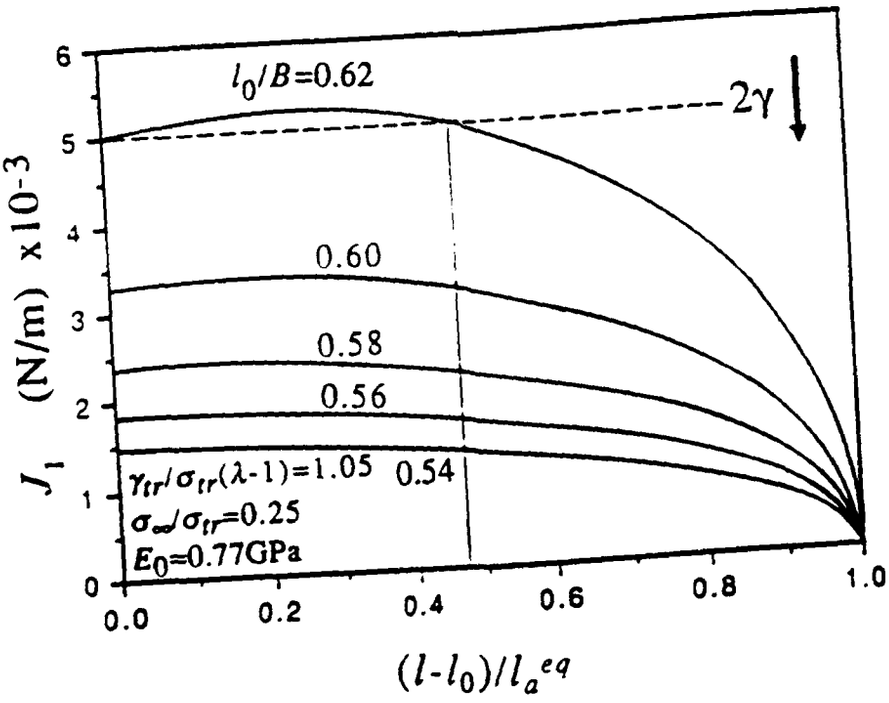

Figure 6.4 Active part of crack driving force J_1 versus normalized crack extension for various crack lengths.

At the moment when material transformation begins at a given point x_1, the degradation process simultaneously begins at x_1. It should be emphasized that each point x_1 of the process zone has its own initiation time, $t_i(x_1)$, for the degradation process. It is assumed that material degradation resulting in the decay of fracture energy γ is a first-order reaction. Assuming that γ=0 when the degradation is completed, γ can be expressed as

$$\gamma = \gamma_0 \exp\{-K\{t-t_i(x_1)\}\} \tag{6.7}$$

Here γ_0 is the initial value of the fracture energy at time $t_i(x_1)$ of material transformation at the point x_1, and K is a rate constant which obeys an Arrhenius-type equation [68].

When the crack advances it disturbs the equilibrium condition for the process zone, so that the process zone grows simultaneously with crack extension. When the crack enters the newly formed process zone, it is arrested because not enough time is available for material degradation to result in a sufficient decrease in 2γ. That is, 2γ of this region is still greater than J_1. However, 2γ in this domain later will become less than J_1 and the crack will again advance. This periodic pattern results in discontinuous CL growth. The actual values of $\gamma(x_1,t)$ vary from point to point, because the time at which the process zone is formed (the beginning of the degradation process in a given point) depends on the point.

When the crack length exceeds a certain critical length ($l_0/B \geq 0.58$ in this case), the second partial derivative of the Gibbs potential with respect to crack length changes sign. For example, when 2γ (dashed line in Fig. 6.4) approaches the value of J_1 for the initial crack length (l_0/B=0.62), J_1 is already greater than 2γ over half the region to the next arresting point. Thus when initiated, the crack jumps. However, the crack driving force decreases monotonically again after $(l-l_0)/l_a^{eq} \approx 0.5$.

Constitutive Equations

The evolution of CL is a slow (quasi-static) process. In thermodynamic equilibrium, both the fluxes and the driving forces are zero. It is therefore natural to assume that a homogeneous linear relationship exists between the fluxes and the conjugate forces near equilibrium:

$$\dot{l} = k_{11}X^{CR} + k_{12}X^{PZ} \tag{6.8}$$

$$\dot{l}_a = k_{21}X^{CR} + k_{22}X^{PZ} \tag{6.9}$$

Here k_{11},k_{12}, k_{21} and k_{22} are the kinetic coefficients. Relationships such as the above are often used in empirical laws. Examples include Fourier's law of heat conduction (heat flux is proportional to the gradient of temperature) and Fick's law of diffusion (the flux of matter is proportional to the gradient of concentration).

In the calculations of the next section, the coupling between the crack and the process zone kinetics is omitted for simplicity, so that k_{12}=k_{21}=0. Evaluating the kinetic coefficients in Eqs. (6.8) and (6.9) from experiments thus becomes easier. The methodology for evaluating the coefficients k_{11} and k_{22} is discussed in the following section.

The Evaluation OF Material Parameters

Equations (6.8) and (6.9) were solved numerically using the Runge-Kutta method. Figure 6.5 shows the simulation of the first three steps of the CL jumps. The time step for the numerical calculation is taken to be 30 minutes. The values of the material parameters used in the calculations for Fig. 6.5 are listed in Table 6.1. The model provides a good simulation of experimentally observed discontinuous CL growth. The parameters used in this model can be evaluated from the first two steps of CL kinetics (in other words, from short-term tests) as follows:

(a) Parameters related to drawing

The parameters such as σ_{tr}, λ and γ_{tr}, which are related to the material transformation (cold drawing) can be determined in an independent test such as a test on neck formation. The evaluation of these parameters for various polyethylenes is reported in [10].

(b) Parameters related to the degradation of fracture energy

The parameters γ_0 and K can be obtained from the crack initiation test. At the instant of crack initiation, the energy release rate equals 2γ. Since J_1 is known for a given crack and process zone size, measuring the time interval between the instances of load application and crack initiation (A-B in Fig. 6.1) gives the condition

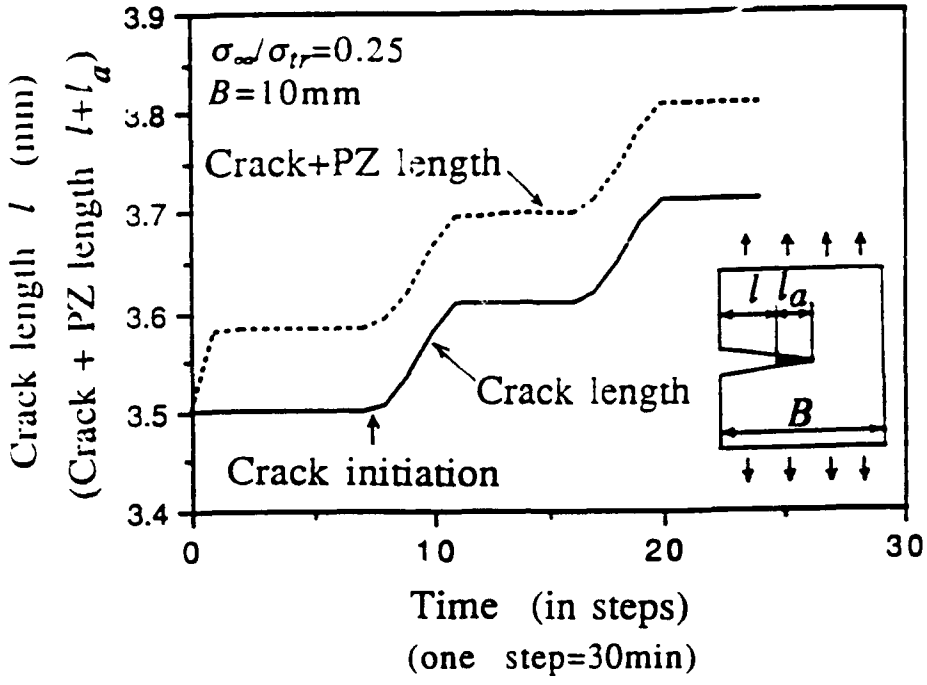

Figure 6.5 CL growth simulation.

Table 6.1: Material parameters used in the simulation

E_0 GPa	σ_{tr} MPa	γ_{tr} $\sigma_{tr}(\lambda\text{-}1)$	k_{11} m/Nsec	k_{22} m/Nsec	γ_0 J/m^2	K 1/sec
0.77	15.8	1.05	$1.5\text{x}10^{-10}$	$1.5\text{x}10^{-10}$	$1.5\text{x}10^{4}$	$3.5\text{x}10^{-4}$

$$J_1 = 2\gamma(\gamma_0, K) \tag{6.10}$$

which has two unknown parameters γ_0 and K.

Similarly, by measuring the time delay for the next crack growth (C-D in Fig. 6.1), another condition can be obtained for a different value of J_1 (for different crack and process zone lengths) having the form of Eq. (6.10). Thus one can determine the unknowns γ_0 and K from these two equations.

(c) Kinetic coefficients

In order to evaluate the kinetic coefficients k_{11} and k_{22}, it is necessary to measure the time for crack and process zone growths (A-A' and B-C in Fig. 6.1). When the load is applied, process zone formation begins immediately, but the crack remains at the initial position (A-B' in Fig. 6.1). Thus from Eq. (6.8),

$$k_{22} = \frac{1}{\Delta t} \int_{l_0}^{l_0 + l_a^{eq}} \left(X^{PZ}(x_1) \right)^{-1} dx_1 \tag{6.11}$$

where l_0 is the initial crack length, l_a^{eq} is the equilibrium process zone size for the fixed crack length $l=l_0$, and Δt is the duration of the first step (A-A' in Fig. 6.1). Similarly, k_{11} can be evaluated by measuring the duration of stage B-C in Fig. 6.1. Because in this case the process zone is formed simultaneously with crack initiation, Eqs. (6.8) and (6.9) must be solved in order to determine k_{11}.

It can thus be seen that all necessary parameters of the model can be obtained from the first two steps of CL growth. After these parameters have been obtained, the entire process of CL growth can be predicted for arbitrary loading histories.

6.2 Computer Simulation of Crack Layer Growth

Crack Layer Stability Analysis and Computer Simulation

The instability conditions for the crack and the process zone result from thermodynamic considerations. The necessary conditions for CL instability are

$$X^{CR}=0, \; X^{PZ}=0 \tag{6.12}$$

The sufficient conditions for CL instability are

$$\frac{\partial^2 G}{\partial l^2} < 0 \quad \text{(crack instability)} \tag{6.13}$$

$$\frac{\partial^2 G}{\partial l_a^2} < 0 \quad \text{(process zone instability)} \tag{6.14}$$

$$\begin{vmatrix} \frac{\partial^2 G}{\partial l^2} & \frac{\partial^2 G}{\partial l \partial l_a} \\ \frac{\partial^2 G}{\partial l_a \partial l} & \frac{\partial^2 G}{\partial l_a^2} \end{vmatrix} < 0 \quad \text{(CL instability)} \tag{6.15}$$

As mentioned earlier crack instability leads to crack jumps, although stable crack growth is recovered after the jump. When the process zone and crack instabilities points are reached, CL evolution becomes a sequence of instant jumps of crack and process zone, resulting in ultimate failure. Figure 6.6 shows the l-l_a diagram for crack and process zone instabilities in a SEN specimen under a tension of $0.25\sigma_{tr}$.

Equations (6.12)-(6.15) give the critical values for a crack length and process zone size at the point of instability, for a given applied stress σ_∞. Using the kinetic equations, the evaluation of the time for CL growth to a point of final instability gives the total lifetime of the specimen (Fig. 6.7). Thus the kinetic equations together with the instability analysis can be used as a tool for accelerated tests.

Test of the Model

Using this model, the final lifetime for a SEN specimen was estimated for different applied stress levels and different material properties (the transformation stress and Young's modulus). The effect of the kinetic coefficients was also examined. For comparison with experimental data, the following empirical formula proposed by Huang and Brown [81] for the lifetime of SEN polyethylene specimens under creep was used:

$$t_f = k\left(\frac{\alpha}{\dot{\delta}_0}\right)^{0.89} \tag{6.16}$$

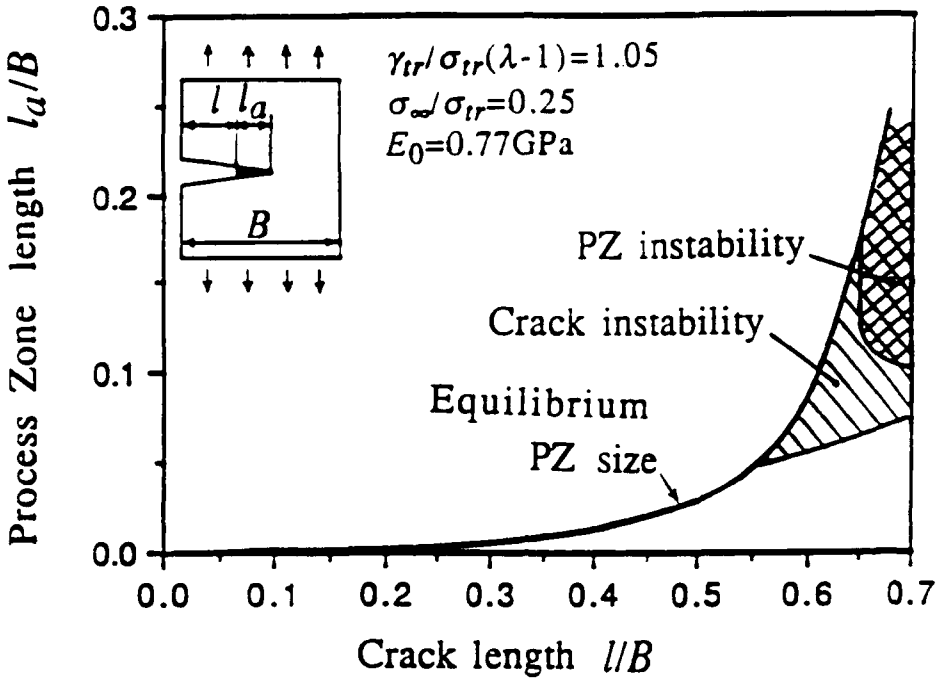

Figure 6.6 l-l_a diagram for CL stability analysis.

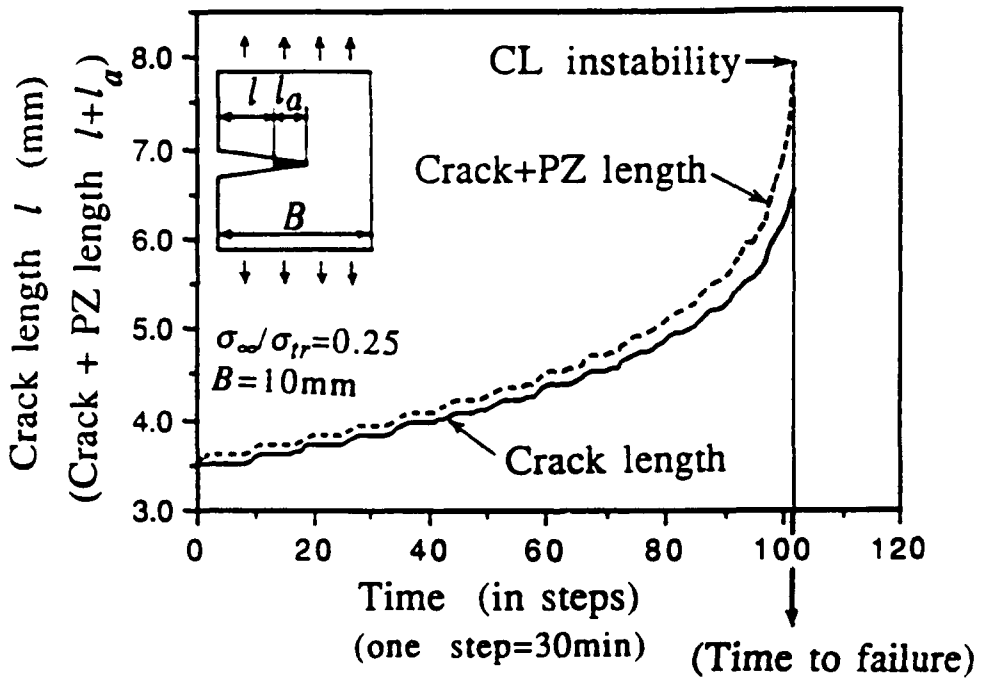

Figure 6.7 CL growth history and lifetime evaluation.

Here t_f is the time to failure, α is the angle at the tip of the process zone at the initiation stage and $\dot{\delta}_0$ is the rate of crack opening displacement at the root of the original notch at the very first stage. The power 0.89 was obtained from regression analysis of an extensive amount of experimental data for different stress levels, temperatures and so forth. The above formula suggests that the time to failure can be predicted from the initial stage of the fracture process. The parameters α and $\dot{\delta}_0$ in Eq. (6.16) are readily evaluated within our model, thereby allowing for a comparison of this model with experimental results.

Figure 6.8 plots the predictions of the model for lifetime versus $(\alpha/\dot{\delta}_0)^{0.89}$, using various stress levels and kinetic coefficients. The model reconstructs exactly the same linear relationship between t_f and $(\alpha/\dot{\delta}_0)^{0.89}$ as specified in Eq. (6.16). One can therefore feel confident that the model captures the essence of the phenomena. This model is perhaps suitable as a tool for accelerated tests.

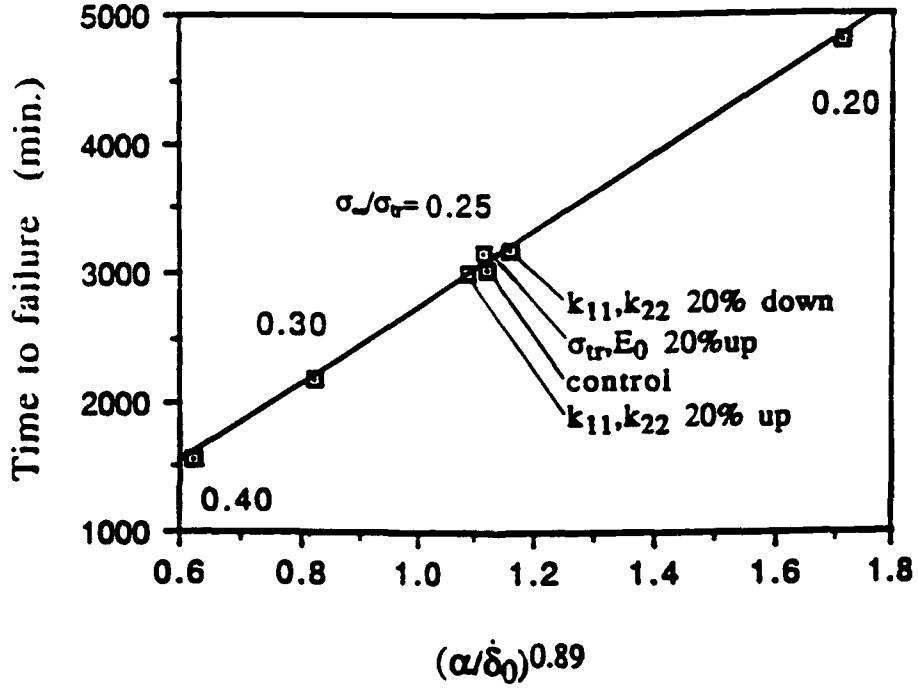

Figure 6.8 Parametric studies of the simulated lifetime versus Brown's empirical factor.

6.3 Conclusion

Constitutive equations to describe slow Crack Layer growth are proposed. This model provides a very good simulation of experimentally observed nonmonotonic crack growth in ductile polymer, and recovers Brown's empirical formula for estimating lifetimes. A methodology is suggested for evaluating the material parameters in the model. Since these parameters can be evaluated from short-term tests, this model can be used as the basis for an accelerated test procedure.

LIST OF REFERENCES

1. G. K. Haritos, J. W. Hager, A. K. Amos, M. J. Salkind and A. S. D. Wang, "Mesomechanics: the microstructire-mechanicsx connection", AIAA, 87-0726, 1987.

2. A. Chudnovsky, The Crack Layer Theory, NASA Contractor Report # 174634, 1984.

3. Huang, W.-L., Kunin, B., and Chudnovsky, A.: Kinematics of damage zone accompanying curved crack. Proc. Symp. Mechanics of Plastics and Plastics Composites, Dec., 1989, also appeared in *International Journal of Fracture*, 50: 143-152, 1991.

4. A. Chudnovsky and S. Wu (1991) "Elastic interaction of a crack with random array of microcracks," *International Journal of Fracture*, 49, p123-140.

5. A. Chudnovsky and S. Wu: "Evaluation of ERR in crack-microcracks interaction problem", Inter. J. Solids and Structure, In press.

6. A. Chudnovsky, W.L. Huang, and B. Kunin: Effect of damage on fatigue crack propagation in polystyrene. *Polymer Engineering and Science*, 30(20): 1303-1308, 1990.

7. A. Chudnovsky and S. Wu (1990) "Effect of crack-microcrack on energy release rates," *International Journal of Fracture*, 44, 43-56

8. S. Wu and A. Chudnovsky: "Effective elastic properties of a linear elastic solid with microcracks," *Engineering Fracture Mechanics*, 37(3), P653, 1990.

9. K. Kadota, A. Chudnovsky, J. Strebel and A. Moet, *Proceedings of ANTEC'91*, Montreal, Canada, 2180 (1991).

10. K. Kadota and A. Chudnovsky, *Proceedings of the ASME Winter Annual Meeting*, MD-29, 101, Dec. 1-6, (1991), Atlanta, GA.

11. A. Stojimirovic and A. Chudnovsky, submitted to *Inter. J. Fracture.*

12. A. Stojimirovic, K. Kadota, A. Chudnovsky, *J. of Applied Polymer Sci.*, to appear.

13. A. Kim, L. V. Garrett, C. P. Bosnyak and A. Chudnovsky: "Modeling of the process zone in ductile polymers", *J. Appl. Polym. Sci.*, in press.

14. A. Kim, L. V. Garrett, C. P. Bosnyak and A. Chudnovsky: "Kinetics and characterization of th process zone evolution", *J. Appl. Polym. Sci.*, in press.

15. N. Brown and S. K. Bhattacharya, *J. Mater. Sci.*, 20, 4553 (1985).

16. K. Kadota and A. Chudnovsky: Constitutive equations of crack layer growth", AMD-Vol. 132/MD-Vol. 30, *Recent Advances in Damage Mechanics and Plasticity*, ASME 1992.

17. K. Kadota, A. Stojimirovic, and A. Chudnovsky: "Modeling of the process zone in ductile polymers", *Proceedings of ANTEC'92*, Detroit, Michigan, pp. 1219-1222.

18. K. Amkee PAN 1993.

19. P. C. Paris and F. Erdogan, *Trans. ASME* 85, 528 (1963).

20. E. P. Tam and G. C. Martin, *J. Macromol. Sci.-Phys.* B23 (4-6),415 (1984-1985).

21. J. Botsis, A. Chudnovsky and A. Moet, *Int. J. Fracture*, 33, 263 (1987).

22. A. A. Rubinstein, *Mechanics of the Crack Path Formation*, NASA Contractor Report #185143, Sep., 1989 (also appeared in *Int. J. Fracture*, 47: 291-305, 1991.)

23. V. L. Tamuz and A. Z. Lachzdenye, *A Phenomenologyical Theory of Fracture Mechanics of Polymer 9 (1968).*

24. Botsis, J. (1988) "Damage analysis of a crack layer'" *Polymer*, Vol. 29, 457-462.

25. A. Chudnovsky and M. Bessendorf, in *Proceeding cf ICF6*, New Delhi, India (1984) 1663-1670.

26. A, Chudnovsku, I. Palley, and E. Baer, *J. Mater. Sci.*, 16 (1981), 35-44.

27. Botsis, J. and Kunin, B. (1987) "On self-similarity of crack layer", *International Journal of Fracture*, 35, R51.

28. Zhang, X. Q., Ph.D thesis, University of Illinois at Chicago, 1991.

29. Lesser, A., Ph.D thesis, CWRU, 1989.

30. Steif, P. S. (1987) "A semi-infinite crack partially penetrating on circular inclusion," *Journal of Applied Mechanics*, Vol.54, pp. 87-92.

31. Ortiz, M. (1987) "A continuum theory of crack shielding in ceramics," *Journal of Applied Mechanics*, Vol.54, pp. 54-58.

32. Huchinson, J. W. (1987), "Crack tip shielding by micro-cracking in brittle solids," *ATCA Metall.* Vol.35, pp.1605-1619.

33. Wu, C. H. (1988) "A semi-infinity crack penetrating an inclusion,"*Journal of Applied Mechanics*, Vol.55, p736-738.

34. Chudnovsky, A. and Kachanov, M.(1983) "Interaction of a crack with a field of microcracks,"*Letter in Applied Engineering Science*, 21, pp. 1009-1018.

35. Horii, H. and Nemat-Nasser, S. (1983) "Estimates of stress intensity factor for interacting cracks," *Advance in Aerospace Structure, Materials and Dynamics*, (Edited by U. Yuceoglu, R.L. Sierakowski and D.A. Glasgow), ASME, pp.111-117.

36. Kachanov, M. (1985) "A simple technique of stress analysis in elastic solids with many cracks," *International Journal of Fracture*, Vol.28, R11-R19.

37. Rose, L.R.F. (1986) "Microcrack interaction with a main crack, "*International Journal of Fracture,* Vol.31, pp.233-242.

38. Rubinstein, A. A. (1986) "Macrocrack-microdefect interaction," *Journal of Applied Mechanics*, Vol.53, pp.505-510.

39. Chudnovsky, A., Dolgopolsky, A. and Kachanov, M. (1987) "Elastic interaction of a crack with microcracks," *International Journal of Solid and Structures*, Vol.23, 1-21.

40. Chudnovsky, A. and Qoezdou, B. (1988) "Semi-impirical crack tip analysis," *International Journal of Fracture*. Vol.37, 3-11.

41. Wu, S. and A. Chudnovsky, has been submitted to International Journal of Fracture.

42. Ballarini, R. and Denda, M. (1988) "The interaction between a crack and a dislocation dipole," *International Journal of Fracture*, Vol. 31, 61-71.

43. Eshelby, J. D. (1956) *in Prog. Solid State Physics* (ed. F. Steitz and D. Turnbull) Vol.3, p79. Academic Press, New York.

44. Eshelby, J. D. (1975) "Energy momentum tensor," *Journal of Elasticity*, Vol. 5, No. 3-4, pp. 321-335.

45. Tada, H. (1973) Handbook of the stress analysis of cracks, Del Research Corporation, Hellertown, Pennsylvania.

46. B. Hashin, *Journal of Applied Mechanics*, Vol. 50, (1983), 481-505.

47. E. Montagut and M. Kachanov, "On modelling a microcracked zone by weakened elastic material", *Inter. J. Fracture*, Vol. 37, R55-R62, (1988).

48. A. A. Rubinstein and H. C. Choi, "Macrocrack interaction with transverse array of microcracks", *Inter J. Fracture*, Vol. 36, (1988), pp.15-26.

49. M. Kachanov, Inter. *J. Solids and Structure*, Vol. 23, No. 1, (1987) pp.23-43

50. Y. Murakami, Stress intensity factors handbook, Vol. 1, Pergamon Press, (1987) p200.

51. A. Chudnovsky, and B. Kunin, Private Communication.

52. E. J. Kramer, "Microscopic and molecular fundamentals of crazing," in Advances in Polymer Science, edt. H. H. Kausch, Springer-Verlags, Berlin (1983).

53. K. Chaoui, A. Chudnovsky and A. Moet, *J. Mater. Sci.*, 22, 3873 (1987).

54. X. Lu and N. Brown, *J. Mater. Sci.*, 21, 4081 (1986).

55. X. Wang and N. Brown, *Polymer*, 30, 1456 (1989).

56. Y. Zhou, Y. Huang, X. Lu and N. Brown, *Plastic Fuel Gas Pipe Symposium Proceedings*, (1989), San Francisco, CA.

57. K. Sehanobish, A. Moet, A. Chudnovsky and P. P. Petro, *J. Mater. Sci. Letters*, 4, 890 (1985).

58. J. J. Strebel, private communication (1990).

59. N. Haddaoui, A. Chudnovsky, A. Moet, *Polymer*, 27, 1377 (1986).

60. A. M. Donald, E.J. Kramer, *J. of Material Science*, 16, 2967 (1981).

61. H. Nisitani, H. Hyakutake, *Eng. Fracture Mechanics*, 22, 359 (1985).

62. K. Sehanobish, E. Baer, A. Chudnovsky and A. Moet, *J. Mater. Sci.*, 20, 1934 (1985).

63. M. Ma, K. Vijayan, A. Hiltner, E. Baer, *J. of Mater. Sci.*, 24, 2687 (1989).

64. R. N. Haward, *Physics of Glassy Polymers* (1976).

65. J. W. Maher, R.N. Haward, J. N. Hay, *J. of Polymer Sci.*, 18, 2169 (1980).

66. G. Buisson, K. Ravi-Chandar, *Polymer*, 31, 2071 (1990).

67. J. Grenet, C. G'sell, *Polymer*, 31, 2057 (1990).

68. S. N. Zhurkov, *Int. J. Fracture*, 1, 311 (1965).

69. A. G. Atkins, C.S. Lee, R.M. Caddell, *J. of Mater. Sci.* 10 1381 (1975).

70. M. A. Kirloskar and J.A. Donovan, *Polymer Eng. and Sci.*, 27 (1987) 124.

71. M. K. V. Chan and J. G. Williams, *Polymer*, 24, 234 (1983).

72 A. Lustiger and R. D. Corneliussen, *J. Mater. Sci.*, 22, 2470 (1987).

73. M. L. Kasakevich, A. Moet and A. Chudnovsky, *Polymer*, 31, 435, (1990).

74. P. E. Kanninen, P. E. O'Donoghue, C. H. Popelar and V. H. Kenner, *Engineering Fracture Mechanics.*, 36, 903, (1990).

75. X. Lu, R. Qian and N. Brown, *J. Mater. Sci.*, 26, 917, (1991).

76. P. T. Reynolds and C. C. Lawrence, *J. Mater. Sci.*, 26, 6197, (1991).

77. J. J. Strebel and A. Moet, *J. Mater. Sci.*, 26, 5671, (1991).

78. A. J. Kinloch and J. G. Williams, *J. Mater. Sci.*, 15, 987, (1980).

79. R. Schirrer, J. Le Masson, B. Tomatis and R. Lang, *Polymer Engi. Sci.*, 24, 820, (1984).

80. T. J. Chen, University of Illinois at Chicago, Department of Civil Engineering, Mechanics and Metallurgy (private communication).

81. Y. Huang and N. Brown, *J. Polymer Sci. Part B: Polymer Phys. Ed.*, 28, 2007 (1990).

82. Botsis, J.: Damage analysis of a crack layer. *Journal of Materials Science*, 24: 2018-2024, 1989.

83. Holik, S. A., Kambour, R. P., Fink, D. G., and Hobbs, S. Y., *Microstructural Science*, Vol. 7, LeMay, ed., Elsevier North Holand, p357, 1978.

84. J. M. Gere and S. P. Timoshenko, Mechanics of Materials, The second edition, PWS Publisher, 1984.

85. S. P. Timoshenko, Strength of Materials, Part II, Advanced Theory and Problems, Third edition, Robert E. Krieger Publishing Company, 1983.

86. M. L. Kasakevich, M. Moet, and A. Chudnovsky:"A crack layer approach to creep crack propagation in high density polyethylene'" *J. Macromol. Sci. - Phys.*, B28, 433-453, 1989.

87. M. L. Kasakevich, M. Moet, and A. Chudnovsky:"A crack layer approach to fatigue crack propagation in high density polyethylene'" *J. Applied Polymer Sci.* 39, 395-413, 1990.

88. I. Narisawa, and H. Nishimura:"Unstable cracking of medium density polyethylene," *J. Mater. Sci.*, 24, 1165-1168, 1989.

89. J. J. Strebel, V. Chellappa, and A. Moet:"Evaluation of J_{1c} for thin polyethylene specimens," *Inter. J. Fracture*, 48, R47-R50, 1991.

Appendix A

Experimental Setup and Parametric studies

A.1 Experimental Setup

Commercial polystyrene (PS) was chosen as a modelling material due to its transparency and visibility of defects. Plane isotropic PS obtained from Transilwrap Company (Cleveland, Ohio) was used in all studies. Rectangular PS sheets were cut and machined to single edge notched specimens with 80mm gauge length and 20mm width. A 60 degree V-shaped notch was milled into the edge to 1mm depth at the midspan of the gauge length. An internal circular hole was drilled, and the location and diameter of the hole vary in different tests.

Tension-tension fatigue experiments were conducted on a 1.1 ton (2.5 Kip) capacity servohydraulic Instron Testing System at room temperature. Sinusoidal waveform loading was employed in all tests. Figure A.1 shows the specimen geometry and the loading configuration. The damage evolution and crack propagation were observed and recorded using the Hamamatsu video system attached to a Quester long range travelling microscope.

After testing, specimens were photographed through the Zeiss optical microscope for the sideview (with transmitted light) and fracture surface (with reflected light) analysis. Then specimens were polished to a thickness of 20-30μm in order to make the micrographs for craze density and orientation analysis.

Botsis [87] has shown that during rectilinear crack layer propagation in PS, crazing is uniformly distributed in the thickness direction. Therefore, sections parallel to the plane of the specimen adequately represent craze distribution within an active zone. Accordingly, damage is characterized as the area of craze middle plane per unit volume, ρ (mm^2/mm^3).

The assembled micrographs of AZ is covered by a square grid, the squares being at least one order of magnitude smaller than the linear dimension of the AZ. In each square, the number of intersections of the crazes with a vertical test line is counted. Then the craze density ρ at each cell is calculated by

$$\rho = \frac{n a t}{a^2 t}$$

where ρ (mm^2/mm^3) represents the amount of area of craze middle planes per unit volume, n is the number of intersections of crazes with a vertical test line at each square, a is the size of the cell, and t is the specimen thickness. The orientation of craze is measured with respect to a horizontal line which is parallel to the tangent direction of the crack trajectory at the crack tip.

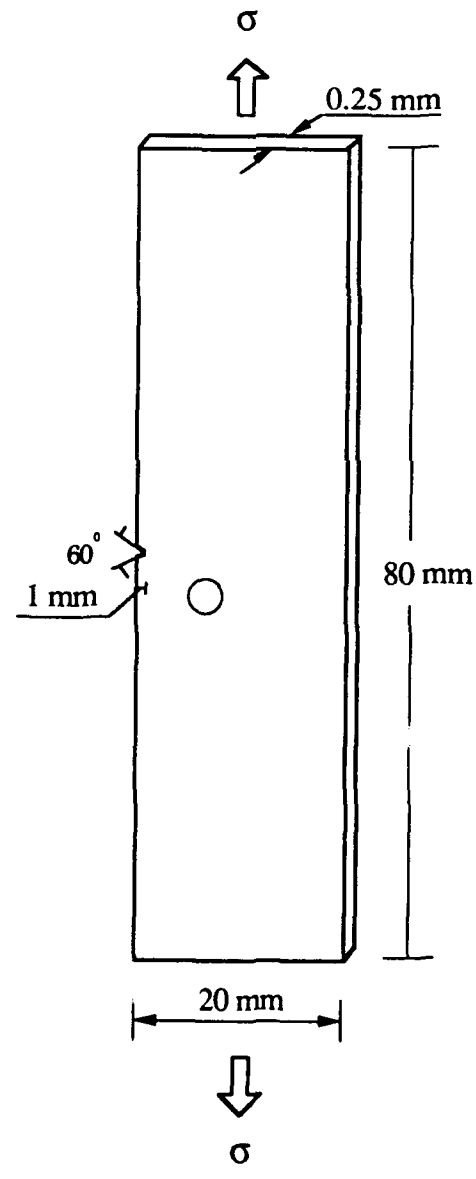

Figure A.1 Experimental setup

Standard metallographic and polishing techniques [88] were used to section the specimen in the direction perpendicular to the fracture surface. A typical micrograph of a polished section of an AZ is shown in Fig. A.2. From these micrographs, the distribution of craze density and orientation within the AZ are obtained by the following procedures.

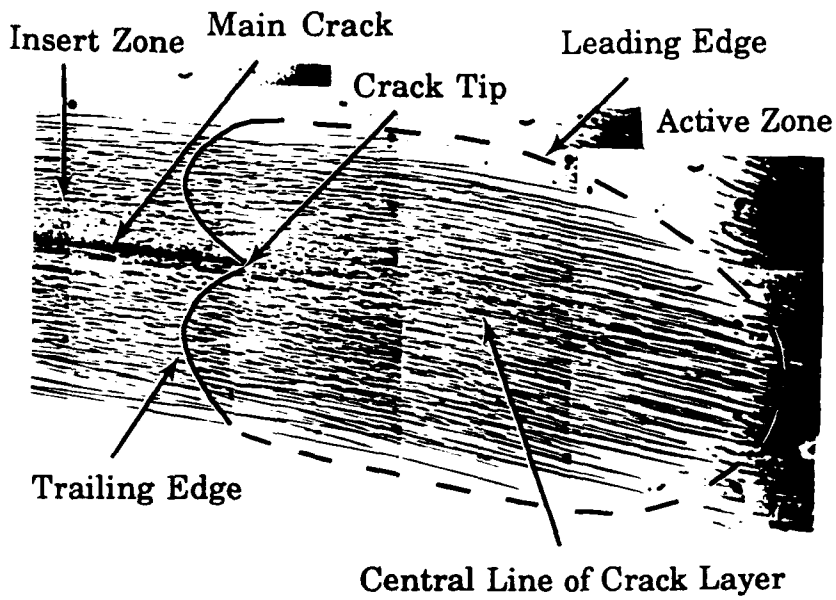

Figure A.2 A schematics of the Active Zone

A.2 Parametric Studies

In this section, the effect of three geometrical parameters on the CL configuration is studied. The parameters are the hole radius, ϕ, and the hole center coordinates: a and h. "a" is the horizontal distance from the hole center to the notched edge and h is the vertical distance from the hole center to the reference line. Figure A.3 shows the geometrical parameters used in this study. The reference line is the potential rectilinear crack trajectory under a symmetric specimen-loading configuration.

The reason to introduce a hole inside the SEN specimen is that we want the crack to experience the most complex stress condition similar to the real situation. This is usually neglected in most research works about crack propagation. Due to the presence of a hole, there are stress concentrations at the hole edge such that the stress field near the hole area is extremely heterogeneous. The mixed mode effect of K_I and K_{II} is clearly shown in the CL evolution.

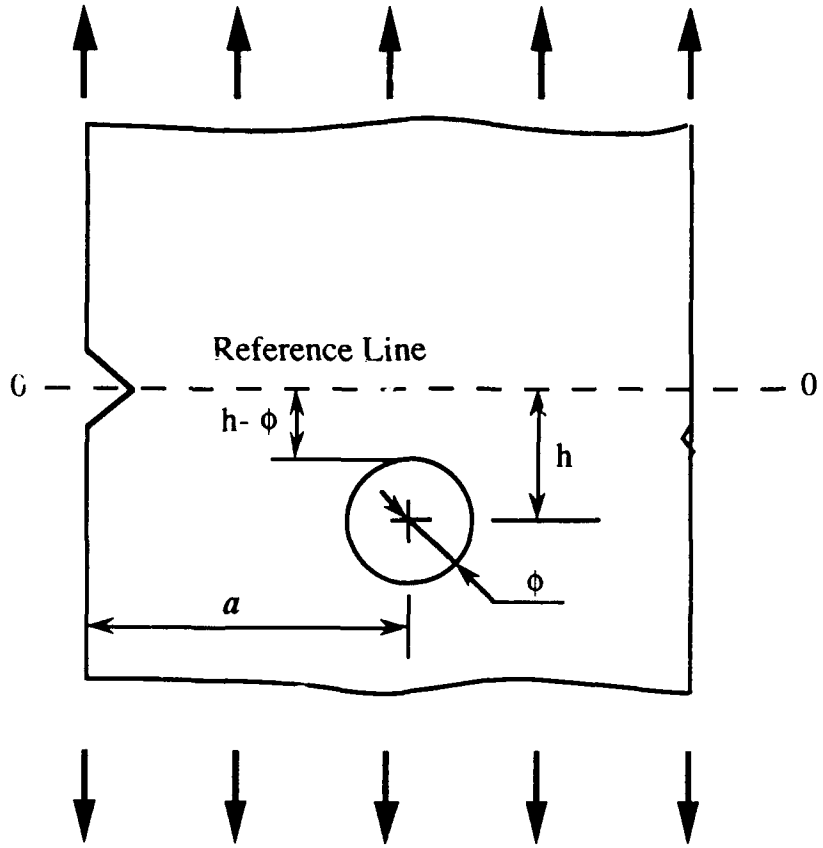

Figure A.3 Parameters of specimen geometry

Experimental Conditions

The following five cases are considered in this study:

(i) h varies; a and ϕ are constants;

(ii) ϕ varies; a and $h-\phi$ are constants;

(iii) h, ϕ, and a vary under the constraint that $h=2\phi$ and a/ϕ is constant;

(iv) a varies; h and ϕ are constants as well as the remotely applied stress;

(v) a varies; h and ϕ are constant and the remotely applied stress is adjusted so that the potential energy of a straight crack of length a remains constant.

Experimental Results

The following format is used to present general observations for each type of the parametric studies.

A. "Crack Trajectory Geometry": Observations concerning the shape of the main crack are shown (its deviation from the reference line, its curvature, etc.).

B. "CL Geometry": Observations concerning the shape of the crack layer are presented (the curvature of the CL central line versus the main crack's curvature, CL width, craze orientation, etc.).

C. "CL Kinetics": Qualitative observations concerning the evolution of both the main crack and the CL are presented (speed of main crack, craze orientation, etc.).

Additional geometrical parameters are introduced in Fig. A.4 for future reference. In this figure, ξ_C and ξ_{CL} represent the difference between the abscissas of the hole center and the depth of the peak of the curvature of the crack trajectory and CL central line, respectively.

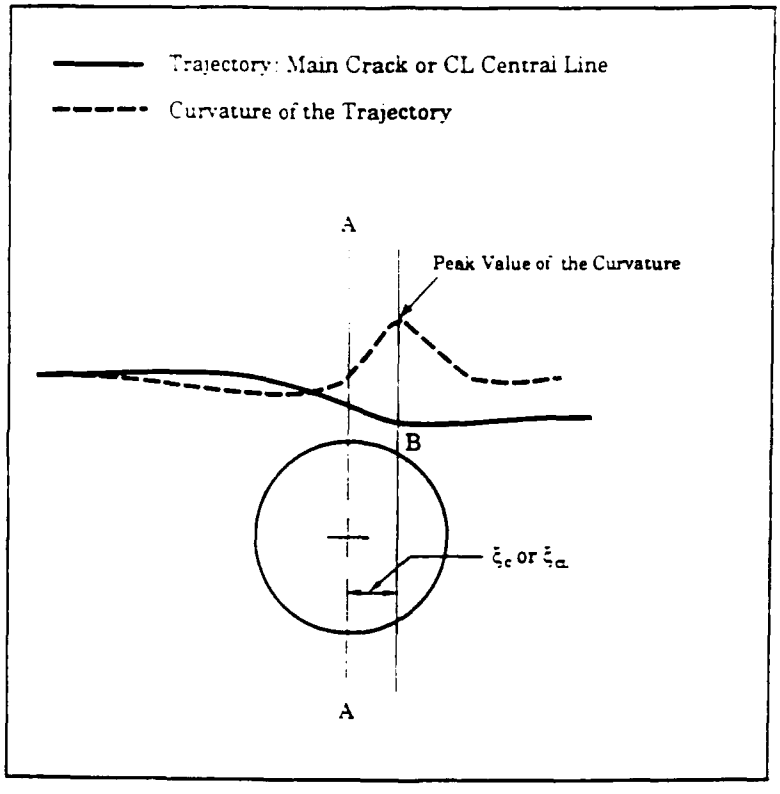

Figure A.4 Additional geometrical parameters

Case (i): Crack Layer Propagation for Various h and Constant ϕ and a

Loading conditions: σ_{max} = 15.0 MPa, σ_{min} = 1.5 MPa

Frequency: 0.5 Hz

Geometry: (1) a = 6.0 mm, ϕ = 1.5 mm, h=2.5 mm
(2) a = 6.0 mm, ϕ = 1.5 mm, h=3.5 mm
(3) a = 6.0 mm, ϕ = 1.5 mm, h=4.5 mm

Number of tests: geometry (1) – 1, geometry (2) – 2, geometry (3) – 2

A. Crack Trajectory Geometry:

The curvature of the crack trajectory is strongly affected by the distance h (Fig. A.5). Figure A.6 shows the corresponding curvatures of crack trajectories. Both figures indicate that the effect of the hole tends to disappear as h becomes larger than 3ϕ

B. CL Geometry:

The comparison of the main crack curvature with the CL curvature (Fig. A.7) indicates that the array of crazes turns first and the main crack follows. To evaluate "CL curvature", we use the geometrical central line of the CL instead of the line formed by gravity centers of the CL cross-sections. However, the conclusion that AZ guides the main crack is supported by the direct observations of the AZ morphology. Intense crazing within AZ appears as a response to the stress concentration at the crack tip. On the other hand, AZ extends ahead of the main crack. Therefore, the crazes at the AZ leading edge "sense" the changes in the stress field earlier than the main crack. As a result, the AZ changes direction prior to the main crack. The peak of the curvature of CL central line occurs at a shorter depth than the peak of the main crack, i.e., $\xi_{CL} < \xi_C$. Notice the apparent oscillation of the CL curvature relative to the main crack curvature, as if the AZ guides the main crack with a strong feedback.

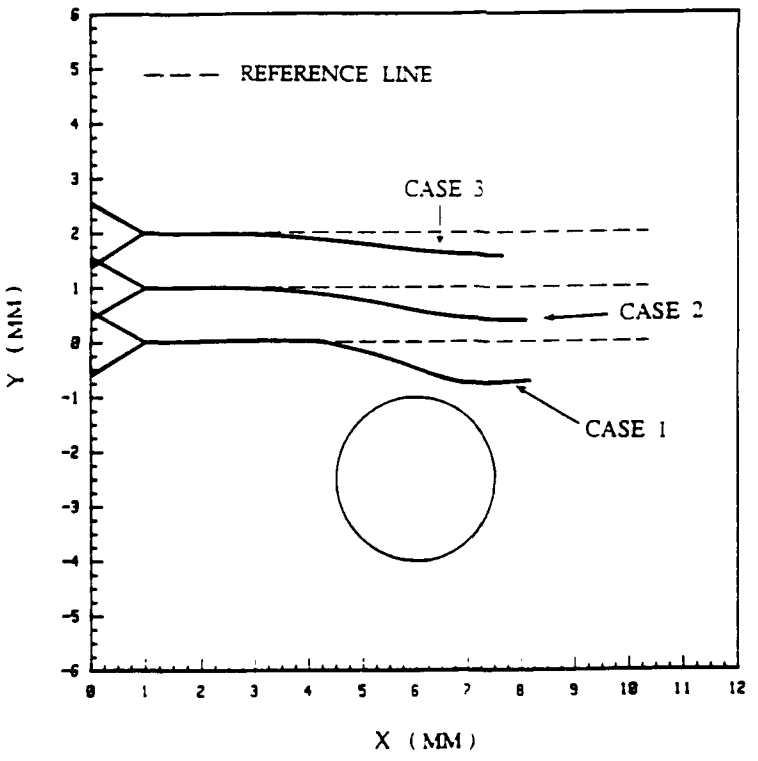

Figure A.5 Trajectories of main cracks for three notch positions

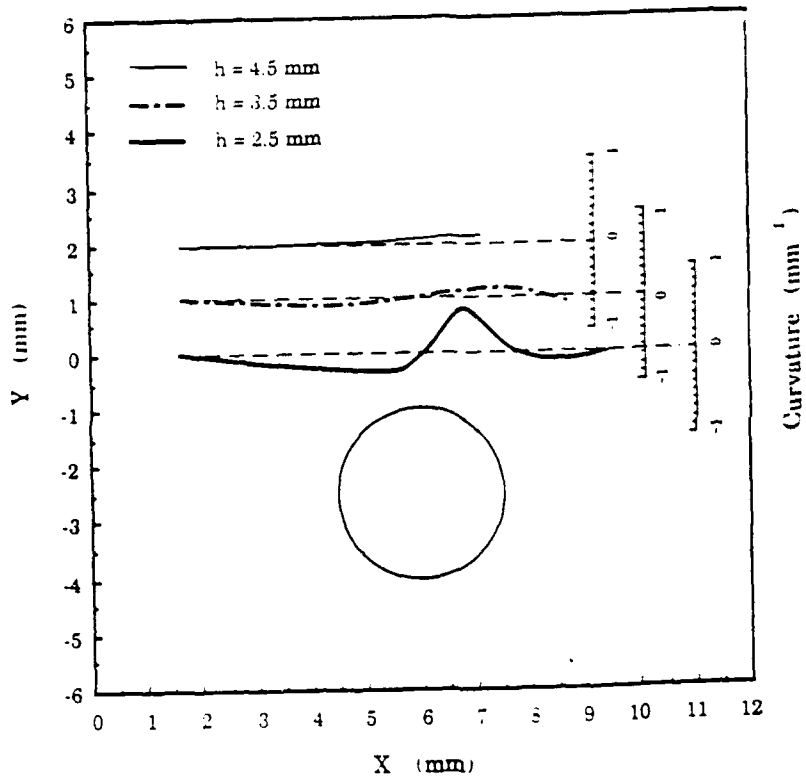

Figure A.6 Curvature of three crack trajectories

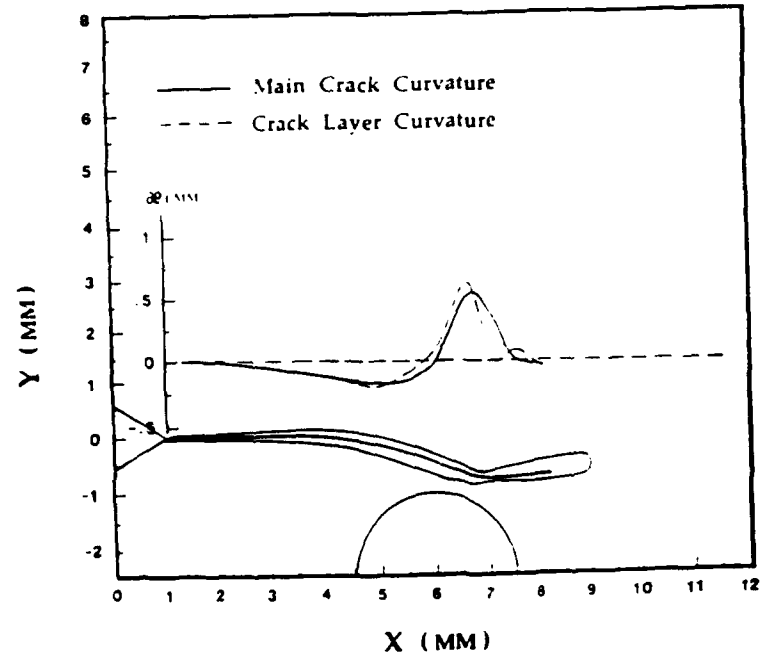

Figure A.7 The curvatures of the crack trajectory and the middle line of the CL together with the CL envelope for Case 1 in Fig. A.5.

C. CL Kinetics:

The width of CL evolves with CL propagation. During the period when CL is turning toward the hole, the lower part of CL is wider than the upper part. Once the tip of the active zone reaches the vertical axis A-A (Fig. A.4), CL propagation speed suddenly decreases and CL starts to move away from the hole. At the same time, the width of the lower part of CL begins to decrease and the width of the upper part begins to increase.

The morphology of CL at this stage for $h = 2.5\,mm$ shows "feather-like" crazes (Fig. A.8). The common phenomenon is that, within one test, the size of the active zone correlates with the crack speed, that is, the larger the active zone is, the higher the crack speed. Apparently, this holds for both rectilinear and curved CL propagation.

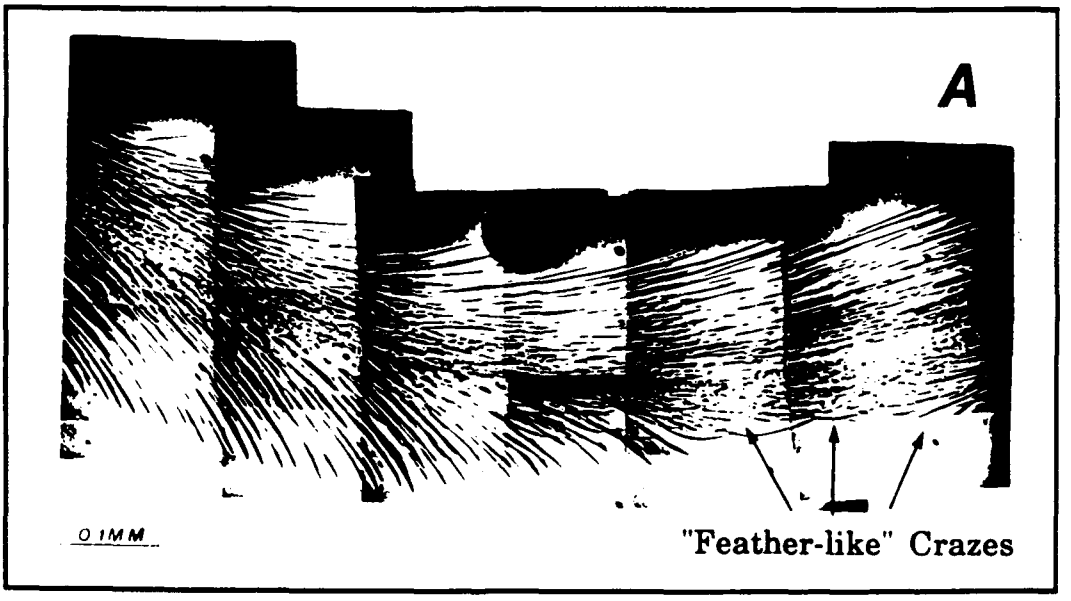

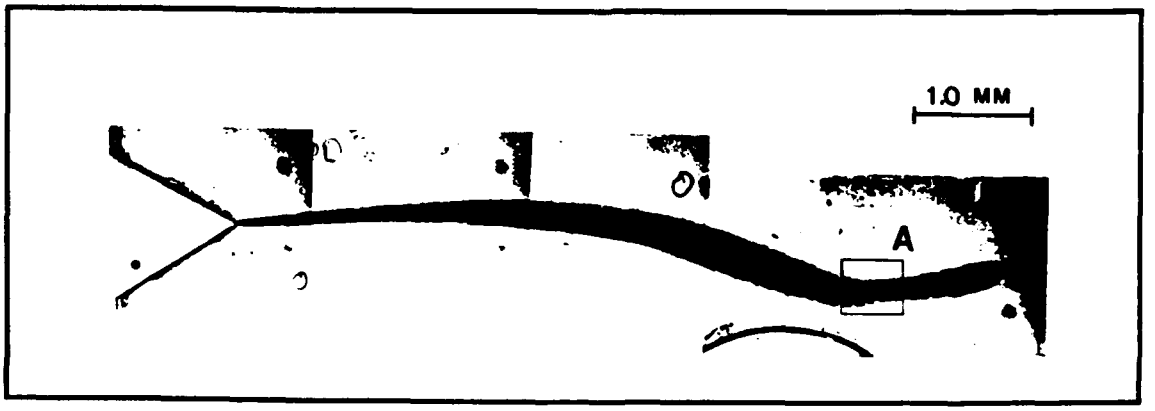

Figure A.8 "Feather-like" crazes are found where the main crack starts to turn away from the hole.

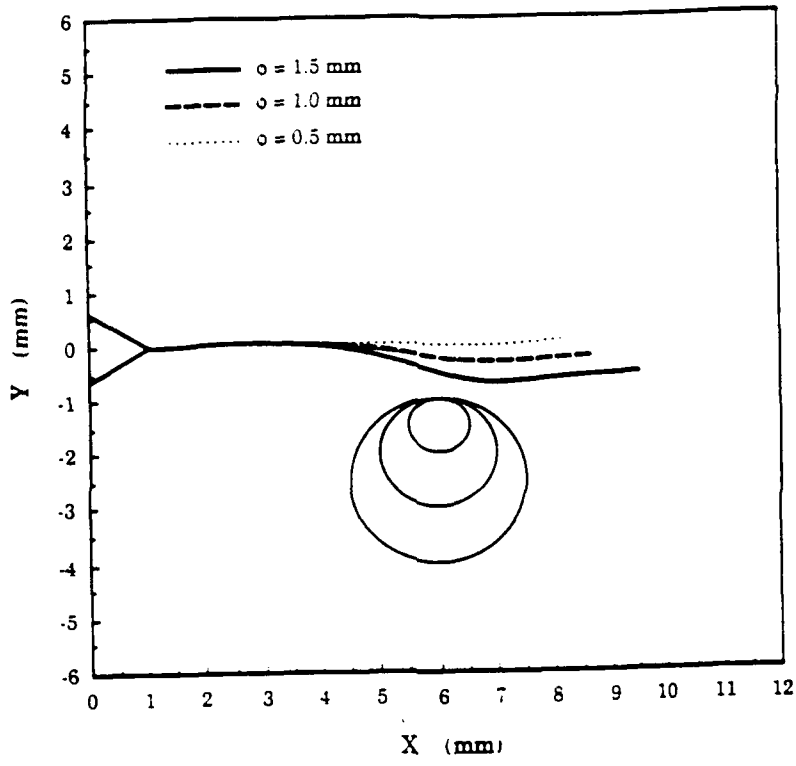

Figure A.9 Trajectories of main cracks in three specimens with different holes.

Crack Layer Propagation for Various h, and ϕ and a under the Constrain that h=2ϕ and a/ϕ is Constant

Loading conditions: σ_{max} = 17.0 MPa, σ_{min} = 1.7 MPa

Frequency: 0.65 Hz

Geometry: (1) a/ϕ = 6, a = 3.0 mm, ϕ = 0.5 mm, h = 1.0 mm

(2) a/ϕ = 6, a = 6.0 mm, ϕ = 1.0 mm, h = 2.0 mm

Number of tests: geometry (1) – 2, geometry (2) – 3

A. Crack Trajectory Geometry

In all of the tests, the crack is arrested at the hole approximately one-half radius beyond the hole center (Figs. A.10, A.11, and point B in Fig. A.4). The main crack curvature of the small-hole specimen is similar to the main crack curvature of the large-hole specimen at the "corresponding" depth. By "corresponding", in this case, we mean "twice as large", since the essential parameters a, h, and ϕ for a large-hole specimen are two times larger than those for the small-hole specimen. Figure A.12 shows a twice enlarged portion of the

small-hole specimen. Then the curvature behavior of both cases is clearly seen by comparing Figs. A.11 and A.12.

B. CL Geometry

The CL width w for specimens with the smaller hole compares to the CL width W at the corresponding depth for specimens with the large hole. For small crack length ($L \leq a/2$). $W \approx 2w$; at later stages ($L \sim a$), $W \approx 3w$ (the CL widths are measured in the direction which is locally perpendicular to the direction of the main crack trajectory).

Cases (iv) & (v): Crack Layer Propagation for Various a and Constant h and ϕ

Loading Conditions:

(a) $\sigma_{max} = 17.7$ MPa, $\sigma_{min} = 4.43$ MPa

(b) $\sigma_{max} = 13.4$ MPa, $\sigma_{min} = 3.35$ MPa

Frequency: 1.0 Hz

Geometry: (1) $\phi = 0.5$ mm, h=1.0 mm, $a = 4.0$ mm

(2) $\phi = 0.5$ mm, h=1.0 mm, $a = 5.0$ mm

Number of tests: geometry (1) under loading condition (a) – 3
geometry (2) under loading condition (a) – 2
geometry (2) under loading condition (b) – 2

Specimens of another thickness (0.17 mm) were used in all of the tests of Cases (iv) and (v) (the thickness was 0.25 mm in cases (i)-(iii)).

Case (iv): Same remote stress

Under the same loading conditions, specimens with the hole farther from the notched edge (a=5.0 mm) exhibit wider CL and more pronounced curvature change of the main crack (Fig. A.13).

Note: For specimens of the same geometry, higher stress caused wider CL and more pronounced curvature of the main crack (Fig. A.14).

Case (v): The same potential energy value (for a straight crack) at depth a

The main crack curvature pattern of (a=4.0 mm)-specimens subjected to half of failure stress (0.5 σ_f) and (a=5.0 mm)-specimens subjected to 0.38 σ_f (to have approximately the same potential energy at depth a) are very similar (Fig. A.15).

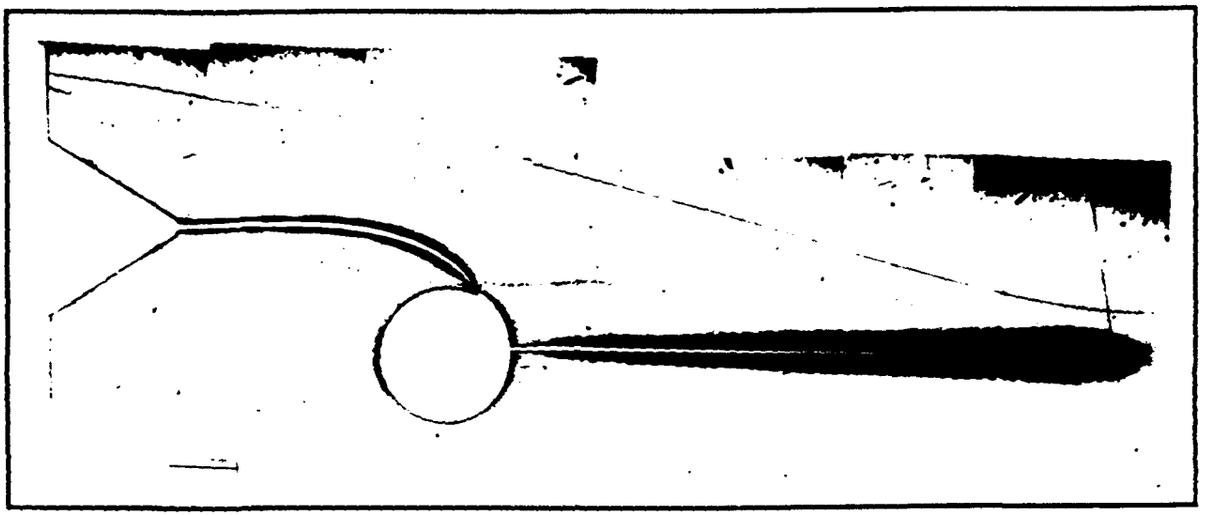

Figure A.10 Crack Layer geometry for a test with a 1 mm diameter hole

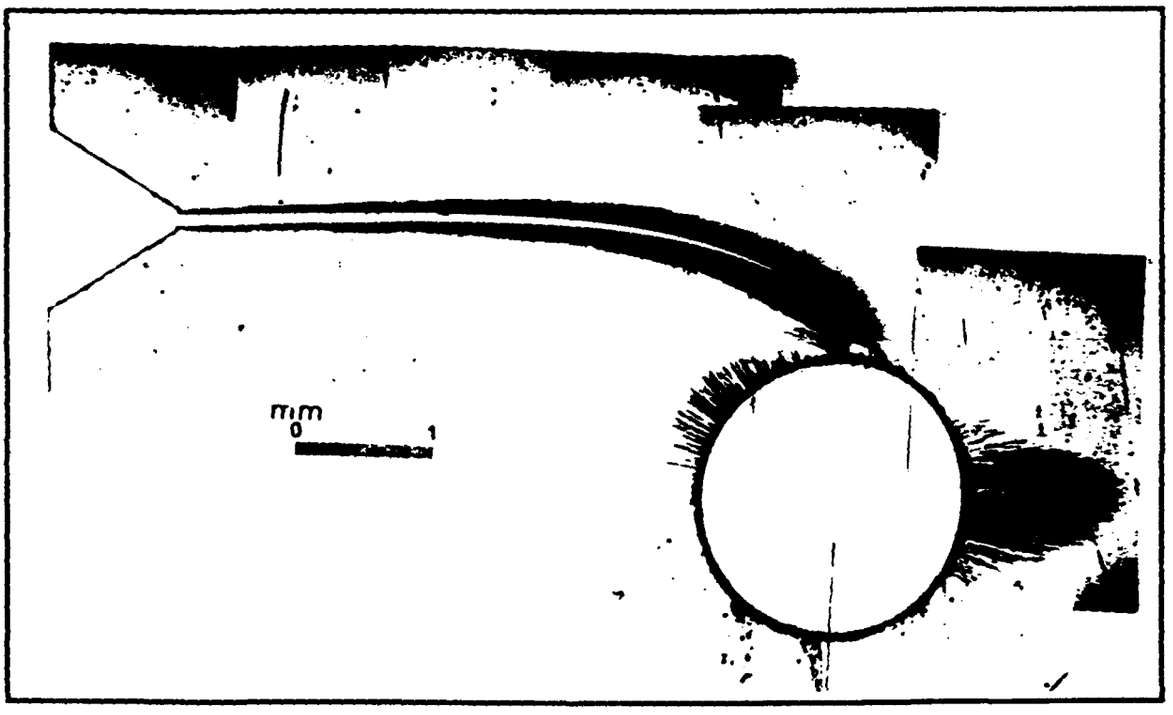

Figure A.11 Crack Layer geometry for a test with a 2 mm diameter hole

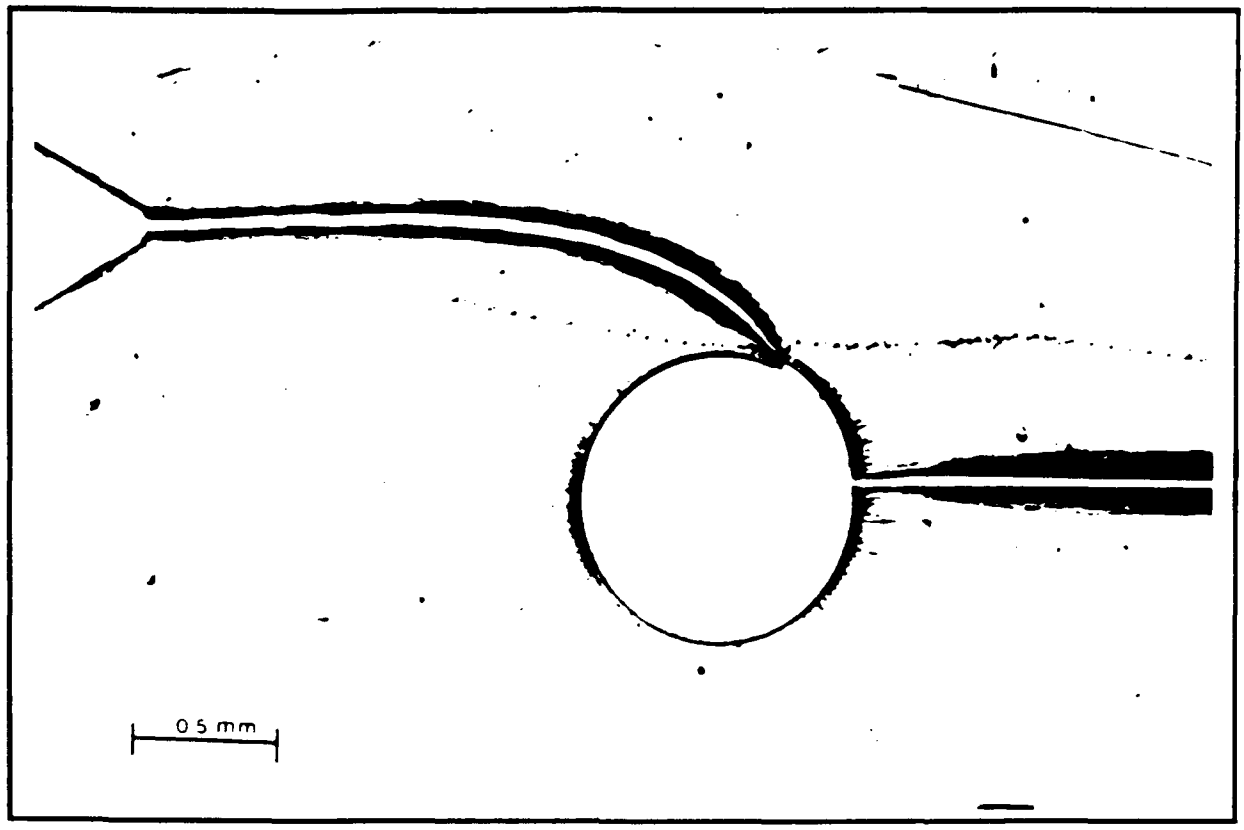

Figure A.12 Twice enlarged portion of Crack Layer geometry from Figure A.10

Summary of the Parametric Studies

As we mentioned in the previous section, the curvature patterns are very similar for 2 conditions of Case (v). An immediate check for this is to compare the normalized curvatures for specimens with the same geometry but different loading conditions at Case (iv). Normalizing the curvature by the stress intensity factor (SIF, $\sigma\sqrt{a}$) for the cases shown in Fig. A.14, we found the normalized curvatures to be almost identical for (a=5.0 mm)-specimen and (a=4.0 mm)-specimen. It can be seen by enlarging Fig. A.14 (a) 1.32 times, then comparing it to Fig. A.14 (b). The factor 1.32 is the ratio of the maximum SIF for these two cases. However, the CL width is different in these two cases even though the curvature appears to be the same.

In terms of the scaling effect, the study of Case (iii) indicates that the scaling of linear elasticity works well for the macroscopic quantity such as the main crack curvature but is not applicable for the microscopic quantity such as CL width, asymmetry, etc. (Figs. A.11 and A.12).

As to other geometrical factors, we also try to normalize the curvatures with the ratio of h/ϕ, but the results are not consistent for all five cases. We find that the main source of this is the CL width. Also, in section 2.1, we have shown that the AZ guides the main crack. This phenomenon is actually observed in all the tests. Rubinstein [4] made an attempt to explain the curved crack trajectory by means of the conventional criteria for crack direction such as maximum K_I, maximum G_1, and $K_{II}=0$. He found that none of these criteria is applicable, i.e., gives the correct direction. It is obvious that the damage zone in front of the main crack plays an important role in the crack propagation rate and direction. Therefore, the detailed analysis of the CL is necessary to understand the CL kinetics and the crack direction.

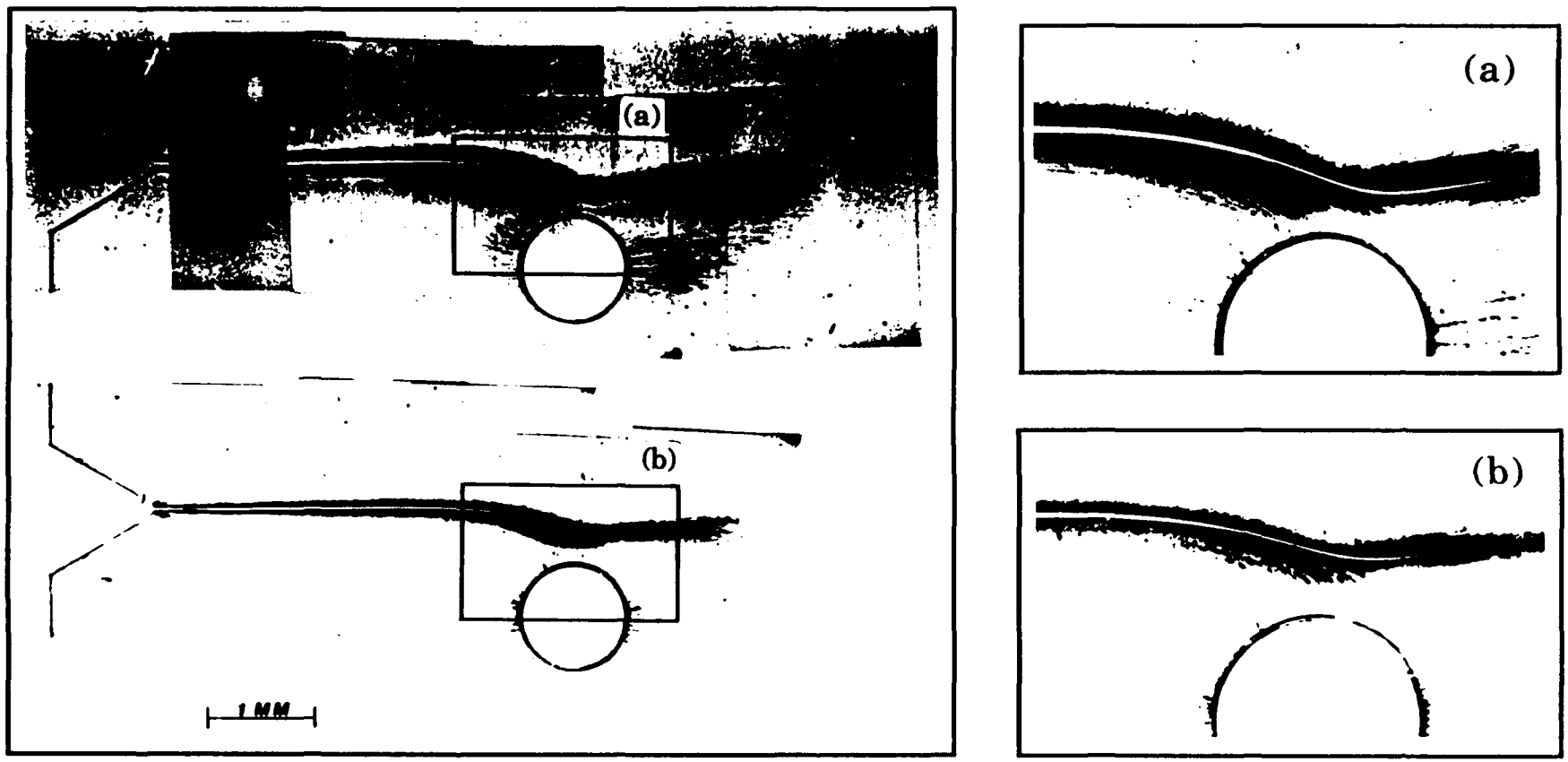

Figure 2.13 CL geometry in identical specimens under different loading conditions. (a) and (b) are the enlarged portions of the specimens under σ_{max} = 17.0 MPa and σ_{max} = 13.4 MPa, respectively.

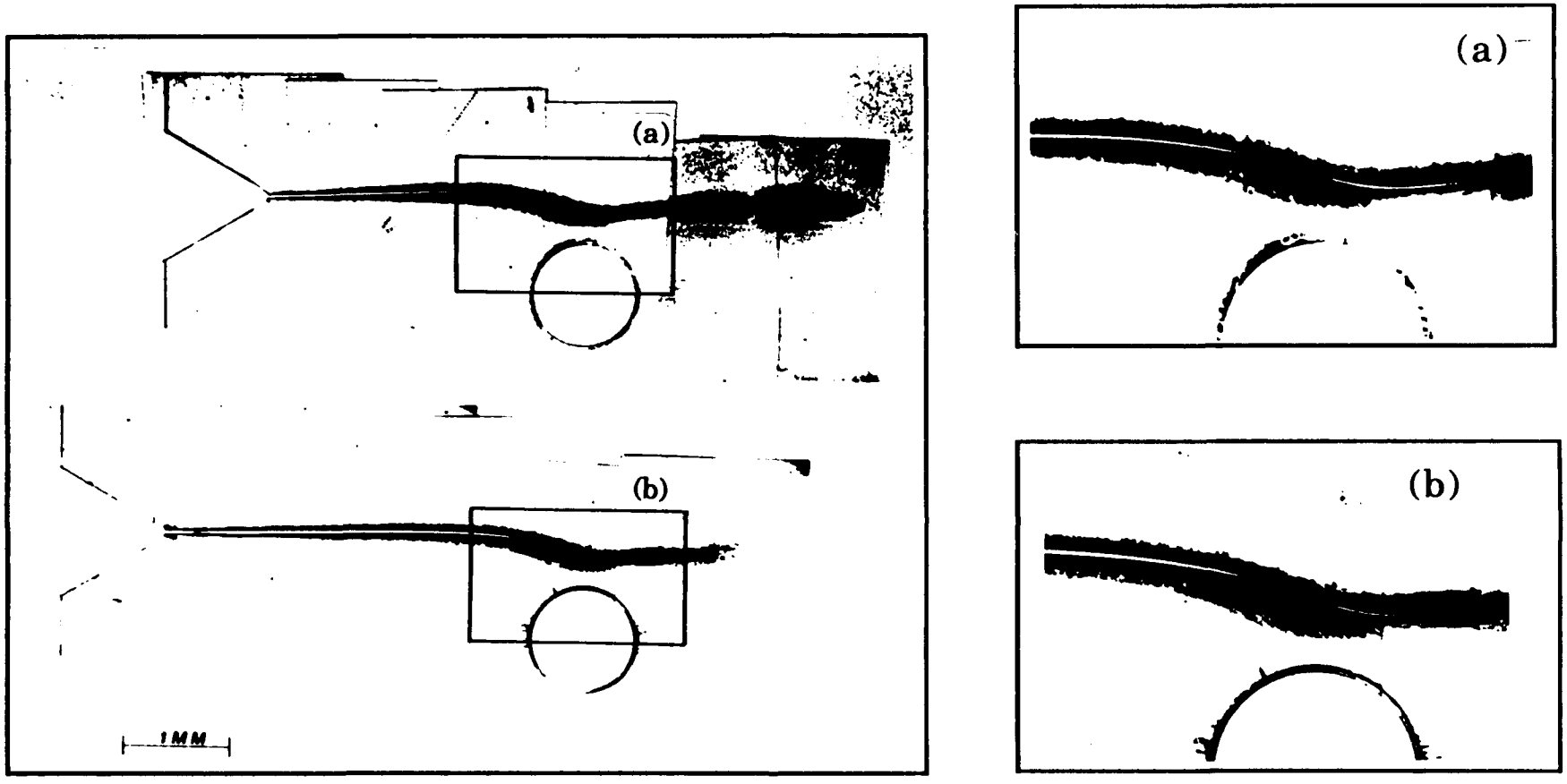

Figure 2.14 CL geometry in different specimens with identical ERR for the unperturbed crack trajectories above the hole center. (a) and (b) are the enlarged portions of the specimens with $a = 4.0\,\text{mm}$ and $a = 5.0\,\text{mm}$, respectively.

Appendix B The Simple Model for Evaluation of Opening

From the representative volume element for the high density cracks in Fig. B.1b and considering the conditions $\ell/a<\ell$, $a/h>>1$, the element in Fig. B.1b is represented by simple beam model (for 2-D case) as shown in Fig. B.1.

The deflection of beam can be found in [90] for simple support beam (Fig. B.1a)

$$v = \frac{P(\ell - c)}{6EI}[6(x+\ell)/\ell - 3(x+\ell)^2 - (\ell - c)^2] \qquad -c < x < 0$$

$$v = \frac{P(x+\ell)}{6EI}[6(\ell - c)/\ell - 3(\ell - c)^2 - (x+\ell)^2] \qquad -\ell < x < -c \tag{B1}$$

for built in beam (Fig. B.1b):

$$v = \frac{P(\ell - c)^2}{6EI}[-(\ell - c) + 3(x+\ell) - 3(x+\ell)^2/2\ell] \qquad -c < x < 0$$

$$v = \frac{P(x+\ell)^2}{6EI}[-(x+\ell) + 3(\ell - c)(\ell + c)/2\ell] \qquad -\ell < x < -c \tag{B2}$$

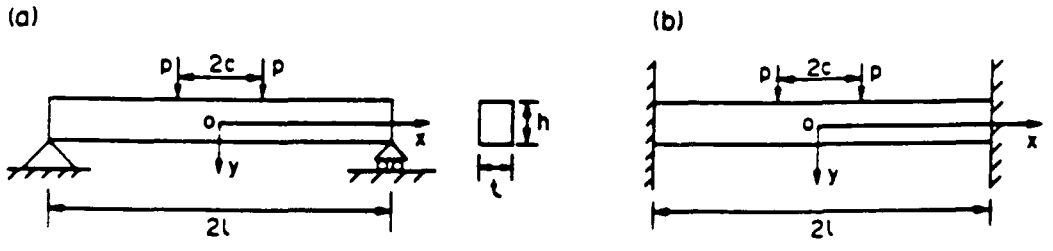

Figure B.1 The sketch of simple beam model. (a). simple support beam. (b). build in beam.

The deflection of a circular plate concentrically load can be found in [91] for simple support plate.

$$w = \frac{12(1-\nu^2)P}{8\pi Eh^3}\left[-(x^2+c^2)\ln\frac{\ell}{c} + (x^2-c^2) + \frac{(3+\nu)\ell^2-(1-\nu)c^2}{2(1+\nu)\ell^2}(\ell^2-x^2)\right] \qquad 0<x<c$$

$$w = \frac{12(1-\nu^2)P}{8\pi Eh^3}\left[-(x^2+c^2)\ln\frac{\ell}{x} + \frac{(3+\nu)\ell^2-(1-\nu)c^2}{2(1+\nu)\ell^2}(\ell^2-x^2)\right] \qquad c<x<\ell \tag{B3}$$

for built in plate:

$$w = \frac{12(1-\nu^2)P}{8\pi Eh^3}\left[-(x^2+c^2)\ln\frac{\ell}{c} + (x^2-c^2) + \frac{1}{2}\left(1+\frac{c^2}{\ell^2}\right)(\ell^2-x^2)\right] \qquad 0<x<c$$

$$w = \frac{12(1-\nu^2)P}{8\pi Eh^3}\left[-(x^2+c^2)\ln\frac{\ell}{x} + \frac{1}{2}\left(1+\frac{c^2}{\ell^2}\right)(\ell^2-x^2)\right] \qquad c<x<\ell \tag{B4}$$

The stress distribution between the two crack tip is modeled by two concentrate load where the loading point is introduced as a "center of gravity " with respect to the normal stress.

$$x_c = \int_0^{2(a-\ell)} x\sigma_{22}\,dx \Big/ \int_0^{2(a-\ell)} \sigma_{22}\,dx, \qquad c = a-\ell-x_c \tag{B5}$$

The concentrate load P is obtained by the equilibrium of force $P = a\,t\sigma_{22}^{\infty}$ (for 3-D case, $P = 2a^2\sigma_{33}^{\infty}$).

Then the average crack opening displacement of upper and lower bounds associate to the simply supported and build in beam can be expressed as:

For 2-D case upper bound,

$$\langle b_2\rangle = \frac{1}{2\ell}\int_{-\ell}^{\ell}[u_2]\,dx = \frac{a\,t\sigma_{22}^{\infty}}{9EI\ell}(4\ell-a)\left[2\ell^3 - \ell/9(4\ell-a)^2 + 1/108(4\ell-a)^3\right] \tag{B6}$$

For 2-D case lower bound,

$$<b_2> = \frac{1}{2\ell}\int_{-\ell}^{\ell}[u_2]\,dx = \frac{a\,t\sigma_{22}^{\infty}}{27EI\ell}(4\ell-a)^2[\,1/36(4\ell-a)^2 - \ell/3(4\ell-a)+\ell^2\,] \qquad (B7)$$

For 3-D case upper bound,

$$<b_3> = \frac{1}{\pi\ell^2}\int_0^{2\pi}\int_{-\ell}^{\ell}[u_3]\,r\,dr\,d\theta$$

$$= \frac{12(1-\nu^2)a^2\sigma_{33}^{\infty}}{\pi Eh^3\ell^2}\left\{\frac{1}{16}\left[\frac{(a-\ell)^4}{81}-\ell^4\right]-\frac{\ell^2(a-\ell)^2}{36}+\frac{\ell^2}{8(1+\nu)}\left[(3+\nu)\ell^2-\frac{(1-\nu)(a-\ell)^2}{9}\right]\right\}. \qquad (B8)$$

For 3-D case lower bound,

$$<b_3> = \frac{1}{\pi\ell^2}\int_0^{2\pi}\int_{-\ell}^{\ell}[u_3]\,r\,dr\,d\theta$$

$$= \frac{12(1-\nu^2)a^2\sigma_{33}^{\infty}}{\pi Eh^3\ell^2}\left\{\frac{-1}{16}\left[\frac{-(a-\ell)^4}{81}+\ell^4\right]-\frac{\ell^2(a-\ell)^2}{36}+\frac{\ell^4}{8}\left[1+\frac{(a-\ell)^2}{9\ell^2}\right]\right\}. \qquad (B9)$$

where E and ν are Young's modulus and Poisson's ratio, I is the moment of inertia. Substitute Eqs. (B6-39) to Eqs. (3.26) and (3.27), the effective compliance in Eq. (3.22) will be obtained and the functions $\Phi_2^u(\eta)$, $\Phi_2^\ell(\eta)$, $\Phi_3^u(\eta)$, and $\Phi_3^\ell(\eta)$ can be presented as the following:

$$\Phi_2^u(\eta) = \frac{2}{3}(4\eta^{(m)}-1)[\,2(\eta^{(m)})^3 - \frac{\eta^{(m)}}{9}(4\eta^{(m)}-1)^2 + \frac{1}{108}(4\eta^{(m)}-1)^3\,] \qquad (B10)$$

$$\Phi_2^\ell(\eta) = \frac{2}{9}(4\eta^{(m)}-1)^2[\,\frac{1}{36}(4\eta^{(m)}-1)^2 - \frac{\eta^{(m)}}{3}(4\eta^{(m)}-1) + (\eta^{(m)})^2\,] \qquad (B11)$$

$$\Phi_3^u(\eta) = \frac{3(1-\nu^2)}{2}\left\{\frac{1}{16}\left[\frac{(1-4\eta^{(m)})^4}{81}-(\eta^{(m)})^4\right]-\frac{(\eta^{(m)})^2}{36}(1-\eta^{(m)})^2\right.$$

$$\left.+\frac{(\eta^{(m)})^2}{8(1+\nu)}\left[(3+\nu)(\eta^{(m)})^2-\frac{(1-\nu)(1-\eta^{(m)})^2}{9}\right]\right\} \qquad (B12)$$

$$\Phi_3^{\prime}(\eta) = \frac{3(1-\nu^2)}{2}\left\{\frac{-1}{16}\left[(\eta^{(m)})^4 - \frac{(1-\eta^{(m)})^4}{81}\right] - \frac{(\eta^{(m)})^2}{36}(1-\eta^{(m)})^2\right.$$

$$\left. + \frac{(\eta^{(m)})^4}{8}\left[1 + \frac{(\eta^{(m)})^2(1-\eta^{(m)})^2}{9}\right]\right\} \qquad \text{(B13)}$$

Appendix C Crack and Process Zone Driving Forces

The purpose of this section is to evaluate the crack driving force. Knowing the Green's function for the SIF allows us to calculate the displacement caused by the crack at any point. Reference [45] specifies the Green's function for the SIF in a SEN specimen caused by a unit dipole force F applied to the crack face as follows:

$$G^{SIF}(x,l) = \frac{2F}{\sqrt{\pi l}}\phi\left(\frac{x}{l},\frac{l}{B}\right) \tag{C-1}$$

Here l is the crack length, B is the specimen width, x is the distance from the notch edge to the point of load application and ϕ, the correction factor reflecting the specimen geometry, is

$$\phi\left(\frac{x}{l},\frac{l}{B}\right) = \frac{3.52\left(1-\frac{x}{l}\right)}{\left(1-\frac{l}{B}\right)^{\frac{3}{2}}} - \frac{4.35 - 5.28\left(\frac{x}{l}\right)}{\left(1-\frac{l}{B}\right)^{\frac{1}{2}}} + \left\{\frac{1.3 - 0.3\left(\frac{x}{l}\right)^{\frac{3}{2}}}{\sqrt{1-\left(\frac{x}{l}\right)^2}} + 0.83 - 1.76\left(\frac{x}{l}\right)\right\}\left\{1-\left(1-\frac{x}{l}\right)\frac{l}{B}\right\} \tag{C-2}$$

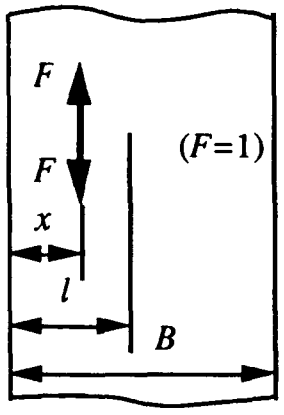

unit thickness

SEN specimen

Then the SIF from σ_{tr} applied at the interval $[l,l+l_a]$ is obtained by means of superposition (integration) as

$$K(\sigma_{tr};l+l_a) = -\sigma_{tr}\int_{l}^{l+l_a} G^{SIF}(x,l+l_a)dx \tag{C-3}$$

Similarly, the SIF from the remote applied stress σ_∞ is

$$K(\sigma_\infty;l+l_a)= \sigma_\infty \int_0^{l+l_a} G^{SIF}(x,l+l_a)dx \tag{C-4}$$

Thus the SIF for the problem in Fig. 4.2a is given by

$$K(\sigma_\infty,\sigma_{tr};l+l_a) = K(\sigma_\infty;l+l_a) + K(\sigma_{tr};l+l_a) \tag{C-5}$$

In order to calculate the potential energy for the problem in Fig. 4.12a, it is necessary to first compute the load point displacement (LPD). The LPD Δ_p can be expressed in terms of the SIF by [45]

$$\Delta_P = \Delta_{P\ no\ crack} + \frac{2}{E_0}\int_0^{l+l_a} K(\sigma_\infty,\sigma_{tr};\xi)K_Q(\xi)_{|Q=1}d\xi \tag{C-6}$$

where $\Delta_{p\ no\ crack}$ is the LPD from the applied load with no crack, and the second term is the LPD caused by the crack. E_0 is the Young's modulus of the initial material; K_Q is the SIF from a fictitious dipole force Q applied at the load point, and can be written in the form

$$K_Q(\xi)_{|Q=1} = \frac{1}{B}\int_0^{\xi} G^{SIF}(x,\xi)dx \tag{C-7}$$

Similarly, the relative ($\Delta_{no\ crack}$=0) crack opening displacement (COD) at the point x_1 caused by a unit dipole force at x_0 is expressed by

$$G^{COD}(x_0,x_1;l+l_a) = \frac{2}{E_0}\int_{max\{x_0,x_1\}}^{l+l_a} G^{SIF}(x_0,\xi)G^{SIF}(x_1,\xi)d\xi \tag{C-8}$$

Then the COD from σ_{tr} applied at the interval $[l,l+l_a]$ is obtained by means of superposition (integration) as

$$\delta(\sigma_{tr};x_1;l+l_a) = -\sigma_{tr}\int_{l}^{l+l_a} G^{COD}(x_0,x_1,l+l_a)dx_0 \qquad \text{(C-9)}$$

Substituting the term on the right side of Eq. (C-8) for G^{COD} in Eq. (C-9), and changing the order of integral gives

$$\delta(\sigma_{tr};x_1,l+l_a) = \frac{-2\sigma_{tr}}{E_0}\int_{x_1}^{l+l_a}\int_{l}^{\xi} G^{SIF}(x_0,\xi)G^{SIF}(x_1,\xi)dx_0d\xi \qquad \text{(C-10)}$$

Since the zone of material transformation only includes the region where $x_1 \geq l$, $x_1 < l$ is not considered in the above integration. Similarly, the COD from the remote applied stress σ_∞ is

$$\delta(\sigma_\infty;x_1,l+l_a) = \frac{2\sigma_\infty}{E_0}\int_{x_1}^{l+l_a}\int_{0}^{\xi} G^{SIF}(x_0,\xi)G^{SIF}(x_1,\xi)dx_0d\xi \qquad \text{(C-11)}$$

Thus the COD for the problem in Fig. 4.1a can be evaluated as

$$\delta(\sigma_\infty,\sigma_{tr};x_1;l+l_a) = \delta(\sigma_\infty;x_1;l+l_a) + \delta(\sigma_{tr};x_1;l+l_a) \qquad \text{(C-12)}$$

The crack driving force is the partial derivative of the Gibbs potential with respect to crack length. The Gibbs potential G of the model (per unit thickness) is [57]

$$G = \Pi + 2\gamma l + \gamma_{tr}V_{tr} + G_0 \qquad \text{(C-13)}$$

The potential energy Π of the elastic body is given by

$$\Pi = F_s - W = -\frac{1}{2}W \qquad \text{(C-14)}$$

where F_s is the strain energy of the system and W is the work done by the external load. For the problem in Fig. 4.1a, the work can be written as:

$$W = \sigma_\infty B\Delta_p - \sigma_{tr}\int_{l}^{l+l_a} \delta(\sigma_\infty,\sigma_{tr};x_1,l+l_a)dx_1 \qquad \text{(C-15)}$$

Using the assumption of a thin process zone, the volume V_{tr} (per unit thickness) can be determined by [10]

$$V_{tr} = \frac{1}{\lambda - 1} \int_{l}^{l+l_a} \delta(\sigma_\infty, \sigma_{tr}; x_1, l+l_a) dx_1 \tag{C-16}$$

Equations (C-14), (C-15) and (C-16) show that the potential energy Π is

$$\Pi = -\frac{1}{2}\sigma_\infty B \Delta_p + \frac{1}{2}\sigma_{tr}(\lambda-1)V_{tr} \tag{C-17}$$

From Eq. (C-17), the crack driving force X^{CR} is

$$X^{CR} = -\frac{\partial G}{\partial l}_{|l+l_a=const.} = -\frac{\partial \Pi}{\partial l}_{|l+l_a=const.} - 2\gamma - \gamma_{tr}\frac{\partial V_{tr}}{\partial l}_{|l+l_a=const.} \tag{C-18}$$

Using Eq. (C-17), the change of the potential energy caused by crack growth for the problem in Fig. 4.2a is

$$\frac{\partial \Pi}{\partial l}_{|l+l_a} = -\frac{1}{2}\sigma_\infty B \frac{\partial \Delta_p}{\partial l}_{|l+l_a=const.} + \frac{1}{2}\sigma_{tr}(\lambda-1)\frac{\partial V_{tr}}{\partial l}_{|l+l_a=const.} \tag{C-19}$$

From Eqs. (C-5), (C-6), (C-7) and (C-10),

$$\frac{\partial \Delta_p}{\partial l}_{|l+l_a=const.} = \frac{2}{E_0}\int_0^{l+l_a} \frac{\partial}{\partial l}\left[K(\sigma_\infty, \sigma_{tr}; \xi)\, K_Q(\xi)_{|Q=1}\right]_{|l+l_a=const.} d\xi$$

$$= \frac{2}{E_0}\int_0^{l+l_a} \left[\sigma_{tr} G^{SIF}(l,\xi)\frac{1}{B}\int_0^{l+l_a} G^{SIF}(x,\xi)dx\right] d\xi$$

$$= \frac{\sigma_{tr}}{B\sigma_\infty}\delta(\sigma_\infty; l, l+l_a) \tag{C-20}$$

Taking the partial derivative of each side of Eq. (C-16) with respect to crack length gives

$$\left.\frac{\partial V_{tr}}{\partial l}\right|_{l+l_a=const.} = \frac{1}{\lambda-1}\left[-\delta(\sigma_\infty,\sigma_{tr};l,l+l_a) + \int_l^{l+l_a} \left.\frac{\partial \delta(\sigma_\infty,\sigma_{tr};x_1,l+l_a)}{\partial l}\right|_{l+l_a=const.} dx_1\right] \tag{C-21}$$

Equations (C-10), (C-11) and (C-12) show that

$$\int_l^{l+l_a} \left.\frac{\partial \delta(\sigma_\infty,\sigma_{tr};X_1,l+l_a)}{\partial l}\right|_{l+l_a=const.} dx_1 = \int_l^{l+l_a} \frac{2\sigma_{tr}}{E_0}\int_{x_1}^{l+l_a} G^{SIF}(l,\xi)\, G^{SIF}(x_1,\xi)\, d\xi dx_1$$

$$= -\delta(\sigma_{tr};l,l+l_a) \tag{C-22}$$

Substituting $-\delta(\sigma_{tr};l,l+l_a)$ for integral in Eq. (C-11) gives

$$\left.\frac{\partial V_{tr}}{\partial l}\right|_{l+l_a=const.} = -\frac{1}{\lambda-1}\left[\delta(\sigma_\infty,\sigma_{tr};l,l+l_a) + \delta(\sigma_{tr};l,l+l_a)\right] \tag{C-23}$$

Substituting the results of Eqs. (C-20), (C-23) into Eq. (C-19(gives

$$\left.\frac{\partial \Pi}{\partial l}\right|_{l+l_a=const.} = -\sigma_{tr}\delta(\sigma_\infty,\sigma_{tr};l,l+l_a) \tag{C-24}$$

Substituting the results of Eqs. (C-24), (C-23) into Eq. (C-28) yields

$$X^{CR} = \sigma_{tr}\delta(\sigma_\infty,\sigma_{tr};l,l+l_a) - 2\gamma + \frac{\gamma_{tr}}{\lambda-1}\left[\delta(\sigma_\infty,\sigma_{tr};l,l+l_a) + \delta(\sigma_{tr};l,l+l_a)\right] \tag{C-25}$$

The last term in Eq. (C-18) results from the change of the Gibbs potential caused by material transformation. It is necessary to emphasize that the change of the process zone volume caused by crack growth consists of two parts. In the right side of Eq. (C-21), the first term

represents a decrease in volume caused by an infinitesimal decrease in the process zone length. The second term represents an increase in the volume because of an infinitesimal increment of the process zone width. Thus the first term corresponds to the release of the energy.

However, the allotropic transformation from the initial to the drawn material is not a reversible process, and process zone material cannot be transformed into initial material by releasing the acting stress. Therefore the change of energy associated with the first part is simply a release of strain energy of the drawn material. In polyethylene the strain energy density of the drawn material is known to be very small in comparison with γ_{tr} (14). Thus the change of the Gibbs potential associated with the material transformation is completely represented by the second term, and the first term is negligible. Taking this into account, the crack driving force can finally be reduced to

$$X^{CR} = \sigma_{tr}\left[\delta(\sigma_{\infty},\sigma_{tr};l,l+l_a) + \frac{\gamma_{tr}}{\sigma_{tr}(\lambda-1)}\delta(\sigma_{tr};l,l+l_a)\right] - 2\gamma \qquad \text{(C-26)}$$